Study of a dipolar gas confined in a one-dimensional lattice and construction of a new imaging setup for the ERBIUM experiment.

– MASTER THESIS –

by

Louis Lafforgue, BSc

submitted to the Faculty of Mathematics, Computer Science, and Physics of the University of Innsbruck

in partial fulfillment of the requirements
for the degree of Master of science (MSc)

advisor:

Univ.-Prof. Dr. Francesca Ferlaino,
Institute for Experimental Physics, University of Innsbruck

Innsbruck, July 2022

Abstract

This thesis describes the work performed during my master thesis in the ERBIUM experiment. The first part explains the steps toward the observation of Bloch oscillations with a dipolar gas of ^{166}Er. We studied Bloch oscillations with ultracold dipolar erbium atoms confined in a one-dimensional lattice. We performed measurement at different scattering lengths, from the contact-dominated regime to the dipolar-dominated one. By combined theoretical and experimental efforts, we emphasize the effect of quantum fluctuations in the dephasing time of Bloch oscillations. In the regime of small mean-field interactions, we observed that the dipole-dipole interactions play an important role in determining the number of occupations of the lattice sites. Special emphasis is given to describe the experimental realization and the method used to analyse the raw data.

The second part of this thesis describes, characterizes, and details the implementation of a sub-micron resolution imaging system. Imaging systems are essential components of ultracold gases experiments, and achieving a high-resolution imaging system enables to probe in-situ spatial density distribution. We performed tests on an objective produced by *Special Optics*. We detail the way to obtain the point-spread function and found an experimental resolution of 0.85(2) µm. We designed a mechanical holder including all degrees of freedom needed to align the objective with the atoms. Finally, we highlight a very flexible optical path using four different optical wavelengths that will enable us to use the objective not merely to image the density distribution but also to apply arbitrary potentials to the atoms.

Contents

Chapter 1

Introduction

1.1. Motivation

The beginning of the 20$^{\text{th}}$ century saw the emergence of quantum mechanics to describe the microscopic world. One core concept of wave-particle duality was proposed by Louis de-Broglie [dB25], stating that a microscopic object, such that electrons or atoms, can behave like a wave or a particle at the same, depending on the experimental environment. Quantum mechanics appears to be the key to describe atoms, subatomic particles and light-matter interaction, and succefully describe, e.g., the photo electric effect or the electron structure of atoms.

Nevertheless, one question remained: how to describe macroscopic objects like a metal, composed of 10^{23} atoms and electrons, all interacting with each others? The intrinsic mathematical construction of quantum mechanics causes classical computer to be very inefficient to simulate those systems, and systems with large number of particles are impossible to solve exactly even with supercomputers. In 1982, Richard Feynman proposed to use an analogue quantum system where it is possible to isolate, control and detect quantum states to simulate a more complex system [Fey82]. The concept of a *quantum simulator* was born. In the past decades, many platforms, capable of performing qunatum simulation, have been developed, from trapped ions to superconducting circuits and photonics systems [Tra12].

In 1995, remarkable progress in the field of experimental quantum physics, quantum optics, and lasers enabled the first realization of a Bose-Einstein condensate (BEC) [Dav95] [And95] [Bra95]. Eric A. Cornell, Carl E. Wieman and Wolfgang Ketterle were rewarded for this breakthrough with the Nobel price in 2001 [Kru01]. A BEC is a macroscopic metastable state of matter formed when a gas of bosons condenses to the lowest state of energy. A pure BEC is zero entropy and then fully governed by quantum physics. The phase coherence guarantees that a BEC can be described by a single *wave function*. The early studies of this new state of matter were focused

on macroscopic quantum phenomena, such as matter-wave interference [And97] or vortices [Mat99].

But rapidly, ultracold gases have revealed themselves to meet all the requirements for quantum simulations [Blo12]. The system is very well isolated from its environment, it is possible to control the interactions, e.g., via a magnetic Feshbach resonance [Chi10], and direct imaging techniques have been developed, pushing the resolution to a single atom [Bak09]. Furthermore, early theoretical [Jak98] and experimental works [Hem93] proposed to create crystals of light to mimic the periodic structure of solids, so-called *optical lattices*. They enabled the first experimental of the Bose-Hubbard model [Hub63] and the first observation of the Mott insulator phase [Gre02].

At the early stage of BEC, most of the experiments were working with alkali atoms and only *contact interaction* was present in the systems. The last decade marked a turning point with the production of the first BEC of lanthnides atoms, dysprosium [Lu11] and erbium [Aik12]. Those magnetic atoms add a new interaction to the ultracold toolbox, the dipole-dipole interaction [Lah09] [Bar08]. The long-range and anisotropy characters allow accessing new quantum phases, e.g., macrodroplets or supersolid [Cho22]. Furthermore, magnetic atoms combined with optical lattices form a paradigmatic platform for the study of strongly correlated systems [Bar12] [Bai16].

Until now, most of the theory of ultracold gases uses the framework of *mean field approximation*. More recently, beyond mean-field contributions have been the key to the understanding of stabilization mechanisms in dipolar gas, e.g with the macrodroplet [Cho16]. Ref. [Lim12] showed that beyond mean-field contributions have to be taken into account with the so-called *Lee-Huang-Yang* (LHY) term. If in the theory, beyond mean field effects are now well understood and their important role undisputed, the exact mathematical expression is still subject to intense debate, and a quantitative experimental measure of its exact form is still missing.

1.2. Thesis outline

This thesis is divided in two parts essential on ultracold experiments, controlling and imaging. The first part deals with the study of a dipolar gas of erbium confined in a one-dimensional lattice. In particular on the use of Bloch oscillations (BOs) as an interferometric tool to asses the role of beyond mean-field contributions. The second part relates the implementation of a new high-resolution imaging system for erbium.

Chapter 2 reviews the relevant properties of erbium used during this thesis.

Chapter 3 is devoted to the physics of ultracold gases loaded in a 1-dimensional lattice. We review in detail the emergence of the band structure and BOs in presence of an externalforce. We present the effect of interactions on BOs and introduce the theoretical model used for this project.

Chapter 4 is the heart of this project and addresses the experimental procedure to observe BOs with a dipolar gas of erbium as well as the method to analysis to row data.

Chapter 5 presents the new imaging setup which will be implemented in the ERBIUM experiment. In the first section, we briefly review the diffraction theory to understand how imaging systems are described. In the second section, we present the optical design and the test realized on the new objective. We provide to the reader details on the numerical analysis of the point spread function. The last section deals with the implementation of the objective in the experiment as well as the planification of the laser distribution.

Chapter 2

Properties of erbium

2.1. Erbium at glance

Erbium(Er) is a rare-earth element belonging to the lanthanide family. In its solid form, it is a soft and silvery metal. It is used in the industry mix with other material to increase the workability of an alloy, for example in reducing the stiffness of the material [Gup05]. Erbium has a high melting point at 1529° and a boiling point at 2900°. Its mostly known form, Er^{3+}, finds applications in doped fiber and glass where it is used, for instance, to amplify laser light [Bec99].

Er has an atomic number of Z=68 and presents five bosonic isotopes and one fermionic isotope. Tab. 2.1 gives the number of nucleons, the abundance of each isotope, and the statistic associated.

Isotopes	Natural Abundance	Statistics
^{162}Er	0.14	Boson
^{164}Er	1.61	Boson
^{166}Er	33.6	Boson
^{167}Er	23.0	Fermion
^{168}Er	26.8	Boson
^{170}Er	15.0	Boson

Table 2.1.: six stable isotopes of erbium, five bosonic and one fermionic. For each isotope, the abundance is reported. Table extracted from [M11a]

All the work of this thesis has been realized with ^{166}Er , presenting advantageous scattering properties and a substantial abundance.

2.2. Electron configuration and energy level structure

The electronic shell of erbium atom is composed of 68 electrons, filling the atomic orbitals following the Madelung rule. Among these electrons, 14 are valence electrons, giving rise to the electronic configuration in the ground state,

$$[\mathrm{Xe}]4f^{12}6s^2, \tag{2.1}$$

where [Xe] refers to the electron configuration of Xenon.

For neutral erbium in the ground state, the $6s$ shell is completely filled before the $4f$. This partially filled inner shell $4f$ gives a structure called *submerged-shell*. The two vacant electrons of the $4f$ shell results in large orbital anisotropy and a large orbital and spin quantum number.

The *submerged-shell* structure also gives rise to a very rich energy spectrum in the optical range. Indeed, the electrons of the $4f$ shell can be excited easily to the unfilled positions within the optical transition range. [Kra18] reports 672 transitions from the ground state with J ranging from 2 to 12. Figure 2.1 reports all the energy levels as well as the transitions used in our experiment; see Chap. 4 or [Fri14a].

The broad 401 nm transition in combination with the one at 583 nm makes erbium suitable to be laser cooled. More details are presented in Chap. 4. Furthermore, it offers transitions with narrow linewidth, particularly advantageous for coherent light manipulation.

2.3. Magnetic moment

Another important property of erbium is the large magnetic moment μ in the ground state. It is a direct consequence of the *submerged-shell* structure, as the electron spin-orbit coupling leads to a large total angular momentum J. The magnetic quantum number m_j can range from $-J$ to $+J$ and is related to the magnetic moment as follow:

$$\mu = m_j \mu_B g_J, \tag{2.2}$$

where μ_B is the Bohr magneton and g_J the landé factor. In the case of only spin-orbit coupling g_J can be written:

$$g_J = 1 + (1 - g_S)\frac{J(J+1) + S(S+1) - L(L+1)}{2J(J+1)}, \tag{2.3}$$

with $g_S \approx 2.002$. L and S are respectively the orbital momentum number and the total spin number. For erbium, jj-cpoupling between electrons has to be taken into

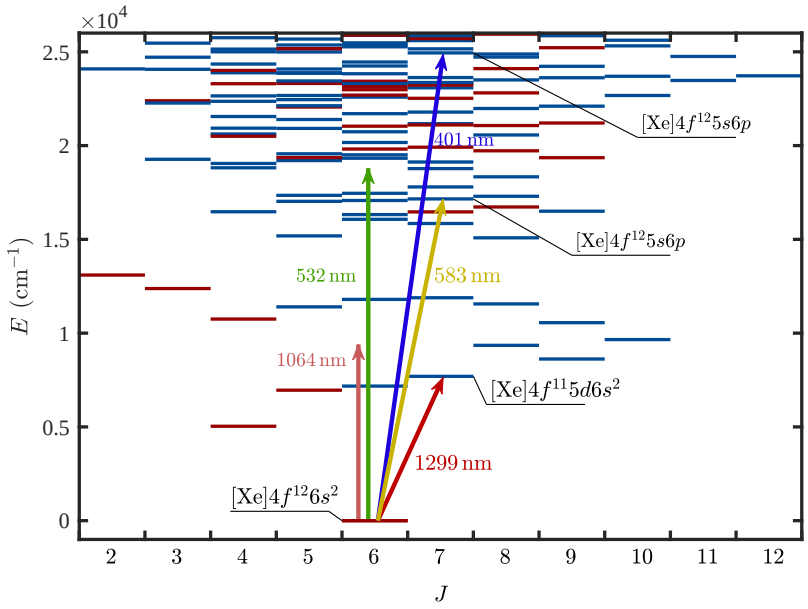

Figure 2.1.: Energy level spectrum of erbium. Energy levels are represented in the relevant range for trapping and cooling. Even and odd parity are shown in blue and red, respectively. 401 nm is used for the Zeeman slower, the transversal cooling and imaging. The narrow line at 583 nm corresponds to the magneto-optical trap transition. The transition at 1299nm features an ultra-narrow linewidth of 2 Hz, making it suitable for coherent spin manipulation. The light at 1064 nm and 532 nm is used to create far detuned optical potentials [Gri00]

consideration and one finds g_J=1.163801(1) [Con63]. One finds that for ^{166}Er in its ground state ($m_j = -6$), the magnetic moment is,

$$\mu = -6.982806(6)\mu_B. \tag{2.4}$$

We can notice that when the spin state is changing, the magnetic moment changes accordingly.

2.4. Interactions between erbium atoms

2.4.1. Contact interaction

Despite the very dilute character of ultracold gases, atoms can interact with each other. In quantum mechanics, the interaction between particles is covered by the *scattering theory*. When two atoms are close to each other, they interact by the so-called Van der Waals (vdW) interaction. This interaction can be described in the first order by

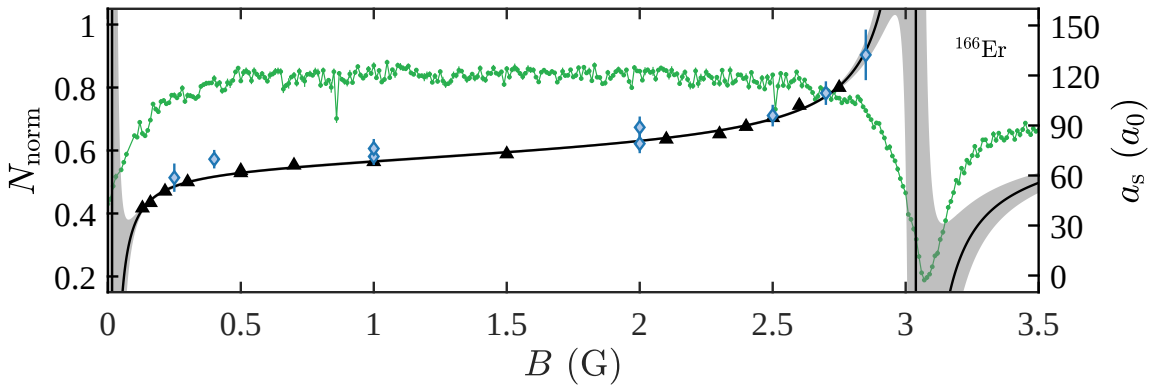

Figure 2.2.: Feshbach resonance around 1.9 G. Green circles: Atom number versusmagnetic field. Blue diamond: scattering length obtained by cross-thermalization. Black triangle: Scattering length obtained by lattice modulation spectroscopy. Black solid line:fir of a_{s}considering 5 resonances. Figure adapted from [Cho16].

a potential with the form,

$$U_{VdW}(r) = \frac{C_6}{r^6}, \tag{2.5}$$

with C_6 is the vdW coefficient and r is the relative distance between the atoms. This potential, responsible for the contact interaction at very low temperature, is short-range and isotropic. For low temperature (i.e. low collision energy) scattered by a short-range scatterer cannot be resolved the exact structure of the potential since the De Broglie wavelength is very long. The scattering of two particles is fully characterized by the *s-wave* scattering length a_{s}. The interaction potential can be rewritten,

$$U(r) = \frac{4\pi\hbar^2 a_{\mathrm{s}}}{m}\delta(r) = g\delta(r), \tag{2.6}$$

with m the mass.

Addtionnaly, when two atoms collide, a twol-atom level can be resonnantly coupled to a dimer level, this phenomenon is called Feshbach resonance [Chi10]. It is observed experimentally by a sudden loss of atoms. More precisely, this happens when the bound energy of a molecular potential coincides with the bound energy of the scattering potential. The difference in energy can be controlled by an external magnetic field, resulting in a modification of the scattering length a_{s}. Typically, this dependence can be discribed in term of simple formula, which for isolated resonances reads,

$$a_{\mathrm{s}}(B) = a_{\mathrm{bg}}(1 - \frac{\Delta}{B - B_0}), \tag{2.7}$$

With a_{bg} the background scattering length, Δ the width of the resonance and B_0 the position of the Feshbach resonance.

Due to the orbital anisotropy making the contact scattering chaotics, lanthanides atoms and in particular ^{166}Er exhibit many Feshbach resonances [Fri14b]. In presence

of many resonances, the depedance of $a_s$in B is more complex,

$$a_s(B) = a_{Bg} \prod_i (1 - \frac{\Delta_i}{B - B_i}), \tag{2.8}$$

with i labelling a resonance.

During this thesis, we use a comparatively broad Feshbach resonance around 1.9 G; see Fig. 2.2. This allows to tune the scattering length from $55\,a_0$ to $100\,a_0$ without suffering from too much atom loss.

2.4.2. Dipole-dipole interaction

The strong magnetic moment of erbium induces a dipole-dipole interaction (DDI) between the atoms. With an external polarizing magnetic field, this interaction can be described by a potential with the folowing mathematical expression,

$$U_{dd} = \frac{\mu_0 \mu^2}{4\pi} \left(\frac{1 - 3\cos^2(\theta)}{r^3} \right), \tag{2.9}$$

with μ_0 the vacuum permeability, μ the magnetic moment, r the relative distance between the two atoms and θ the angle between the magnetic field direction and direction of r. The notations are resumed in Fig. 2.3. The two striking properties of the dipole-dipole potential are the long-range character in 3 dimensions and the anisotropy.

Furthermore, by utilizing an external field, it is possible to go from an attractive potential in the *head-to-tail* configuration ($\theta = 0$) , to a repulsive interaction when the dipoles are aligned *side-by-side* ($\theta = \pi/2$).

As the DDI is anysotropic, the many-body properties of an ensemble of erbium atoms are drastically affected by the shape of the trapping potential. For an elongated trap with the weak axis aligned with **B**, the dipoles are mostly head-to-tail and the system is attractive. On the other hand, for a "pancake" trap, where the strong confinement is align with **B**, the dipoles sit side-by-side and the system is mainly repulsive.

To quantify the absolute strength of dipole-dipole interaction, it is usual to define the dipolar length,

$$a_{dd} = \frac{C_{dd}}{12\pi\hbar^2}, \tag{2.10}$$

with $C_{dd} = \frac{\mu_0 \mu^2}{4\pi}$.

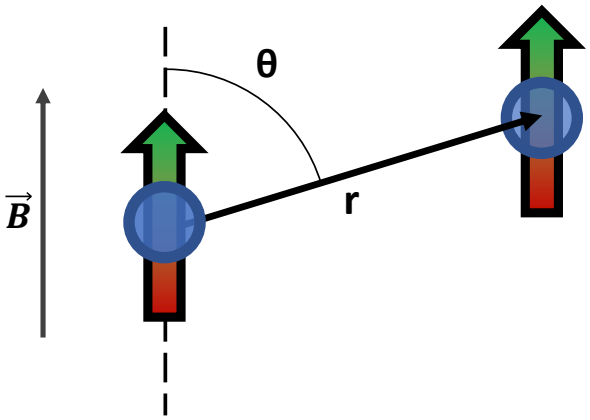

Figure 2.3.: Schematic representation of dipole-dipole interaction. **r** is the distance between the two atoms and θ the angle with the magnetic field direction. The external magnetic field **B** is used to control the orientation of the dipoles.

The dipolar length can be directly compared with the s-wave scattering length and we introduce the ratio

$$\epsilon_{dd} = \frac{a_{dd}}{a_s} \tag{2.11}$$

When $\epsilon_{dd} << 1$, the contact interaction is much stronger and DDI doesn't play a significant role in the properties of the system. On the other hand, for $\epsilon_{dd} > 1$, DDI dominates and exotic behaviours appear. Tuning the s-wave scattering length through Feshbach resonance makes it possible to study the crossover at $\epsilon_{dd} \approx 1$. For ^{166}Er the dipolar length is fixed at $a_{dd} = 66.5\, a_0$ and with the Feshbach resonance in Fig. 2.2, ϵ_{dd} can be varied from approximately 1.2 to 0.7.

Chapter 3

Theory: quantum gas in a one-dimensional lattice

Already before the creation of the first Bose-Einstein condensate, physicists proposed to engineer periodic potentials and study the emerging properties with a system of ultracold atoms [Hem93]. Loading a BEC in a periodic potential represents a very robust system to tackle solid-state and condensed matter physics problems [Blo05]. Indeed, those systems feature a very high degree of controllability, in particular, the potential landscape and the interactions between particles.

For instance, ultracold gases permitted the observations of Bloch oscillations (BO). BO were originally predicted by Felix Bloch in the framework of solid-state physics [Blo29], they describe the movement of a non-interacting electron confined in a periodic potential and subject to an external force. Because of the very high oscillation frequencies and the difficulty to image the electron motion, physicists had to wait for the arrival of BEC to observe the first signs of BO [Niu96] [Wil96].

In this Chapter, we review the theoretical tools necessary to understand how BO arise with a BEC and the equations used to describe BO with a gas of ^{166}Er .

3.1. One-dimensional optical lattices

In presence of an optical field (typically laser beams) described by $\overrightarrow{E}(\omega, \mathbf{r})$, with ω the frequency, the atoms experience two forces, the radiation pressure, dissipative and used to cool, and the dipole potential. While the radiation pressure is related to light scattering and is therefore a dissipative process, used for laser cooling, the dipole potential is created by the energy shift of the atomic state in the light field, the so-called AC Stark shift [Gri00].

When induced by far-detuned light, the latter creates an external potential for the atoms. For alkali atoms, the potential created scales as follows,

$$V(\mathbf{r}) \propto Re(\alpha(\omega))|\overrightarrow{E}|^2 \tag{3.12}$$

where $\alpha(\omega)$ is a complex number called the *polarizability* and $|\overrightarrow{E}|^2$ the intensity of the field at a position $\mathbf{r}$. However, due to the orbital anisotropy erbium has a tensorial polarizability $\bar{\alpha}$. The dipolar force depends on the polarization of the light and advance theoritical methods are needed to predict $\bar{\alpha}$ [Li17] [Bec18]. For more details about dipolar potential in general, the reader can refer to [Gri00].

To engineer a stationary periodic potential, so-called optical lattice, we can counter-propagate two laser beams with the same frequency and create a standing wave. The strength of the potential, or potential depth, can be controlled by the power of the lasers. In the ERBIUM experiment, the laser beams are propagating along the gravity axis z, which results in a periodic potential along z, see Fig. 3.1.

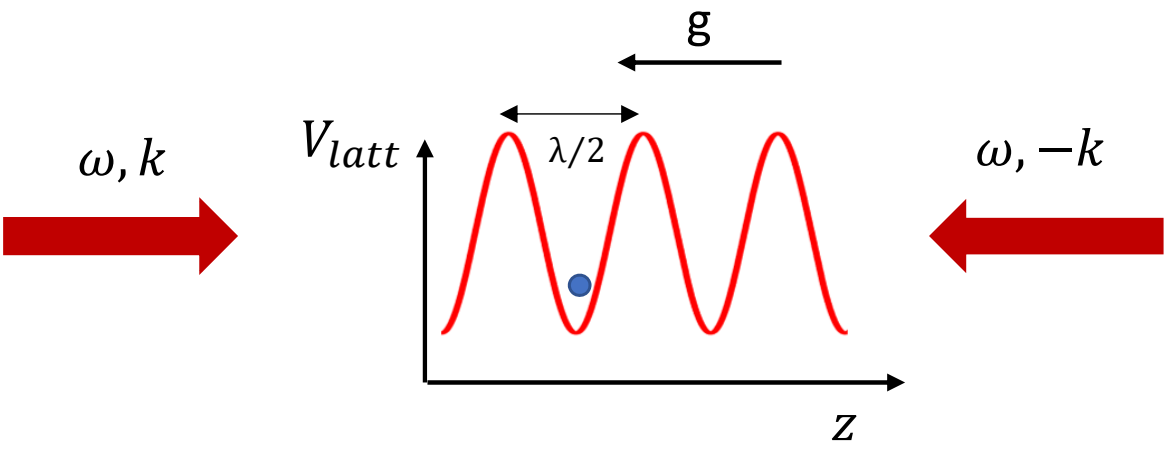

Figure 3.1.: 1D optical potential created by 2 counter-propagating beams with the same frequency. The atoms will experience a periodic potential V_{latt} with period $\lambda/2$. ω is the frequency and k the wave vector

The potential created has the mathematical expression,

$$V_{\text{latt}}(z) = sE_{\text{rec}} \sin^2(\frac{2\pi z}{\lambda}). \tag{3.13}$$

Here, we express the potential depth as a multiple s of the recoil energy $E_{\text{rec}} = \hbar^2k^2/(2m)$, with $k = 2\pi/\lambda$, the recoil momentum, or the momentum gain after absorbing one photon and m the mass of the particle. λ is the wavelength of the lattice. The minima of potential are often called *lattice sites*, they are separated by a distance $d = \lambda/2$.

In the experiments, this creates an array of two-dimensional BECs. Additionaly, the laser beams used to create the standing waves have a transverse gaussian profile,

creating harmonic confinement along the transverse directions x and y. It is very weak in comparison with standard dipole traps (only a few hertz) but has to be taken into consideration during the numerical simulations.

3.2. Non-interacting quantum gas in a one-dimensional lattice

3.2.1. Single particle in an optical lattice

In order to understand the physics of a BEC loaded into an optical lattice, we first have look at the effect of a periodic potential on the wavefunction of a single particle. In the most simple case, we ignore the two transversal directions, which is supposed to give only a small correction. For non-interacting systems, the ground-state and the energy associated can be calculated by solving the 1D stationnary Schrödinger equation,

$$\left[\frac{-\hbar^2}{2m}\frac{d^2}{dz^2} + V_{\text{latt}}(z)\right]\psi_n(z) = E_n\psi_n(z). \tag{3.14}$$

E_n and $\psi_n(z)$ correspond respectively to the eigenenergies and eigenfunctions that have to be determined.

To find the ground state, we apply the Bloch band theory [Blo29], developed in the field of solid-state physics and described in detail in [Asc76] and [Kit05]. In presence of a periodic potential, the Bloch theorem states that we can find solutions of Eq. (3.14) with the form,

$$\psi_{n,q}(z) = e^{iqz}u_n(z,q). \tag{3.15}$$

Here, q is a continuous variable called quasimomentum and $u_n(z,q)$ an unknown periodic function with the same periodicity as the external potential. Thanks to the periodicity, we can without loss of generality restrict $q \in [-k,k]$, called the Brillouin zone(BZ).

As $u_n(z,q)$ is a periodic function, we can further decompose it in a sum of plane waves,

$$u_n(z,q) = \sum_j c_{n,j}e^{-iqjz}, \tag{3.16}$$

with the complex coefficients $c_{n,j}$. This corresponds to the Fourier transform.

By inserting Eq. (3.15) and Eq. (3.16) in Eq. (3.14), we can derive the following discrete

equation,

$$\left[(2j+\frac{q}{k})^2+\frac{s}{2}\right]c_{n,j}-\frac{s}{4}(c_{n,j-1}+c_{n,j+1})=\frac{E_n}{E_{\mathrm{rec}}}. \tag{3.17}$$

This is a basic eigenvalue problem which can be solved numerically for an arbitrary q.

For any value of q, we retrieve the different energy levels $E_n(q)$ and the coefficient c_j of the Bloch function associated $\Psi_{n,q}$. For a given n, $E_n(q)$ is a continuous function and is often refered as a *band*. Figure 3.2 shows $E_n(q)$ for $n=1-3$ ans s=1,3 and 8.

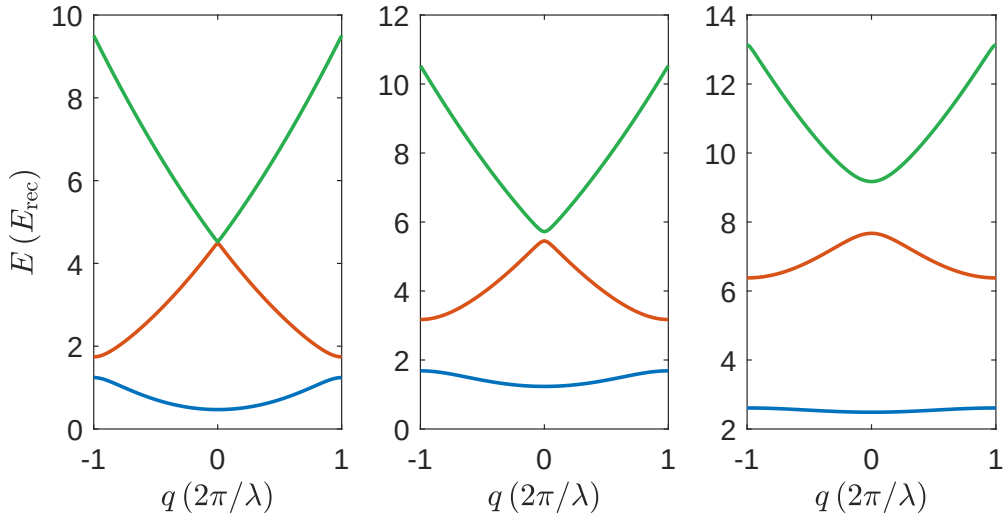

Figure 3.2.: Energy bands from 3 different values of s, from left to right, $s=1$, $s=3$ and $s=8$. The first 3 bands are represented with different colours, in blue $E_0(q)$, in yellow $E_1(q)$ and in red $E_2(q)$. the gap between the different bands increases with the potential depth.

The dispersion relation $E_n(q)$ is an essential characteristic of particles confined in a periodic potential. For instance, in solid-state physics, this band structure explains the conduction of electrons in a metal.

The Bloch functions form a complete orthogonal set for Eq. (3.14) and are completely delocalized over the lattice sites. For a deep lattice, it is more convenient to introduce the Wannier-functions as a basis [Wan37]. They have the property to be localised at a single lattice site and are mathematically defined as the inverse Fourier transform of the Bloch functions,

$$w_n(z-z_j)\propto\int_{-\hbar k}^{\hbar k}dqe^{-iqz_j}\psi_{n,q}(z), \tag{3.18}$$

where z_j corresponds to the position of the j^{th} lattice site.

The concept of localize particle in a lattice site leads to the interpretation of a delocalized state as a state with particles tunnelling between neighbouring lattice sites at a rate J,

$$J = -\int_{-\infty}^{\infty} w_n(z - z_j)\hat{H}w_n(z - z_{j+1})dz. \tag{3.19}$$

When the lattice is deep enough($V_{\text{latt}} > 5E_{\text{rec}}$), we can considere the lattice as an array of of harmonic potential and use the so-called tight biding approximation. We then find (ref. [Mor06]),

$$J = \frac{4}{\sqrt{\pi}} E_{\text{rec}} s^{3/4} \exp(-2\sqrt{s})/h. \tag{3.20}$$

3.2.2. Bloch oscillations

When confined in a periodic potential, a particle subject to an external Force will start to oscillate, this phenomenon is known as Bloch oscillations. The period of the oscillations can be calculated by a simple semi-classical approach that we will detail. In presence of an external force F, the time dependence of the quasimomentum can be written,

$$q(t) = q_0 + Ft/\hbar, \tag{3.21}$$

with q_0 the initial quasimomentum. Due to the k periodicity of the BZ, after a time,

$$T_{BO} = 2k\hbar/F, \tag{3.22}$$

the states are again equivalent and the wave functions are the same, besides a global phase factor.

A more rigorous approach to the BO is the so-called Wannier-stark ladders. We will now discuss briefly this approach which will be useful in presence of interactions. As seen in the previous section, it is possible to express the wave function as a superposition of Wannier states.

$$\psi(z,t) = \sqrt{N}\sum_j c_j(t)\, w(z - z_j)\,, \tag{3.23}$$

with $c_j(t)$ complex coefficients and $w(z - z_j)$ a function localized around each lattice site labelled by $z_j = jd$, with $d = \lambda/2$, the distance between each lattice site. When the tunnelling rate J between neighbouring lattice site is small enough in comparison with the external force, the on-site occupation number $\|c_j\|^2$ can be approximated constant and we can write $c_j(t) = c_j(0)e^{-i\phi_j(t)}$, where $\phi_j(t)$ corresponds to a phase.

All the physics is encapsulated in the phase difference between the Wannier functions. In presence of gravity, the phase evolution is governed by the Schrödinger equation with an additional term accounting for the gravity. The Hamiltonian associated is,

$$\hat{H} = \frac{\hat{p}^2}{2m} + V_{\text{latt}}(z) + mgz, \tag{3.24}$$

With g the gravity acceleration and m the mass of the particle. Solving the Schrödinger equation gives us,

$$\phi_j(t) = (q - mgt)jd/\hbar. \tag{3.25}$$

We see that gravity has the effect to translate with time the wave function in the quasimomentum space, and due to the periodicity of the quasimomentum, the wave function will undergo oscillations in momentum space. When the wave function reaches one edge of the BZ, it reappears at the other edge by a sudden jump. This sawtooth behaviour, in momentum space, is characteristic of BO.

The first observation of BO with ultracold gases has been done in 1996, in the group of Christoph Salomon [BD96] and Mark Raizen [Niu96] [Wil96]. Nevertheless, they observed damping of the oscillations, which is not included in Eq. (3.25) and prevented the of BO for precesion measurement. As we will see below, this behaviour is due to the actual interactions between particles in a real BEC.

In presence of an external force F_{ext}, a particle initially in the lowest band has a probability to jump to a higher band. The jump probability between E_0 and E_1 is given by [Mor06],

$$P_t = e^{-F_t/F_{ext}}, F_t = \frac{s^2 E_{\text{rec}}}{d}\frac{\pi^2}{32}, \tag{3.26}$$

with $d = \lambda/2$, the distance between 2 lattice sites. If this probability is too high, the atoms will get excited and lost. For typical ultracold experiments with $s > 1$ and atoms subject to gravity, $P_t << 1$ and the excitation to a higher band can be omitted for the rest of the thesis.

3.3. Bloch oscillations with a Bose-Einstein condensate

3.3.1. Gross-Pitaevskii equation

A BEC is a gas of bosons in the same quantum states. Therefore, it is possible to describe them by a single complex wave function $\Psi(\mathbf{r}, t)$, product of the individual wave functions $\psi_i(\mathbf{r}, t)$,

$$\Psi(\mathbf{r}, t) = \prod_i \psi_i(\mathbf{r}, t). \tag{3.27}$$

Here, $\mathbf{r}$ is the 3D position vector, $\mathbf{r} = (r_1, r_2, r_3) = (x, y, z)$. This wave function obeys the so-called Gross-Pitaevskii equation(GPE) Eq. (3.28), derived independently by Gross and Pitaevskii in 1961. The GPE makes use of the Hartree-Fock and pseudo-potential approximation to describe the ground state of a system of identical bosons. In the case of only contact interacting particles, the time-dependant GPE reads,

$$i\hbar\frac{\partial}{\partial t}\Psi(\mathbf{r},t) = \Big[\frac{\hbar^2}{2m}\nabla^2 + V_{\text{ext}}(\mathbf{r}) + g|\Psi(\mathbf{r},t)|^2\Big]\Psi(\mathbf{r},t). \tag{3.28}$$

The first term of the right part accounts for the kinetic energy, $V_{\text{ext}}(\mathbf{r})$ corresponds to the external potential and $g = \frac{4\pi\hbar^2 a_s}{m}$ the contact interaction, with the m mass of ^{166}Er and a_s the s-wave scattering length. Eq. (3.28) represents the Schrödinger equation counterpart for many-body bosons and all the results presented in Sec. 3.2.1 can be derived for an assembly of bosons. We consider them unchanged if the interaction term $g = 0$. However, as we will see, neglecting the interaction is in most cases a too strong approximation to describe Bloch oscillations with a BEC.

3.3.2. Interaction-induced dephasing

As we saw in Sec. 3.2.2, in absence of interactions between particles, the phase evolution will only be governed by the external potential, i.e gravity, and Bloch oscillations will go on forever. But, when the atoms interact with each other, a dephasing between the lattice sites occurs, resulting in a broadening of the momentum cloud and a limited observation time of the BO. This phenomenon can be formally understood with the Wannier-stark Ladder presented before. When the atoms interact, an additional term needs to be added to the phase Eq. (3.25) and we now have,

$$\phi_j = (q - Ft)jd/\hbar + g\mu_j t, \tag{3.29}$$

with $\mu_j = \int g|\Psi|^4$, the chemical potential at lattice site j. As the phase depends now on the local chemical potential, the different Wannier components dephase from each other. This is clear when considering the phase velocity,

$$\frac{d\phi_j}{dt} = Fjd/\hbar + g\mu_j. \tag{3.30}$$

While without interactions the phase velocity between neighbouring lattice sites is a constant, with interactions it depends on the local chemical potential. From 3.30, we can expect the minimum of dephasing arises when the variance of the phase velocity is the minimum, which corresponds to minimising g.

Groups of Florence managed to overtake this dephasing limitation with non-interacting fermions [Roa04] in 2004 and with bosonic ^{88}Sr [Fer06] in 2006. They used BO as an interferometric tool to measure gravity acceleration. ^{88}Sr presents an s-wave scattering length substantially close to 0, allowing the observation of up to 5000 oscillations.

Following the proposal in Ref. [Car05], they could deduce the value of g with a precision of 6×10^{-6}.

However, this sensitivity to interactions allows to use BO as an interferometric tool. Aditionnaly with BEC, Feshbach resonance gives the ability to control the contact interaction, which, together with BO, to probe interactions effects. By tunning the scattering length with cesium atoms, in Ref. [Gus08] they could study the transition from non-interacting to interacting BEC. They observed up to 20000 oscillations and associate this minimum of dephasing with the zero-crossing of the Feshbach resonance. Furthermore, they observed a revival of the BO after a certain time, indicating that the broadening and the apparent loss of oscillations is a purely dephasing effect.

3.3.3. Dipole-dipole interaction

It is possible to imagine that the attractive character of DDI can be used to compensate for the dephasing induced by the repulsive contact interactions. But, due to the long-range property, the DDI contributes to both on-site and intersite. Although the on-site attractive DDI can fully compensate for the on-site contact interaction and shift the minimum of dephasing to a higher scattering length, the intersite DDI becomes the limiting factor to the BO. The DDI effect has been first highlighted in Ref. [Fat08], with a weakly dipolar gas of ^{39}K ($\mu_B = 0.96$). This experiment points for the first time to the effect of intersite DDI in optical lattices and addresses the problem of stability of a dipolar gas in a lattice, further studied in [M̈1b].

From a naive point of view, we can imagine that when the attractive DDI is stronger than the total contributions, from the trap and the contact interaction, the BEC will shrink in size and after a certain time collapse. However, it has been shown recently that strongly dipolar gas can remain stable and form self-bound ensembles of ultracold atoms, so-called macro droplets [Sch16] [Cho16]. BO in this regime has not yet been studied and calls upon numerical methods.

3.4. Numerical model

To compare our experimental data, we developed a quasi 1-dimensional numerical scheme. The following paragraph details the equations used to describe our BEC and how we include dynamical effects created by gravity.

3.4.1. Extended Gross-Pitaevskii equation

Even though the GPE equation has been proven to be a very powerful tool to accurately describe the contact interacting BEC, when considering dipolar ^{166}Er , one has to add some terms taking into account the dipolar nature of ^{166}Er . The full extended Gross-Pitaevskii equation (eGPE) used in this work reads,

$$\begin{aligned} i\hbar\frac{\partial}{\partial t}\Psi(\mathbf{r},t) = \Big[& -\frac{\hbar^2}{2m}\nabla^2 + V_{\text{harm}}(\mathbf{r}) \\ & + V_{\text{latt}}(z) - F_{\text{ext}}z + g|\Psi(\mathbf{r},t)|^2 \\ & + \int \mathrm{d}^3\mathbf{r}'\, U_{\text{dd}}(\mathbf{r}-\mathbf{r}')|\Psi(\mathbf{r}',t)|^2 \\ & + \gamma_{\text{QF}}|\Psi(\mathbf{r},t)|^3\Big]\Psi(\mathbf{r},t)\,. \end{aligned} \tag{3.31}$$

$V_{\text{ext}}(\mathbf{r})$ has been separated into 3 different contributions, the 3-dimensional harmonic external potential, $V_{\text{harm}}(\mathbf{r}) = \sum_{i=1,2,3}\frac{1}{2}r_i\omega_i$, the potential created by the lattice, $V_{\text{latt}}(z)$ (Eq. (3.13)), and the potential created by the gravity $F_{ext} = mg$. The third line accounts for the long-range DDI, with $U_{\text{dd}}(\mathbf{r}) = 3\hbar^2 a_{\text{dd}}/m\,(1-3\cos^2\theta)\,/|\mathbf{r}|^3$, where θ is the angle between the polarization axis (y-axis) and $\mathbf{r}$. The last line is the second-order correction to the mean-field approximation, the so-called Lee-Huang-Yang term. In the local density approximation, $\gamma_{\text{QF}} = \frac{32}{3}g\sqrt{\frac{a_{\text{s}}^3}{\pi}}\left(1+\frac{3}{2}\varepsilon_{\text{dd}}^2\right)$ [Lim11].

3.4.2. Our 1-D model

Due to the non-linear behaviour of the eGPE (Eq. 3.31) one has to use numerical methods. Even with a very powerful computer, solving Eq. (3.31) in its more general form is hardly achievable. In this context, we developed a quasi-1-dimensional approach based on Ref. [Bla20], allowing us to probe the dynamic and scan a large range of parameters at a reduced cost.

We start by reducing the wave function to one dimension (1D) by applying the ansatz,

$$\Psi(\mathbf{r},t) = \Phi(x,y,l,\eta)\psi(z,t) \equiv \frac{1}{\sqrt{\pi}l}e^{-(\eta x^2+y^2/\eta)/2l^2}\psi(z,t)\,, \tag{3.32}$$

where l and η are variational parameters corresponding respectively to the width and the anisotropy of the radial wave function. We now insert the above ansatz into the (3.31) and obtain a quasi 1-dimension eGPE.

To solve numerically this equation, we need to discretize it over the lattice sites. For that, we decompose the longitudinal wave function in Wannier functions over every lattice sites.

$$\psi(z,t) = \sqrt{N}\sum_j c_j(t)\, w(z-z_j)\,, \tag{3.33}$$

with the complex amplitudes c_j, and the positions of lattice minima $z_j = (\lambda/2)j$. When the lattice is deep enough, it is possible to approximate the Wannier function by Gaussian of the form $w(z) = (\pi l_{\rm latt}^2)^{-1/4}\, e^{-z^2/2l_{\rm latt}^2}$, where we defined $l_{\rm latt} = (k\sqrt[4]{s})^{-1}$. Those manipulations lead us to the discrete equation

$$\begin{aligned} i\hbar\frac{\partial c_j}{\partial t} =& -J(c_{j+1}+c_{j-1}) \\ &+\Big\{ -F_{\rm ext} z_j + V_{\rm harm}(z) + g^{\rm 1D} N|c_j|^2 \\ &+ N\sum_k U^{\rm dd}_{|j-k|}|c_k|^2 + \gamma^{\rm 1D}_{\rm QF} N^{3/2}\gamma_{\rm QF}|c_j|^3\Big\} c_j\,, \end{aligned} \tag{3.34}$$

Here, J is the tunnelling rate between two neighbouring lattice sites and the reduced parameters, $\gamma^{\rm 1D}_{\rm QF} = 2^{3/2}/(5\pi^{3/2}l^2 l_{\rm latt})^{3/2}\gamma_{\rm QF}$ and $g^{\rm 1D} = g/((2\pi)^{3/2}l^2 l_{\rm latt})$. The DDI in 1D can be rewritten,

$$\begin{aligned} U^{\rm dd}_{|j-k|}(l,\eta) = \int {\rm d}^3\vec{x}\Big\{ &|\Psi_0(\vec{x}-z_{|j-k|}\hat{e}_z, l, \eta)|^2 \\ &\int {\rm d}^3\vec{x}'\, U_{\rm dd}(\vec{x}-\vec{x}')|\Psi_0(\vec{x}', l, \eta)|^2\Big\}\,, \end{aligned} \tag{3.35}$$

with $\Psi_0(\vec{x}', l, \eta) = \Phi(x, y, l, \eta)w(z)$

The computation of the wave function $\Psi(\mathbf{r}, t)$ is done as followed . First, Eq. (3.34) is evolved in imaginary time without the gravity potential to find the ground state together with the minimization of the energy functional. After each step of the imaginary time evolution, l and η are found by a variational approach and the new parameters are used to run the next iteration of imaginary-time evolution. Secondly, the ground state wave-function $\psi(z,t)$ computed is evolved in real-time with Eq. (3.34). Typical results from the simulations are presented in Fig. 3.3.

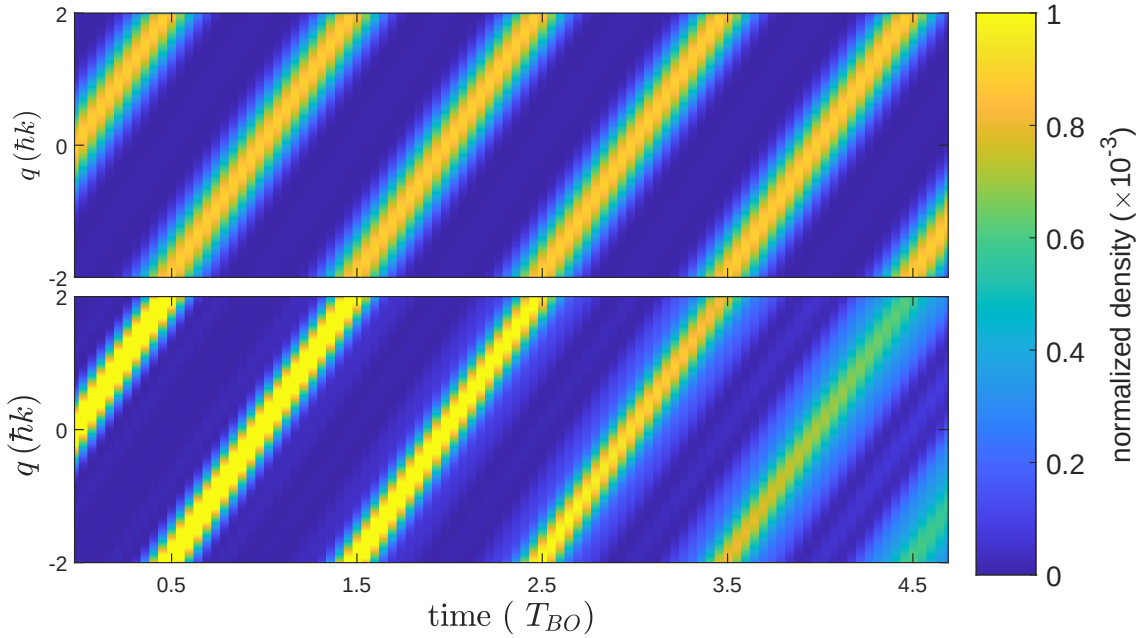

Figure 3.3.: Real time evolution of $\|\psi(q,t)\|^2$ for two different scattering lengths. The upper (resp. lower) plot corresponds to $60\,a_0$ (resp. $83\,a_0$) with a total atom number of 20000. In both cases observe a saw tooth behaviour. At $83\,a_0$, $\|\psi(q,t)\|^2$ is broadened due to interactions. The parameters of those simulations are $\omega_{x,y,z} = 2\pi \times (240(3), 30(3), 217(1))$ Hz, $s = 8$ and with the dipoles align along the weak axis of the trap.

Chapter 4

Observation of Bloch oscillations and ground state properties in a lattice

Given the essential theory to understand the phenomenon of BO in dipolar gases, we detail, in this Chapter, the experimental aspects to observe BO with a dipolar gas of ^{166}Er .

4.1. Producing a Bose-Einstein condensate of erbium

The ERBIUM experiment is a fully operating set up to study ultracold gases of srbium. Designed and built from 2010 to 2012, it aims at producing BEC of bosonic ^{168}Er isotopes [Fri12] and degenerate Fermi gas [Aik14].

The main elements are, the high temperature oven, the Zeeman slower (ZS), high vacuum chamber, narrow line magneto-optical trap (MOT), the optical dipole trap (ODT) and the absorption imaging. We will now resume the process to reach a dipolar BEC of erbium. For an extensive description, the reader can refer to [Fri14a].

The high temperature oven is composed of 2 cells, operating at respectively 1100 °C and 1200 °C. Those temperatures are high enough to create an atomic flux with a velocity of $450\,\mathrm{m\,s^{-1}}$. The first steps to slow down the atoms are the transversale cooling and the ZS, both operating on the broad transition at 401 nm. After the ZS, the atoms have a velocity of $5\,\mathrm{m\,s^{-1}}$ and are slow enough to be captured in the MOT. The MOT uses the narrow transition at 583 nm, corresponding to a doppler temperature of 4.6 µK. The MOT stage prepares aroud 2×10^7 atoms, in their lowest zeeman spin states, at a temperature of 10 µK. To further reach the quantum degeneracy and BEC regime, a last step is necessary. Subsequently to MOT cooling, the atoms are

loaded in the ODT. By lowering the trapping potential progressively, it is possible to perform evaporation cooling and reach BEC regime [Ket96]. An optimized sequence takes approximately 17 s and produce 10^5 atoms of ^{166}Er with $\approx 60\%$ of BEC fraction. During the evaporation, the contact interaction is set to a_s=90 a_0 by an external magnetic field **B**. The orientation of **B** polarizes the dipoles along z. After obtaining the BEC we change the magnetic field along y and go to the final scattering length value in 50 ms.

To image the atomic cloud, we perform absorption imaging. Absorption imaging is a standard technique that consists in shining resonant light and recording the "shadow" created by the atoms on a charge-coupled device (CCD) [Smi11]. In the Erbium experiment, we use 401 nm resonant light. By comparing two pictures, one with atoms and one without, we can deduce the intensity absorbed and map it to an atomic density. The total atom number is obtained by summing the atomic density over all the pixels of the CCD. If we want to extract the number of atoms condensed, we utilize a double gauss fit to separate the thermal part of the condensed part.

Due to the high density, BEC can only be imaged after ballistic expansion, refers as time-of-flight (TOF). This also allows to directly access the BEC in the momentum space. In the Erbium experiment, we use a TOF of 30 ms. In addition, after 15 ms we change the direction of **B** toward the camera axis, this modifies the polarizability and increases the scattering of incoming photons.

4.2. Preparation of the Bose-Einstein condensate in a 1D-lattice

We adiabatically load the BEC in the vertical lattice by exponentially ramping up for 20 ms the lattice beams. The lattice is created by a retro-reflected 1064 nm laser beam with a waist of 30 µm, resulting in a spacing of 532 nm between the lattice sites.For ^{166}Er in the ground state and a lineary polarized 1064 nm light we have a polarizability $Re(\alpha) = 176$ a.u. (atomic units) [Bec18], corresponding to a potential depth of $V_{\text{latt}} = 527\,\text{kHz}\,\text{W}^{-1}$. The beam is provided by an high power and narrow line-width MOPA laser, also used for the horizontal dipole trap. With the available power, we can reach a lattice depth of 80 E_{rec}. With ^{166}Er , we estimated $E_{\text{rec}} = h \times 10.5\,\text{kHz}$. For our experiment, we fixed the lattice depth to 8 E_{rec}. This corresponds to a tunnelling rate (Eq. 3.20) of $J = h \times 33\,\text{Hz}$. In the remaining part, the tunnelling can be omitted because of the small value compared to the gravity. The resulting system is presented in Fig. 4.1(a).

When all the laser beams are switched off, the clouds confined in each *lattice site* will start to expand and interfere. This gives rise to matter-wave interference pat-

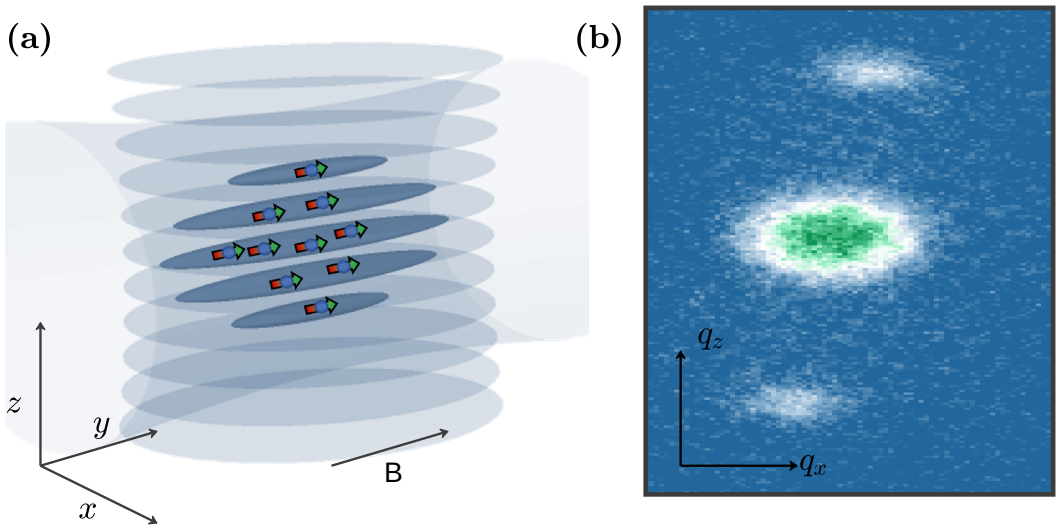

Figure 4.1.: **(a)** Schematic representation of the final system. A 1D optical lattice is loaded with an Erbium BEC, confined in a dipole trap with frequency from an optical dipole trap with trapping frequencies $\omega_{x,y,z} = 2\pi \times (240(3), 30(3), 217(1))$ Hz. Gravity acts along z. The dipoles are polarized along y by an external magnetic field. **(b)** absorption imaging after 30 ms TOF for a_s=58.8 a_0. The two interference peaks sits at a distance $\hbar k$ from the central peak.

terns, represented in Fig. 4.1(b). In absence of interactions during the expansion, the momentum distribution directly represents the Fourier transform of the initial wave function in the lattice. The first-order diffraction appears at a distance of $\hbar k$ from the central peak. The occupation of the diffracted peak gives information on lattice depth and the extension of the ground state. It can be used to calibrate the lattice depth, with for instance the Kapitza-Dirac method [Gad09].

4.3. Observation of Bloch oscillations

To initialize the Bloch oscillations, we switch-off abruptly the dipole trap and let the system evolve for a defined time t_h. The entire sequence is resumed in Fig. 4.2. the lattice beam creates a residual lateral confinement along x and y of 4 Hz. However, our system presents an angle of 9(1) degrees between the gravity axis and the lattice, which is too important for the atom to be laterally confined.

We then hold for a variable time t_h and perform TOF imaging. We take 4 to 6 pictures for many t_h, separated by 0.1 ms time step. Figure. 4.3 shows typical pictures obtained for a_s=83 a_0 and 58.8 a_0 . We observed the sawtooth behaviour, a feature of BO. When the contact interaction is small (58.8 a_0), no dephasing occurs and the

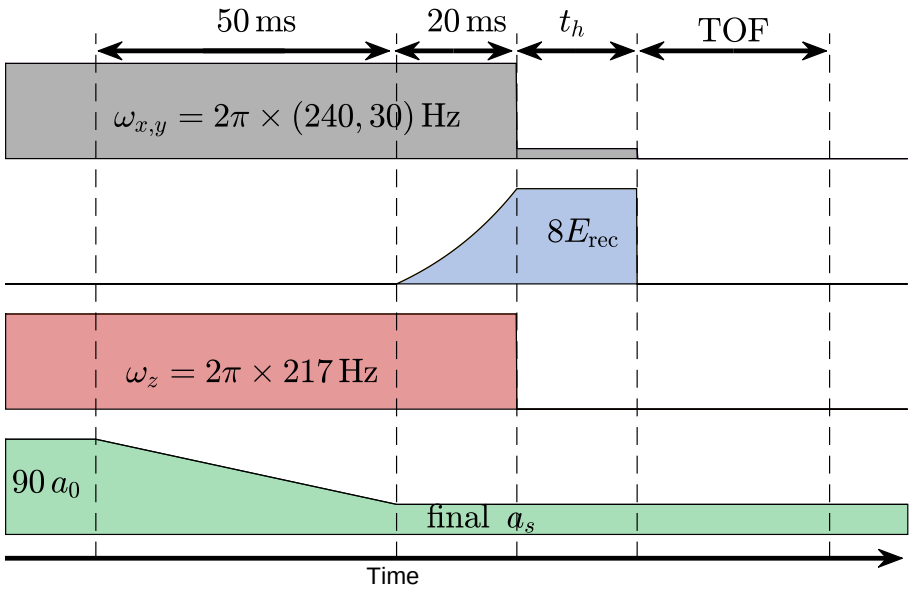

Figure 4.2.: Graphic representation of the parameters of the experiment as a function of time. In grey, the lateral harmonic confinement. The lattice induces a latteral confinement of 4 Hz, remaining during the BO. In blue, the optical lattice depth. In red, the vertical confinement and in green the scattering length. t_h is a variable time and TOF corresponds to 30 ms.

width of the momentum distribution remains the same. On contrary, with strong contact interactions ($83\,a_0$), the oscillation dephases, indicated by the broadening of the momentum distribution.

To analyse the BO more quantitatively, we start by integrating the density profile along x to obtain a 1D momentum distribution that we named for the following $n(q_z)$. First, we looked at the position of the maximum of $n(q_z)$, q_{max} as a function of the holding time t_h, represented in Fig. 4.4 for a_s=58.8 a_0 and 83 a_0. Due to the angle between the gravity and the lattice, the atoms slide on the side and eventually fall out of the lattice potential and this limits our observation time to 12 ms. The pictures are recentered by fitting a 2^{nd} order polynomial function to q_{max} and removing the offset.

To ensure that our observations are indeed BO, we fit the maximum positions $q_{max}(t_h)$ at a_s=58.8 a_0 with the sawtooth function as done in Ref. [Roa04],

$$f(t) = -1 + 2mod(\frac{t-O}{T} + C, 1), \tag{4.36}$$

where O, T and C are the fitting parameters. T directly corresponds to the period of the oscillation and yields $T = T_{BO} = 0.469(4)$ ms, in agreement with Eq. 3.22 yielding

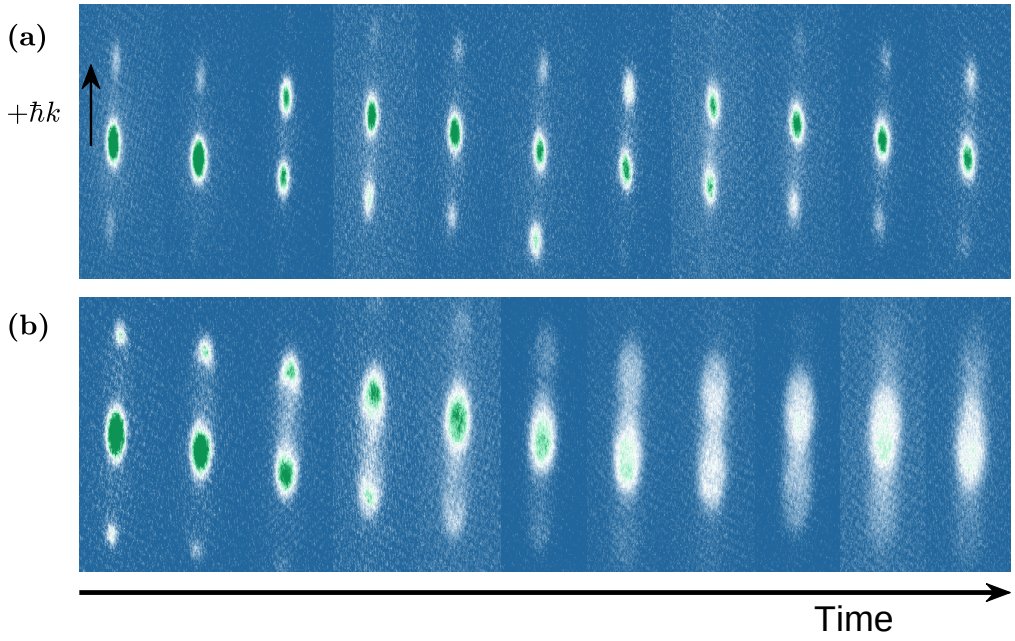

Figure 4.3.: Absorption imaging after TOF for different holding times in the lattice, for a_s=58.8 a_0**(a)** and 83 a_0**(b)**

$T_{BO}^{theory} = 0.469\,\text{ms}$.

In the contact-dominated case (83 a_0, Fig. 4.4(a)), the amplitude of the oscillations of q_{max} decays rapidly and no oscillation is observed after a few periods. We further tried to include a decay in Eq. (4.36) but the fit didn't converge to acceptable results as too many fit variables are needed.

This first analysis already points out the clear effect of interactions in the dephasing of BO. However, a more robust method is needed to have a quantitative understanding.

4.4. Analysing the interaction-induced dephasing

One of the main challenges of this thesis was to find and implement a method to quantify the dephasing of BO as a function of a_s. As seen in Chap. 3, when BO dephases, the width of the momentum distribution increases. By studying the width, we could systematically quantify the dephasing of both theoretical and experimental data. This method relies on finding the right observable for the width. In this section, we review step by step, how the analysis of the dephasing was done and the main results obtained. We show example for two a_s.

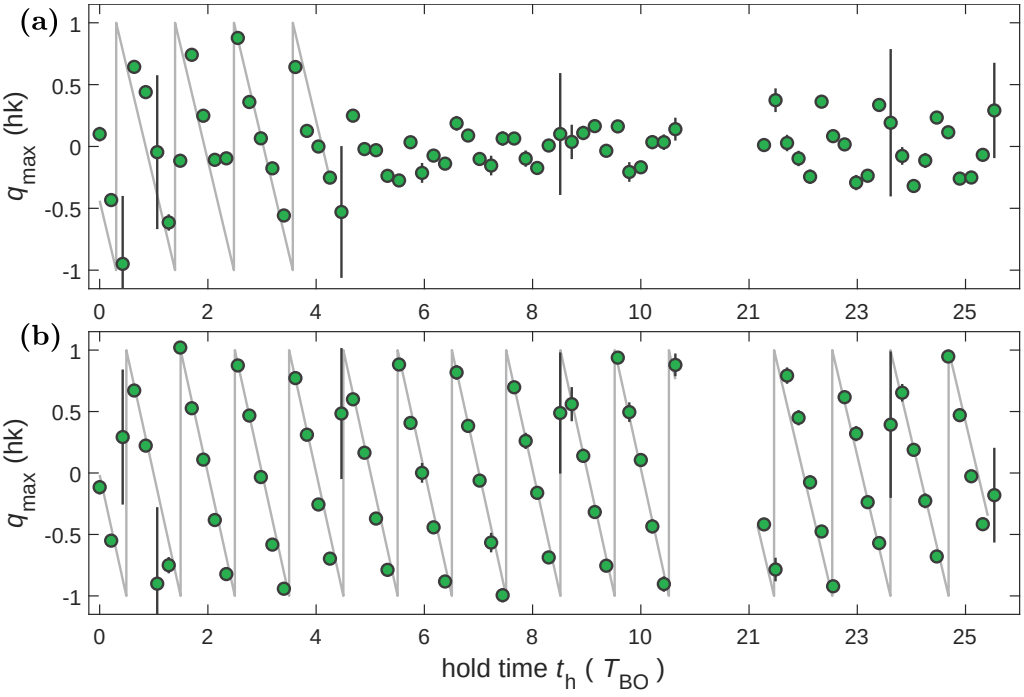

Figure 4.4.: Evolution of the peak position for a_s=83 a_0**(a)** and 58.8 a_0**(b)**. In grey, saw-tooth fit. The error bars correspond to the standard error on the mean over 4-6 repetitions.

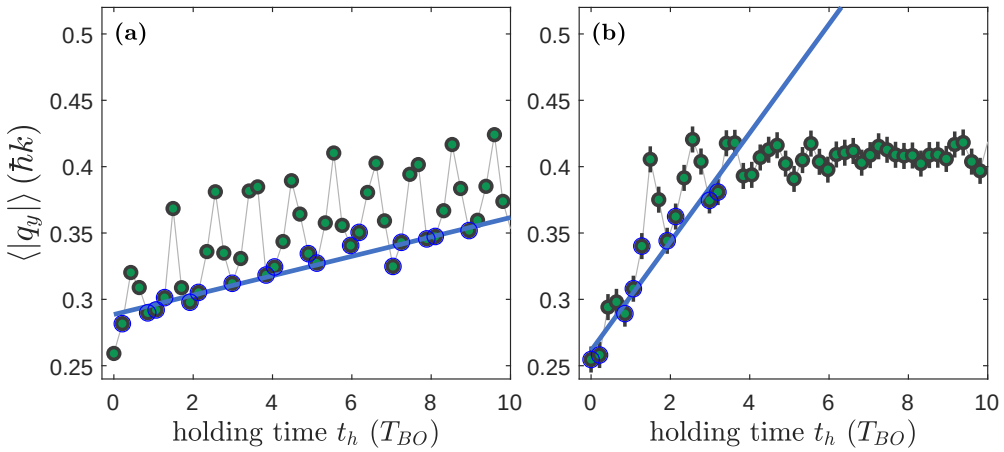

Figure 4.5.: $\langle |q_z| \rangle$ as a function of time t_h for a_s=58.8 a_0**(a)** and 83 a_0**(b)**. With blue edges, the points selected for the fit. The blue line corresponds to the fit result $A(t-\tau)+0.5$

We start with the 1D distribution $n(q_z)$, from it we extract the quantity $\langle |q_z| \rangle$, given by the mathematical expression,

$$\langle |q_z| \rangle = \sum_{q_z} n(q_z) \, |q_z - q_z^{max}| \, , \tag{4.37}$$

with q_{max}, the position of the maximum. This quantity is proportional to the width of the distribution and is less sensitive to noise than the conventional $\langle q_z^2 \rangle$.We consider

that BO are fully dephased when the cloud is spread among all the Brillouin zone, this corresponds to $\langle|q_z|\rangle = 0.5\,\hbar k$. We can easily convince ourselves by taking a fully dephased normalized wave function in theory and calculate $\langle|q_z|\rangle$.

To evaluate the spreading of $\langle|q_z|\rangle$, we fit the first 8 ms with the non-linear model,

$$g(t) = A(t - \tau) + 0.5, \tag{4.38}$$

with A and τ the fitting parameters. We define the dephasing time τ it takes to $g(t)$ to reach $0.5\,\hbar k$. Thus, the above parametrization allows to directly extract the dephasing as a fitting parameter. At the edge of the Brillouin zone, the cloud is split in two and $\langle|q_z|\rangle$ is artificially increased which will lead to underestimation of the dephasing time. Furthermore, we don't want to consider, for the fit, the points when $\langle|q_z|\rangle$ saturates. To take into account all those constraints we select only particular points, following the condition,

$$q_{max} \in [-0.2\,\hbar k, 0.2\,\hbar k] \quad \text{and} \quad \langle|q_z|\rangle < 0.9\,\overline{\langle|q_z|\rangle}_5, \tag{4.39}$$

where $\overline{\langle|q_z|\rangle}_5$ is the average value of the last five $\langle|q_z|\rangle$ for a given scattering length. $\langle|q_z|\rangle$ and the fit associated for two scattering lengths are presented in Fig. 4.5.

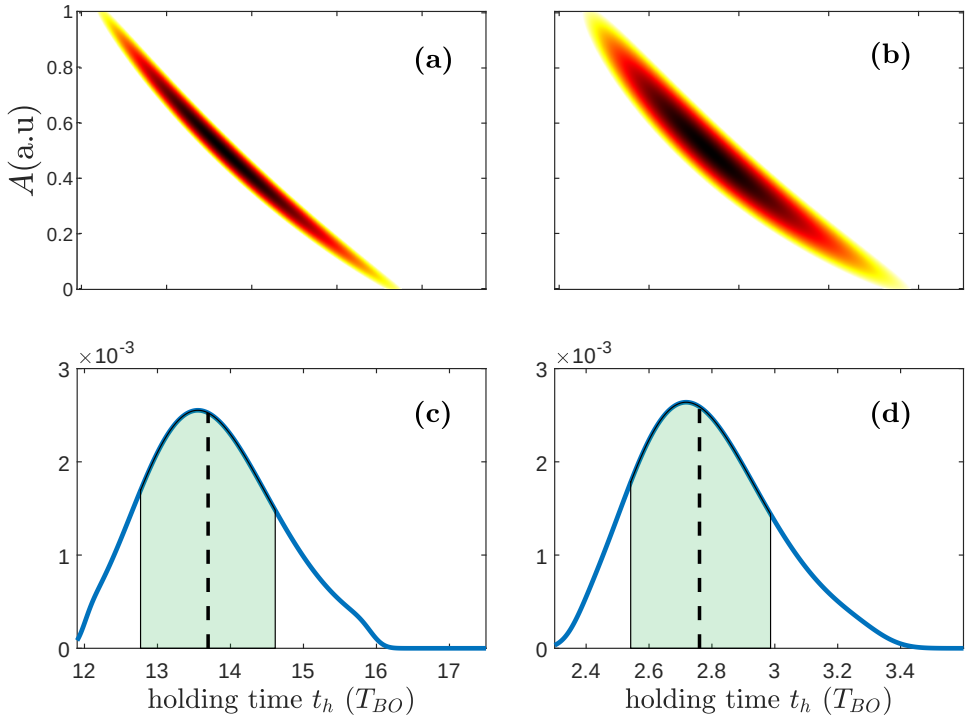

Figure 4.6.: (a,b) χ^2 as a function of the fitting parameters A and τ. **(c,d)** Probability distribution of τ for a_s=58.8 a_0 and a_s=83 a_0

To find the best fitting values, we used the **maximum likelihood** method presented in Ref. [Ifa10]. Close to the standard **least-squares fitting**, this method is based on the minimization of the quantity,

$$\chi^2 = \sum_i \frac{(y_i - g(x_i))^2}{\alpha_i^2}, \tag{4.40}$$

with the data points labelled by (x_i, y_i) and α_i the uncertainty associated. To be consistent with the theoretical data, we fix $\alpha_i = \alpha$ by assuming equal statistical fluctuation around the fitting model and use the expected value $\langle\chi^2\rangle = N_{data} - 2$. This implies,

$$\alpha = \sqrt{\frac{\sum_i (y_i - g(x_i))^2}{N_{data} - 2}} \tag{4.41}$$

$\chi^2(A, \tau)$ is calculated numerically for many values of A and τ and shown in Fig. 4.6 for a_s=58.8 a_0 and a_s=83 a_0. In both cases, χ^2 shows a clear asymmetric shape due to the non-linear fitting model. one consequence of the shape of χ^2 is that the uncertainties associated with τ will also be asymmetric and the linear approximation to calculate the uncertainties can't be applied. A general method to extract uncertainties on multi-variable fits consists in integrating, over all the parameters but one, the function $\exp(-\chi^2/2)$, and after normalization, we obtain a probability distribution. Thus, we get the probability distribution for τ,

$$P_{\chi^2}(\tau) = \frac{\int_A dA e^{-\chi^2(A,\tau)/2}}{\int_{A,\tau} d\tau dA e^{-\chi^2(A,\tau)/2}}. \tag{4.42}$$

We define the uncertainties of τ as the 68% confidence interval. We then convert the dephasing time τ into a dephasing rate $\gamma = 1/\tau$.

To compare the experimental data with the theory predictions, we run the same analysis with the theory data. Due to a variable atom number at different scattering lengths, we vary accordingly the atom number used for the theory.

In the experiment, we estimate the atom number as a function of $a_s$with a linear fit. We account for the fluctuation by taking an interval of ±20% of the experimental BEC atoms number for the theory. For every theory data, we determine the upper (resp. lower) value of τ in the ±20% range. We expand those values with upper (resp. lower) uncertainties on the parameter τ. Thus, we obtain an upper and lower bound of τ as a function of a_s, that we use to create the shaded area in Fig. 4.7.

We also analysed the theory when the Lee-Huang-Yang (Eq. 3.31) is turned to 0 and we obtain the blue dash line in Fig. 4.7.

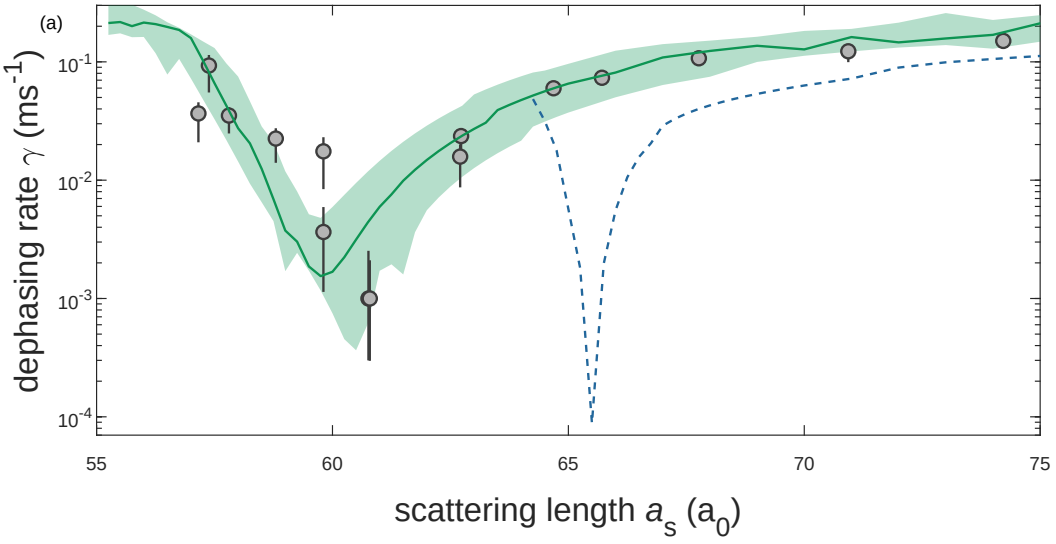

Figure 4.7.: Dephasing rate as a function of a_s. In grey, experimental points with uncertainties. The green line represents the numerical simulations results and the shaded area the uncertainties associated. In blue dashed line, theory prediction without quanum fluctuations.

We observe a minimum of dephasing in agreement with the theory around $60\,a_0$. It is shifted in comparison with the expected mean-field cancellation at $a_{dd} \approx 66\,a_0$. This can be explained by first, the LHY contribution which adds a repulsive term and secondly by the inter-site contribution of the DDI. In fact, we understood that the minimum of dephasing occurs when the variance of chemical potential between each *lattice site* is the smallest. Nevertheless, if we expect a purely interaction-driven dephasing we would expect a symmetric shape in the dephasing rate, but at a low scattering length ($<57\,a_0$) the BO disappear suddenly. This behaviour can't be explained by the effect of the interactions and necissitate a more precise analysis of the initial momentum distribution.

4.5. Ground state: localization in a single lattice plane

As seen previously, for high a_s, the lattice induces two sidepeaks at a position $\pm k$. Nevertheless, when $a_s$crosses $57\,a_0$ the interference patterns desappear suddenly. This behaviour indicates a structural change of the ground state wave function, which can be explained by the localization of the BEC to one *lattice site*. Figure 4.8 shows the transitions around $57\,a_0$. For a_s=$56.7\,a_0$ and $51.7\,a_0$, the ground state already occupies the full Brillouin zone and no BO can be observed. To confirm the localization hypothesis we analyse the interference patterns at $t_h = 0$ as a function of a_s. We associate the absence of sidepeaks with the localization to a single lattice plane.

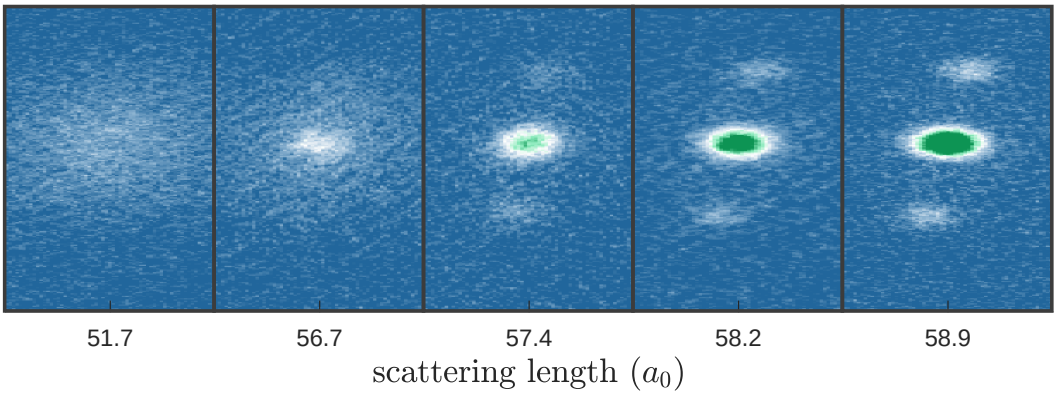

Figure 4.8.: TOF images for 5 scattering lengths around the transition a_s=57 a_0

To quantify the intensity of the sidepeaks, for each picture, we perform a Fourier transform (FT) of the density profile $n(q_z)$. This is done numerically by the fast Fourier transform algorithm (fft). Figure 4.9 (a,b) shows two density profiles for a_s= 56.7 a_0 and 58.9 a_0 and Figure 4.9 (c,d) the Fourier transform associated. fft$[n(q_z)]$ shows many peaks at separated by a distance of $z^* = \lambda_{\mathrm{latt}/2}$. We define the contrast C,

$$C = \frac{\mathrm{fft}[n(q_z)](0)}{\mathrm{fft}[n(q_z)](z^*)} \qquad 4.43$$

When no interference is observed, Fig. 4.9 (b,d), C drops to zero. To compare the results with the theory, we evolve the extended Gross-Pitaevskii equation Eq.(3.31) in imaginary time and apply twice the Fourier transform on the ground state wave function obtained. We then calculate the contrast C in the same way and multiply it by 0.7 to account for the thermal part only present in the experiment.

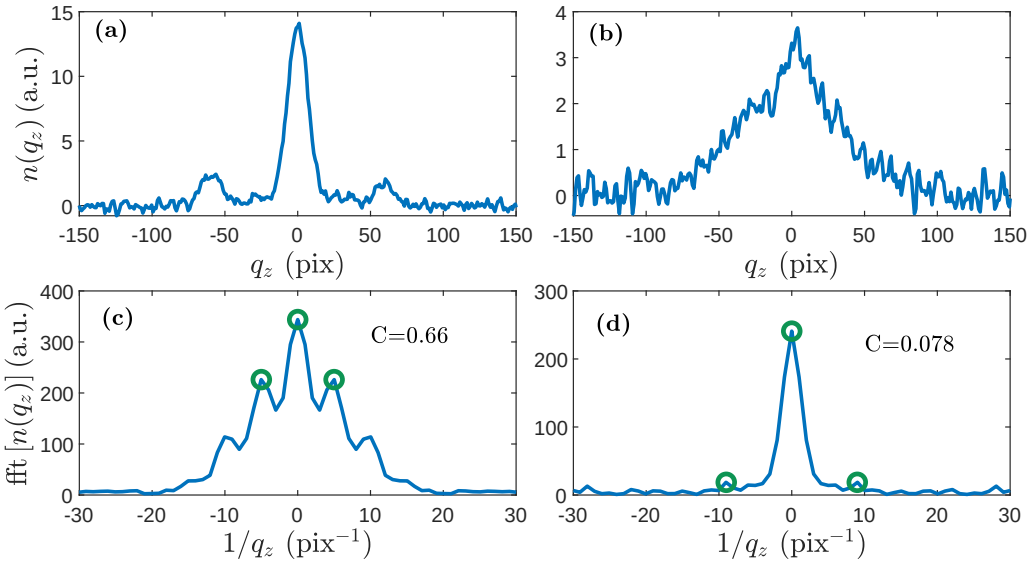

Figure 4.9.: **(a,b)** density profile $n(q_z)$ for a_s=56.7 a_0 and 51.7 a_0. **(c,d)** fourier transform of the density profile $n(q_z)$ for a_s=56.7 a_0 and 51.7 a_0. The green circle represents the intensity peaks fft$[n(q_z)](0)$ and fft$[n(q_z)](z^*)$ used to calculate C.

4.6. Publication: "Strongly dipolar gases in a one-dimensional lattice: Bloch oscillations and matter-wave localization."

Submitted to Communication Physics (2022)[1]
submitted 17 May 2022;

DOI: arXiv:2205.03280
G. Natale,[2] T. Bland,[1] S. Gschwendtner,[1] L. Lafforgue,[1] D. S. Grün,[1] M. J. Mark,[1,2] F. Ferlaino,[1,2]

[1] *Institut für Experimentalphysik, Universität Innsbruck, 6020 Innsbruck, Austria*
[2] *Institut für Quantenoptik und Quanteninformation, Österreichische Akademie der Wissenschaften, 6020 Innsbruck, Austria*

[1] The author of the present thesis contributed to the developement of the experimental procedures together with G. N., A. P., and M. N., performed the measurements together with G. N., D. S. G., S. G., and A. P., analyzed the data with G. N. and contributed in writing the manuscript. The theoretical calculations of this publication have been contributed by S. G, G. N, and T. B..

Strongly dipolar gases in a one-dimensional lattice: Bloch oscillations and matter-wave localization

G. Natale,[1,2] T. Bland,[2] S. Gschwendtner,[2] L. Lafforgue,[2]
D. S. Grün,[2] A. Patscheider,[2] M. J. Mark,[1,2] and F. Ferlaino[1,2]

[1] *Institut für Quantenoptik und Quanteninformation, Österreichische Akademie der Wissenschaften, Technikerstraße 21a, 6020 Innsbruck, Austria*
[2] *Institut für Experimentalphysik, Universität Innsbruck, Technikerstraße 25, 6020 Innsbruck, Austria*

(Dated: May 9, 2022)

Three-dimensional quantum gases of strongly dipolar atoms can undergo a crossover from a dilute gas to a dense macrodroplet, stabilized by quantum fluctuations. Adding a one-dimensional optical lattice creates a platform where quantum fluctuations are still unexplored, and a rich variety of new phases may be observable. We employ Bloch oscillations as an interferometric tool to assess the role quantum fluctuations play in an array of quasi-two-dimensional Bose-Einstein condensates. Long-lived oscillations are observed when the chemical potential is balanced between sites, in a region where a macrodroplet is extended over several lattice sites. Further, we observe a transition to a state that is localized to a single lattice plane–driven purely by interactions–marked by the disappearance of the interference pattern in the momentum distribution. To describe our observations, we develop a discrete one-dimensional extended Gross-Pitaevskii theory, including quantum fluctuations and a variational approach for the on-site wavefunction. This model is in quantitative agreement with the experiment, revealing the existence of single and multisite macrodroplets, and signatures of a two-dimensional bright soliton.

The dipole-dipole interaction (DDI) between magnetic atoms in an ultracold quantum gas has been key to the discovery of supersolids [1–3] and macrodroplets [4, 5], new states of matter with extremely intriguing and counter-intuitive properties [6, 7]. Macrodroplets are macroscopic quantum states that behave in many ways like liquid droplets [4, 5, 8, 9]. They are at least an order of magnitude denser than normal Bose-Einstein condensates (BECs), and can be self-bound. They exist in a parameter regime in which mean-field theories predict the collapse of the entire system when the attractive dipolar interactions overcome the repulsive contact interactions. Instead, the system remains surprisingly stable thanks to the so-called quantum fluctuations, thus providing one of the rare examples where beyond-mean-field interactions substantially change the ground state of the system [10, 11]. Although the functional form of the beyond-mean-field term, otherwise known as the Lee-Huang-Yang (LHY) correction [12], is still subject to intense study and debate [13, 14], its importance is now undoubted. Isolating beyond-mean-field effects may be crucial to settle disputes on its validity, particularly in dipole dominated systems; however, it is very difficult to have access to individual interaction contributions. Though, the differing atom number scaling between mean-field and LHY contributions provide a promising method to differentiate between them.

Optical lattices enable powerful interferometric approaches to, e.g., measure with high precision the zero-crossing of the scattering length or of the mean-field interaction with the so-called Bloch oscillation (BO) technique [15–18], and to achieve an accurate determination of the background scattering length via lattice spectroscopy in Hubbard models [4, 19, 20]. Moreover, the presence of the lattice itself may change completely the phase diagram of the system, as shown in seminal experiments with contact interacting gases [21–23]. Unique phenomena are predicted with the addition of long-range DDIs [24, 25]. Experiments with lattice-confined atomic dipolar gases have already shown important results, e.g., the realization of extended Bose-Hubbard models [26] and spin models [27–30] in three-dimensional (3D) lattices. In 2D lattices, forming quasi-1D tubes, suppression of dipolar relaxation [31] and the controlled breakdown of integrability [32] have been observed. Instead, up to now, 1D lattices, forming an array of quasi-2D layers, have been used with large wavelengths to load a single pancake trap [33], or multi-layer traps to study the role of DDI in the stability against collapse [34]. Further, theoretical proposals have suggested that the DDI between layers not only can lead to modifications within each layer [35–38] but also to inter-layer bound states [39–41]. Other works predict the existence of bright-soliton structures along the lattice [42] or anisotropic on-site solitons [43, 44]. However, those proposals lack the important stabilization mechanism given by the LHY term, which is known to provide many new phases in continuous systems (e.g. harmonically trapped), opening up many questions: What is the ground state of an attractive dipolar gas in a 1D lattice potential? Can droplets be delocalized over many lattice planes? Will solitonic solutions continue to exist?

In the present work, we study an erbium dipolar gas in a 1D optical lattice with dominantly attractive DDI. We employ BOs as an interferometric tool to probe the interaction contributions of the system, and to isolate the role of beyond-mean-field effects. We find long-lived oscillations, associated with a minimum in the dephasing rate, close to the cancellation point between mean-field and beyond-mean-field interactions, and at scatter-

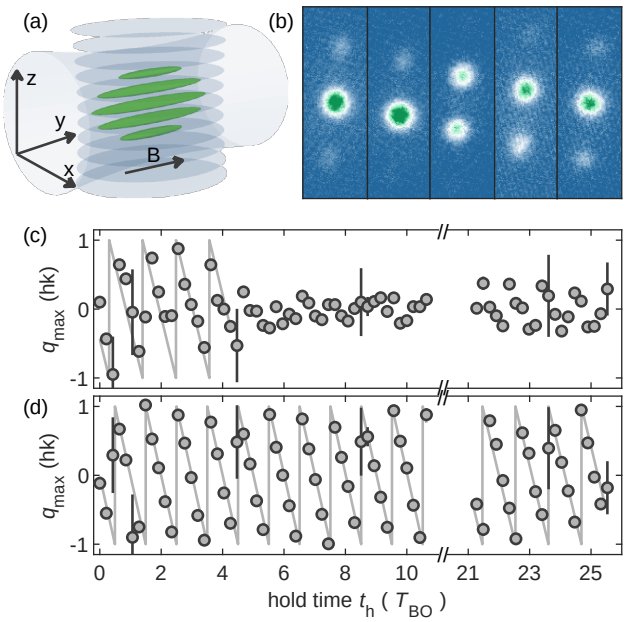

FIG. 1. **Bloch oscillations of a dipolar BEC in a one-dimensional optical lattice. (a)** Sketch of our experiment, consisting of a 1D optical lattice in the z-direction, loaded with an erbium BEC from an optical dipole trap with trapping frequencies $\omega_{x,y,z} = 2\pi \times (240(3), 30(3), 217(1))$ Hz. Gravity acts along z. **(b)** Absorption images after TOF showing the momentum distributions during one Bloch cycle. **(c,d)** Evolution of the peak position of the momentum distribution for $a_s = (71.6(1.0),\ 59.8(1.0))\, a_0$, respectively. A sawtooth fit (solid grey) to the data yields $T_{BO} = 0.469(4)$ ms, consistent with the expected value $T_{BO} = 2k/(mg_{grav})$. The error bars represent the standard error on the mean over 4-6 repetitions.

ing lengths significantly shifted from the expected mean-field result. We develop a discrete effective 1D extended Gross-Pitaevskii equation (eGPE) with variational transverse widths [45, 46]. We find that this minimum occurs when the chemical potentials on each site are equal, not the energies–as has been employed successfully in contact interaction dominated systems [17, 18]–due to the difference in density scaling between the interactions. The close correspondence between theory and experiment shows the validity of the LHY prediction, even while highly inhomogeneous densities are expected to break the local density approximation [12]. Moreover, we see that for low scattering lengths the system undergoes a structural transition to a single localized 2D plane, signifying an important new way to generate systems in reduced geometries through varying the interactions alone. Finally, using our theoretical model we produce a full phase diagram of the system, revealing the impact of the LHY contribution to the predicted 2D anisotropic soliton state [43], which is instead morphed into a droplet solution at high atom numbers. Though, promisingly, we still find soliton-like solutions exist.

In the experiment, we prepare a degenerate dipolar gas of erbium atoms in a one-dimensional optical lattice as follows. We start with a dipolar quantum gas of 5×10^4 spin-polarized ^{166}Er atoms confined in a cigar-shaped optical dipole trap [47] elongated along y. Typical BEC fractions range from 60% to 80%. The dipolar length for ^{166}Er is fixed at $a_{dd} = 66.5\, a_0$, where a_0 is the Bohr radius. We tune the contact interaction between atoms and therefore the s-wave scattering length, a_s, via Feshbach resonances [4, 48–50] by changing the absolute value of a bias magnetic field $|\mathbf{B}|$. We fix the orientation of $\mathbf{B}$ to be along the weak axis (y) of the trap, making the DDI dominantly attractive [4, 7].

Once the harmonically-trapped cloud is prepared at the desired a_s, we switch on a 1D optical lattice, aligned along the gravity direction (z); see Fig. 1(a). The vertical lattice is created by retro-reflecting a $\lambda = 1064$ nm laser beam. We load the planes by exponentially increasing the lattice depth V_0 to $8\, E_{rec}$ in 20 ms, where $E_{rec} = \hbar^2 k^2/2m = h \times 10.5$ kHz. Here, $\hbar = h/2\pi$ is the reduced Planck's constant (h), m is the mass of ^{166}Er atoms and $k = 2\pi/\lambda$ is the wave-vector of the lattice. The 1D lattice forms an array of tightly confined quasi-2D planes with a trap frequency along the tight direction $\omega_z \simeq 2\pi \times 6$ kHz, corresponding to an harmonic oscillator length $z_{ho} = 100$ nm. The tunnelling rate, J, between planes is about $h \times 33$ Hz. For these 1D lattice parameters, $\hbar\omega_z > k_B T$ and the system is kinematically 2D [51].

We first aim at inducing Bloch oscillations to interferometrically assess the role of beyond-mean-field effects and test the validity of the LHY term. We thus suddenly switch off the dipole trap and let the system evolve in the combined lattice and gravitational potential for a variable hold time t_h. Finally, using standard absorption imaging after 30 ms of time-of-flight (TOF), we record the evolution of the momentum distribution and extract the position of the main peak, q_{max}, as a function of t_h. Figure 1(b) shows an exemplary set of absorption images during a single Bloch period T_{BO}. We observe the key paradigm of BOs, i.e. the linear increase of the mean momentum due to the acceleration and the Bragg reflection occurring at the border of the Brillouin zone [52], well described by fitting a sawtooth function to q_{max}.

The high sensitivity of BOs to interactions [17, 53] clearly appears by tracing the evolution for two different a_s (see Fig. 1(c,d)), as the interaction dependence is encoded into the dephasing rate. For a contact-dominated gas ($a_{dd} < a_s = 90\, a_0$, Fig. 1(c)), we see that the BOs vanish within a few T_{BO}. On the contrary, decreasing a_s, and thereby going into the regime where contact interactions and DDI nearly compensate each other ($a_s = 60\, a_0$, Fig. 1(d)), we observe persisting oscillations for more than 25 Bloch cycles, set by our limited observation time [50]. To systematically study this effect, we repeat the BO measurements for different values of a_s, and extract the corresponding dephasing rate γ [50]. As shown in Fig. 2(a), we observe a resonant-type behavior with γ showing a pronounced dip with a minimum at

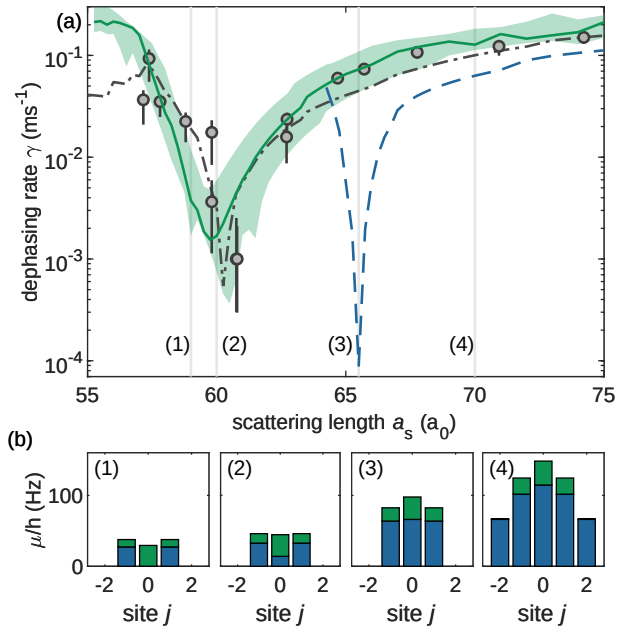

FIG. 2. **Dephasing rate and chemical potential distributions. (a)** Experimental dephasing rate γ (circles) as a function of scattering length a_s. The green solid line shows the theory result, with an uncertainty region (shaded area) accounting for 20% atom number variation. The blue dashed line shows the theory expectation without LHY. The gray dot-dashed line gives the prediction of the semi-analytic approximation for γ. Error bars show the 68% confidence interval [50]. **(b)** Chemical potential per lattice site μ_j extracted from the discrete model for $a_s = (59, 60, 65.5, 70)\,a_0$ (1, 2, 3, 4). The green area depicts the LHY contribution to μ_j.

$a_s = 61\,a_0$. This minimum is clearly different to the point $a_s \approx a_{dd}$, where the variance of the mean-field energies across different lattice sites cancel [18], which would be expected from previous observations [17, 53].

To get further insight on the origin of the minimum, we develop a discrete effective 1D eGPE, inspired by the close correspondence between predictions from discrete models and experimental observations in non-dipolar [54, 55] and weakly dipolar [18] BECs. We separate the 3D wavefunction into radial and axial contributions, allowing for a variational anisotropic radial width and thus maintaining the 3D character [45]. Along the lattice direction (z), we further decompose the wavefunction, $\psi(z,t)$, as a sum of Wannier functions $w(z)$ of the lowest energy band over all lattice sites: $\psi(z,t) = \sqrt{N}\sum_j c_j(t)w(z-z_j)$, where N is the atom number and $c_j(t)$ the complex wavefunction amplitude on lattice site j, leading to a set of discrete effective 1D eGPEs, each including mean-field and beyond mean-field interactions. For the beyond-mean-field interaction, the 3D form of the LHY still fully applies since the contact interaction energy exceed the confinement energy scale [50, 56]. However, our system may also open to further studies on the 2D to 3D crossover of the LHY. We solve these equations coupled to a minimization of the energy functional with respect to the variational parameters to determine the ground states, benchmarking them against the full 3D theory. We then perform dynamic simulations of the expected time evolution [50], giving an accurate dephasing rate (solid line) in Fig. 2(a) without free parameters.

In previous studies, the point of minimum dephasing was found to occur when the mean-field interaction energies vanish or cancel. We isolate the mean-field contribution by removing beyond-mean-field effects from our simulations (dashed line in Fig. 2(a)), predicting a minimum at $a_s \approx a_{dd}$. However, this is in clear contradiction with our experimental observations by a shift of $6a_0$ and a different overall shape due to the different scaling of the LHY term with the density. Without LHY, the cancellation of mean-field energies, E^j_{MF}, is equivalent to the cancellation of onsite chemical potentials, given by $\mu_j = 2E^j_{MF}/|c_j|^2$. Note, μ_j dictates the wavefunction phase winding on each site through $c_j = |c_j|e^{-i\mu_j t/\hbar}$. Reintroducing quantum fluctuations, we obtain $\mu_j = (2E^j_{MF} + 5/2E^j_{BMF})/|c_j|^2$, where the 5/2 appears due to the $|c_j|^5$ density scaling in the beyond-mean-field energy (E^j_{BMF}). Figure 2(b) shows μ_j from the ground state calculation for four scattering lengths, additionally indicating the contribution of the LHY correction.

We observe that the point of minimal dephasing in the experiment is close to the point where the variance of μ_j is minimized [57]. Indeed, within a semi-analytic approximation (see Ref. [50] for details), we find a direct relationship between γ and μ_j, which reads $\gamma \propto |\mu_1 - \mu_0|$ when 3 lattice sites ($j = -1, 0, 1$) are occupied. This model can be extended to 5 lattice sites, giving the dot-dashed line (Fig. 2(a)) which reproduces very well the system behaviour [50]. Interestingly, measuring the dephasing rate through the chemical potential is ubiquitous to systems with arbitrary interaction potentials.

Surprisingly, by further decreasing the scattering length below $57\,a_0$, no BOs nor interference peaks are visible anymore. We observe at the initial instant ($t_h = 0$ ms) that the momentum distribution is already spread over the entire first Brillouin zone. To quantify this, we study the contrast, C, of the interference pattern of the initial momentum distribution as a function of a_s, see Figure 3(a). We extract C, defined as the amplitude of the momentum peaks at $\pm 2\hbar k$ relative to the zero momentum peak, from the Fourier analysis of the TOF images [50]. For large a_s, we observe the typical matter-wave interference pattern, as expected from a coherent state populating several lattice planes (see inset) [55]. As we lower a_s, C first remains fairly constant. For a_s below a certain critical value $a_s^* \approx 57\,a_0$, we observe a sudden loss of the interference pattern with a sharp decrease of C to almost zero.

Remarkably, we observe that this interaction-driven process is reversible. To test the restoring of the interference pattern, we employ the following protocol [50]: In brief, we first prepare the system in the lattice at constant

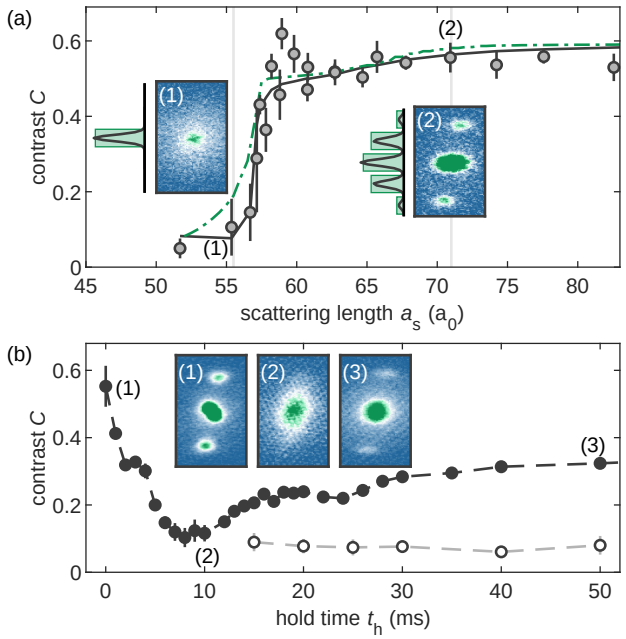

FIG. 3. **Interaction-induced localization. (a)** Contrast of the interference pattern after loading the lattice at different a_s. The green dot-dashed (black solid) line represents the result of the 1D discrete model (3D eGPE) multiplied by 0.7. The insets show the respective density distributions along z of the 1D discrete model (bars) and 3D eGPE (lines) and corresponding experimental averaged interference patterns after TOF expansion (1,2). **(b)** Dynamic evolution of the contrast quenching back (filled circles) or holding a_s (open circles); see text. The error bars represent the standard error on the mean over 4-6 repetitions.

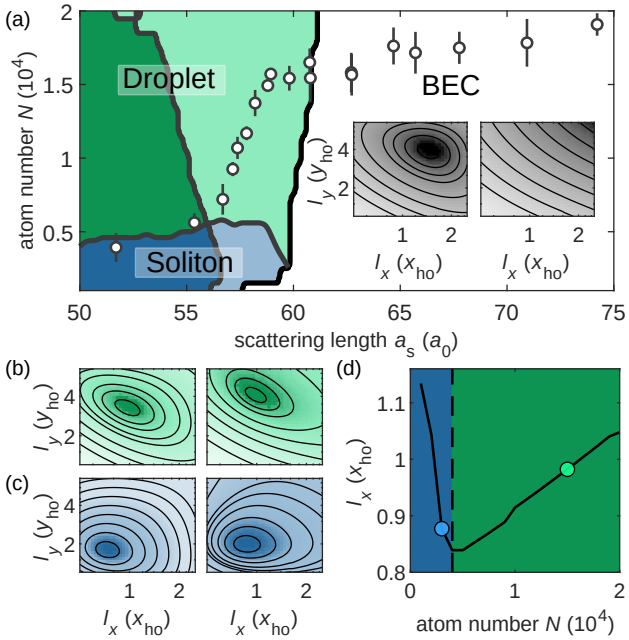

FIG. 4. **Phase diagram and energy landscapes. (a)** Phase diagram as a function of a_s and atom number. The white region denotes a trap-bound BEC extended over several lattice sites. The colored regions denote quasi-2D self-bound solutions: a droplet (green), a soliton (blue), each either extended over several lattice sites (lighter shade) or localized (darker shade, >95% of the atoms are localized in the central lattice plane). Circles show our experimental data points from Fig. 3(a). **Inset (a), (b-c)** Energy landscapes as a function of the radial widths l_x and l_y, in units of the radial harmonic oscillator lengths $x_{ho} = 0.50(1)\,\mu m$ and $y_{ho} = 1.42(1)\,\mu m$, respectively, with (left) and without (right) the radial harmonic trap, for (inset (a)) BEC (a_s, N) = ($70\,a_0$, 1.5×10^4), (b) droplet (a_s, N) = ($65\,a_0$, 1.5×10^4) and (c) soliton (a_s, N) = ($51.5\,a_0$, 0.4×10^4) regimes, with darker shading at the minima. **(d)** Radial width l_x versus N for $a_s = 51.5\,a_0$. The dashed line indicates the soliton-to-droplet transition point, and the circles indicate the position of (b-c).

and large a_s ($a_s = 69(2)\,a_0$). We then ramp down a_s below a_s^* ($a_s = 56(2)\,a_0$) in 20 ms and wait until C stabilizes to a small value; see Fig. 3(b). Note that the interference pattern disappears after about 10 ms, which is on the order of the tunneling time h/J between two neighboring lattice sites. At this point, we quench a_s back to its initial value and probe the time evolution of the system towards its new equilibrium state. On a similar timescale, we observe the reappearance of the interference pattern with an increase of C, which then saturates to about 60% of its initial value [58]. For comparison, we also show the data without inverting the field ramp.

The observed broad distribution in reciprocal space suggests that the system ground state has undergone a structural change, with the macroscopic wavefunction localized in one lattice plane. To verify this interpretation, we calculate the ground state of the system as a function of a_s. When the repulsive contact interaction dominates ($a_s > a_{dd}$), we find an array of BECs occupying approximately three to five lattice planes; see insets Fig. 3(a). In contrast, when the relative strength of the attractive dipolar interaction with respect to the other terms in the Hamiltonian is increased, the system reaches a critical point. Here, it undergoes a phase transition to a quasi-2D state, in which all atoms are localized into a single lattice plane to minimize their energy. This purely interaction-driven phase transition–somewhat reminiscent of a continuous version of a superfluid to Mott insulator transition [59]–is stabilized by quantum fluctuations (LHY), preventing the subsequent collapse of the system [42, 60]. The predicted critical point occurs exactly where we observe the disappearance of the interference pattern in the experiments. We find an overall excellent agreement between the measured and the calculated C from both the discrete 1D model and the 3D theory without any free fitting parameters, except for a rescaling factor to the contrast amplitude to account for the thermal atoms in the experiment.

The observation of this phase transition to a quasi-2D localized state driven by interactions points to the existence of a rich variety of phases. The importance of

the LHY correction and its peculiar density scaling motivate us to investigate the properties of the ground state as a function of a_s and atom number to identify distinct phases in this unique setting. For this, we employ our discrete model to derive a full phase diagram; see Fig. 4(a). To investigate the boundness of the states, we assess the impact of the radial harmonic trap on the minimum of the variational energy, which is a function of the radial widths l_x and l_y. At large scattering lengths, as expected, we find a stable delocalized BEC phase, where the total interaction energy (mean-field + LHY) is positive. The state is trap-bound, meaning that there is no energy minimum without the radial harmonic confinement; inset of Fig. 4(a).

Reducing a_s, we find an energy minimum even without the radial harmonic trap (colored region in the phase diagram). These quasi-2D self-bound solutions (the lattice still provides axial confinement) are either extended over several sites (lighter color) or localized to a single plane (darker color). In the literature, there are two paradigmatic examples of self-bound objects with attractive mean-field energy: droplets and solitons. Droplets can exist in one, two or three dimensions and are stabilized through the LHY correction [7]. Stable bright solitons only exist in quasi-1D systems with attractive contact interactions and are stabilized against collapse purely by kinetic energy. In the search for solitons in higher dimensions, theoretical studies have suggested that the DDI could stabilize such 2D solutions [43, 44]. To the best of our knowledge, there have been no studies on the effect the LHY correction has on this prediction, nor experimental observation. In the present case, where many interactions and kinetic energy compete, a classification of self-bound solutions is much less straightforward. As a crucial distinction between a soliton and a droplet, we use the scaling of the system width with atom number. The soliton width (along the collapse direction) scales inversely with increasing atom number [61], while in contrast, the droplet size increases in all directions with N [62], as predicted in a quasi-1D setting [63]. We use this distinction to draw a boundary between the two phases, observing a phase transition at around 5000 atoms, for both single-site and multi-site solitons. The overlaying of our measurements (Fig.3(a)) onto the phase diagram suggests that the experiments have already reached the interesting regimes of both 2D self-bound droplet and dipolar solitons. This opens the door to future experimental investigation on the self-bound nature and properties of these new 2D phases.

In conclusion, we theoretically and experimentally investigate the behavior of a strongly dipolar quantum gas in a 1D optical lattice. We employ BOs and characterize their dephasing rate as a function of a_s. We observe a minimum in the dephasing shifted $6\,a_0$ away from the purely mean-field prediction, providing an interferometric measure of the beyond-mean-field contribution. For low enough a_s, the system enters into a quasi-2D state which is localized onto a single lattice plane, providing a genuine interaction-driven path to reach reduced dimensions in dipolar gases. Using our developed discrete theory model, we derive a full phase diagram which confirms the observed localization transition. This also reveals signatures of quasi-2D self-bound dipolar droplet solutions, and the long sought-after 2D anisotropic dipolar soliton, first predicted in Ref. [43] (see also [44, 64]). Our work paves the way for future studies of the soliton-to-droplet crossover in a dipolar gas, as observed in a Bose-Bose gas [65], and of the "solitonic" nature [66] of dipolar solitary waves [67–71].

ACKNOWLEDGMENTS

We thank R. N. Bisset, A. Houwman, L. Lavoine, R. Grimm, and L. Tarruell for stimulating discussions, and B. Yang for his support in the early stage of the experiment. This work is financially supported through an ERC Consolidator Grant (RARE, no. 681432) and a DFG/FWF (FOR 2247/I4317-N36). We also acknowledge the Innsbruck Laser Core Facility, financed by the Austrian Federal Ministry of Science, Research and Economy. Part of the computational results presented have been achieved using the HPC infrastructure LEO of the University of Innsbruck.

* Correspondence and requests for materials should be addressed to Francesca.Ferlaino@uibk.ac.at.

[1] L. Tanzi, E. Lucioni, F. Famà, J. Catani, A. Fioretti, C. Gabbanini, R. N. Bisset, L. Santos, and G. Modugno, Phys. Rev. Lett. **122**, 130405 (2019).
[2] F. Böttcher, J.-N. Schmidt, M. Wenzel, J. Hertkorn, M. Guo, T. Langen, and T. Pfau, Phys. Rev. X **9**, 011051 (2019).
[3] L. Chomaz, D. Petter, P. Ilzhöfer, G. Natale, A. Trautmann, C. Politi, G. Durastante, R. M. W. van Bijnen, A. Patscheider, M. Sohmen, M. J. Mark, and F. Ferlaino, Phys. Rev. X **9**, 021012 (2019).
[4] L. Chomaz, S. Baier, D. Petter, M. J. Mark, F. Wächtler, L. Santos, and F. Ferlaino, Phys. Rev. X **6**, 041039 (2016).
[5] M. Schmitt, M. Wenzel, F. Böttcher, I. Ferrier-Barbut, and T. Pfau, Nature **539**, 259 (2016).
[6] M. A. Norcia and F. Ferlaino, Nature Physics **17**, 1349 (2021).
[7] L. Chomaz, I. Ferrier-Barbut, F. Ferlaino, B. Laburthe-Tolra, B. L. Lev, and T. Pfau, arXiv preprint (2022), arXiv:2201.02672.
[8] C. R. Cabrera, L. Tanzi, J. Sanz, B. Naylor, P. Thomas, P. Cheiney, and L. Tarruell, Science **359**, 301 (2018).

[9] G. Semeghini, G. Ferioli, L. Masi, C. Mazzinghi, L. Wolswijk, F. Minardi, M. Modugno, G. Modugno, M. Inguscio, and M. Fattori, Phys. Rev. Lett. **120**, 235301 (2018).
[10] D. S. Petrov, Phys. Rev. Lett. **115**, 155302 (2015).
[11] D. Baillie, R. M. Wilson, R. N. Bisset, and P. B. Blakie, Phys. Rev. A **94**, 021602 (2016).
[12] A. R. P. Lima and A. Pelster, Phys. Rev. A **84**, 041604 (2011).
[13] V. Cikojević, L. V. Markić, G. Astrakharchik, and J. Boronat, Phys. Rev. A **99**, 023618 (2019).
[14] M. Ota and G. Astrakharchik, SciPost Phys. **9**, 20 (2020).
[15] G. Roati, E. de Mirandes, F. Ferlaino, H. Ott, G. Modugno, and M. Inguscio, Phys. Rev. Lett. **92**, 230402 (2004).
[16] G. Ferrari, N. Poli, F. Sorrentino, and G. M. Tino, Phys. Rev. Lett. **97**, 060402 (2006).
[17] M. Gustavsson, E. Haller, M. J. Mark, J. G. Danzl, G. Rojas-Kopeinig, and H.-C. Nägerl, Phys. Rev. Lett. **100**, 080404 (2008).
[18] M. Fattori, G. Roati, B. Deissler, C. D'Errico, M. Zaccanti, M. Jona-Lasinio, L. Santos, M. Inguscio, and G. Modugno, Phys. Rev. Lett. **101**, 190405 (2008).
[19] S. Baier, D. Petter, J. H. Becher, A. Patscheider, G. Natale, L. Chomaz, M. J. Mark, and F. Ferlaino, Phys. Rev. Lett. **121**, 093602 (2018).
[20] A. Patscheider, L. Chomaz, G. Natale, D. Petter, M. Mark, S. Baier, B. Yang, R. Wang, J. Bohn, and F. Ferlaino, arXiv preprint (2021), arXiv:2112.11883.
[21] I. Bloch, J. Dalibard, and W. Zwerger, Rev. Mod. Phys. **80**, 885 (2008).
[22] I. Bloch, J. Dalibard, and S. Nascimbène, Nat. Phys. **8**, 267 (2012).
[23] C. Gross and I. Bloch, Science **357**, 995 (2017).
[24] C. Trefzger, C. Menotti, B. Capogrosso-Sansone, and M. Lewenstein, Journal of Physics B: Atomic, Molecular and Optical Physics **44**, 193001 (2011).
[25] O. Dutta, M. Gajda, P. Hauke, M. Lewenstein, D.-S. Lühmann, B. A. Malomed, T. Sowiński, and J. Zakrzewski, Reports on Progress in Physics **78**, 066001 (2015).
[26] S. Baier, M. J. Mark, D. Petter, K. Aikawa, L. Chomaz, Z. Cai, M. Baranov, P. Zoller, and F. Ferlaino, Science **352**, 201 (2016).
[27] A. de Paz, A. Sharma, A. Chotia, E. Maréchal, J. H. Huckans, P. Pedri, L. Santos, O. Gorceix, L. Vernac, and B. Laburthe-Tolra, Phys. Rev. Lett. **111**, 185305 (2013).
[28] S. Lepoutre, J. Schachenmayer, L. Gabardos, B. Zhu, B. Naylor, E. Marechal, O. Gorceix, A. M. Rey, L. Vernac, and B. Laburthe-Tolra, Nature Communications **10**, 1714 (2019).
[29] L. Gabardos, B. Zhu, S. Lepoutre, A. M. Rey, B. Laburthe-Tolra, and L. Vernac, Phys. Rev. Lett. **125**, 143401 (2020).
[30] A. Patscheider, B. Zhu, L. Chomaz, D. Petter, S. Baier, A.-M. Rey, F. Ferlaino, and M. J. Mark, Phys. Rev. Research **2**, 023050 (2020).
[31] B. Pasquiou, G. Bismut, E. Maréchal, P. Pedri, L. Vernac, O. Gorceix, and B. Laburthe-Tolra, Phys. Rev. Lett. **106**, 015301 (2011).
[32] Y. Tang, W. Kao, K.-Y. Li, S. Seo, K. Mallayya, M. Rigol, S. Gopalakrishnan, and B. L. Lev, Phys. Rev. X **8**, 021030 (2018).
[33] T. Koch, T. Lahaye, J. Metz, B. Frohlich, A. Griesmaier, and T. Pfau, Nat. Phys. **4**, 218 (2008).
[34] S. Müller, J. Billy, E. A. L. Henn, H. Kadau, A. Griesmaier, M. Jona-Lasinio, L. Santos, and T. Pfau, Phys. Rev. A **84**, 053601 (2011).
[35] P. Köberle and G. Wunner, Phys. Rev. A **80**, 063601 (2009).
[36] M. Klawunn and L. Santos, Phys. Rev. A **80**, 013611 (2009).
[37] R. M. Wilson and J. L. Bohn, Phys. Rev. A **83**, 023623 (2011).
[38] M. Rosenkranz, Y. Cai, and W. Bao, Phys. Rev. A **88**, 013616 (2013).
[39] D.-W. Wang, Phys. Rev. Lett. **98**, 060403 (2007).
[40] C. Trefzger, C. Menotti, and M. Lewenstein, Phys. Rev. Lett. **103**, 035304 (2009).
[41] A. Macia, G. E. Astrakharchik, F. Mazzanti, S. Giorgini, and J. Boronat, Phys. Rev. A **90**, 043623 (2014).
[42] G. Gligorić, A. Maluckov, L. c. v. Hadžievski, and B. A. Malomed, Phys. Rev. A **78**, 063615 (2008).
[43] I. Tikhonenkov, B. A. Malomed, and A. Vardi, Phys. Rev. Lett. **100**, 090406 (2008).
[44] M. Raghunandan, C. Mishra, K. Łakomy, P. Pedri, L. Santos, and R. Nath, Phys. Rev. A **92**, 013637 (2015).
[45] P. B. Blakie, D. Baillie, and S. Pal, Communications in Theoretical Physics **72**, 085501 (2020).
[46] P. Blakie, D. Baillie, L. Chomaz, and F. Ferlaino, Physical Review Research **2**, 043318 (2020).
[47] K. Aikawa, A. Frisch, M. Mark, S. Baier, A. Rietzler, R. Grimm, and F. Ferlaino, Phys. Rev. Lett. **108**, 210401 (2012).
[48] C. Chin, R. Grimm, P. S. Julienne, and E. Tiesinga, Rev. Mod. Phys. **82**, 1225 (2010).
[49] A. Frisch, M. Mark, K. Aikawa, F. Ferlaino, J. L. Bohn, C. Makrides, A. Petrov, and S. Kotochigova, Nature **507**, 475 (2014).
[50] See Supplemental Material at [URL] for details on the experimental setup, measurement schemes, analysis and theory calculations. (2022).
[51] D. S. Petrov and G. V. Shlyapnikov, Phys. Rev. A **64**, 012706 (2001).
[52] M. Ben Dahan, E. Peik, J. Reichel, Y. Castin, and C. Salomon, Phys. Rev. Lett. **76**, 4508 (1996).
[53] M. Fattori, C. D'Errico, G. Roati, M. Zaccanti, M. Jona-Lasinio, M. Modugno, M. Inguscio, and G. Modugno, Phys. Rev. Lett. **100**, 080405 (2008).
[54] L. Fallani, C. Fort, and M. Inguscio, in *Advances in Atomic, Molecular, and Optical Physics*, Vol. 56 (Academic Press, 2008) pp. 119–160.
[55] O. Morsch and M. Oberthaler, Rev. Mod. Phys. **78**, 179 (2006).
[56] P. Zin, M. Pylak, T. Wasak, K. Jachymski, and Z. Idziaszek, Journal of Physics B: Atomic, Molecular and Optical Physics **54**, 165302 (2021).
[57] The total (MF + LHY) interaction energies cancel at $62a_0$.
[58] The contrast is not fully recovered, which we attribute to the effect of inelastic losses.
[59] M. Greiner, O. Mandel, T. Esslinger, T. W. Hänsch, and I. Bloch, Nature (London) **415**, 39 (2002).
[60] A. Maluckov, L. c. v. Hadžievski, B. A. Malomed, and L. Salasnich, Phys. Rev. A **78**, 013616 (2008).
[61] A. Shabat and V. Zakharov, Sov. Phys. JETP **34**, 62 (1972).
[62] S. Pal, D. Baillie, and P. Blakie, Physical Review A **105**, 023308 (2022).

[63] M. Edmonds, T. Bland, and N. Parker, J. Phys. Comm. **4**, 125008 (2020).
[64] P. Pedri and L. Santos, Phys. Rev. Lett. **95**, 200404 (2005).
[65] P. Cheiney, C. R. Cabrera, J. Sanz, B. Naylor, L. Tanzi, and L. Tarruell, Phys. Rev. Lett. **120**, 135301 (2018).
[66] P. G. Drazin and R. Johnson, *Solitons: an introduction*, Vol. 2 (Cambridge university press, 1989).
[67] J. Cuevas, B. A. Malomed, P. Kevrekidis, and D. Frantzeskakis, Physical Review A **79**, 053608 (2009).
[68] R. Eichler, D. Zajec, P. Köberle, J. Main, and G. Wunner, Physical Review A **86**, 053611 (2012).
[69] S. K. Adhikari, Physical Review A **90**, 055601 (2014).
[70] B. Baizakov, S. Al-Marzoug, and H. Bahlouli, Physical Review A **92**, 033605 (2015).
[71] M. Edmonds, T. Bland, R. Doran, and N. Parker, New Journal of Physics **19**, 023019 (2017).
[72] F. Wächtler and L. Santos, Phys. Rev. A **93**, 061603 (2016).
[73] R. N. Bisset, R. M. Wilson, D. Baillie, and P. B. Blakie, Phys. Rev. A **94**, 033619 (2016).
[74] I. Ferrier-Barbut, H. Kadau, M. Schmitt, M. Wenzel, and T. Pfau, Phys. Rev. Lett. **116**, 215301 (2016).
[75] H.-Y. Lu, H. Lu, J.-N. Zhang, R.-Z. Qiu, H. Pu, and S. Yi, Phys. Rev. A **82**, 023622 (2010).
[76] D. S. Petrov and G. E. Astrakharchik, Phys. Rev. Lett. **117**, 100401 (2016).
[77] T. Ilg, J. Kumlin, L. Santos, D. S. Petrov, and H. P. Büchler, Physical Review A **98**, 051604 (2018).
[78] L. Lavoine and T. Bourdel, Phys. Rev. A **103**, 033312 (2021).
[79] D. Edler, C. Mishra, F. Wächtler, R. Nath, S. Sinha, and L. Santos, Phys. Rev. Lett. **119**, 050403 (2017).
[80] A. Boudjemâa, New Journal of Physics **21**, 093027 (2019).
[81] D. Witthaut, M. Werder, S. Mossmann, and H. J. Korsch, Phys. Rev. E **71**, 036625 (2005).
[82] O. Morsch, J. H. Müller, M. Cristiani, D. Ciampini, and E. Arimondo, Phys. Rev. Lett. **87**, 140402 (2001).

Supplemental materials: Strongly dipolar gases in a one-dimensional lattice: Bloch oscillations and matter-wave localization

G. Natale, T. Bland, S. Gschwendtner, L. Lafforgue, D. S. Grün, A. Patscheider, M. J. Mark, and F. Ferlaino

THEORETICAL MODEL

In this work, we use an extended Gross-Pitaevskii theory for direct comparison to our experimental results. We employ both the standard three-dimensional form of the extended Gross-Pitaevskii equation (eGPE) and derive a discrete effective one-dimensional eGPE. Starting with the three-dimensional case, our system can be described by the 3D eGPE of the form [4, 72–74]

$$i\hbar\frac{\partial}{\partial t}\Psi(\vec{x},t) = \Big[-\frac{\hbar^2}{2m}\nabla^2 + V_{\mathrm{harm}}(\vec{x}) + V_{\mathrm{latt}}(z) - F_{\mathrm{ext}}z + g|\Psi(\vec{x},t)|^2 + \int \mathrm{d}^3\vec{x}'\, U_{\mathrm{dd}}(\vec{x}-\vec{x}')|\Psi(\vec{x}',t)|^2 + \gamma_{\mathrm{QF}}|\Psi(\vec{x},t)|^3\Big]\Psi(\vec{x},t)\,, \tag{S1}$$

where the wavefunction Ψ is normalized to the total atom number $N = \int \mathrm{d}^3\vec{x}\,|\Psi|^2$. The atoms are confined in a harmonicpotential $V_{\mathrm{harm}} = \sum_{\xi=x,y,z}\frac{1}{2}m\omega_\xi^2\xi^2$ with single particle mass m and trap frequencies ω_ξ, together with the lattice potential $V_{\mathrm{latt}} = sE_{\mathrm{rec}}\sin^2(kz)$ where s is the tunable lattice depth in multiples of the recoil energy E_{rec} and $k = 2\pi/\lambda$ is the lattice spacing in reciprocal space. The mean-field interaction contributions are $g = 4\pi\hbar^2 a_{\mathrm{s}}/m$ for the contact interaction, governed by the s-wave scattering length a_{s}, and the long-ranged anisotropic dipolar interaction potential $U_{\mathrm{dd}}(\vec{x}) = 3\hbar^2 a_{\mathrm{dd}}/m\left(1-3\cos^2\theta\right)/|\vec{x}|^3$, where $a_{\mathrm{dd}} = \mu_0\mu_m^2 m/12\pi\hbar^2$ with magnetic moment μ_m and θ is the angle between the polarization axis (y-axis) and the vector between neighboring atoms. We also include beyond-mean-field effects through the quantum fluctuations term $\gamma_{\mathrm{QF}} = \frac{32}{3}g\sqrt{\frac{a_{\mathrm{s}}^3}{\pi}}\left(1+\frac{3}{2}\varepsilon_{\mathrm{dd}}^2\right)$ [12], which depends on the relative strength between the dipolar and short-ranged interactions $\varepsilon_{\mathrm{dd}} = a_{\mathrm{dd}}/a_{\mathrm{s}}$. Finally, $F_{\mathrm{ext}} = g_{\mathrm{grav}}m$ denotes the external force exerted on the system by gravity.

In this work, we employ the imaginary time-evolution technique on Eq. (S1) in order to find stationary solutions for the wavefunction in the lattice, without gravity. For various atom numbers and scattering lengths, we use a numerical grid of lengths $(L_x, L_y, L_z) = (6, 33.3, 6)\,\mu$m, with corresponding grid points $128\times256\times128$. The dipolar term is efficiently calculated in momentum space, and we use a cylindrical cut-off in order to negate the effects of aliasing from the Fourier transforms [75].

To derive the effective one-dimensional model, we follow Ref. [45] by assuming a wavefunction decomposition

$$\Psi(\vec{x},t) = \Phi(x,y,l,\eta)\psi(z,t) \equiv \frac{1}{\sqrt{\pi}l}e^{-(\eta x^2+y^2/\eta)/2l^2}\psi(z,t)\,, \tag{S2}$$

with variational parameters l and η representing the width of the radial wavefunction and the anisotropy of the state, respectively. Integrating out the transverse directions (x,y) in Eq. (S1) upon substitution of the ansatz above gives the continuous quasi-one-dimensional eGPE, which when combined with a variational minimization of the energy functional to find (l,η) gives close agreement to the full 3D eGPE [45]. We further decompose the longitudinal wave function $\psi(z,t)$ into a sum of Wannier functions $w(z)$ of the lowest energy band over all lattice sites

$$\psi(z,t) = \sqrt{N}\sum_j c_j(t)\,w(z-z_j)\,, \tag{S3}$$

for complex amplitudes c_j, and positions of lattice minima $z_j = (\lambda/2)j$. For deep enough lattices, the Wannier functions are well approximated by Gaussians of the form $w(z) = \left(\pi l_{\mathrm{latt}}^2\right)^{-1/4}e^{-z^2/2l_{\mathrm{latt}}^2}$, with $l_{\mathrm{latt}} = (k\sqrt[4]{s})^{-1}$. After multiplying on the left by c_j^* and integrating over z, we obtain a set of discrete effective one-dimensional eGPEs

$$i\hbar\frac{\partial c_j}{\partial t} = -J(c_{j+1}+c_{j-1}) + \left(-F_{\mathrm{ext}}z_j + V_{\mathrm{harm}}(z) + g^{1\mathrm{D}}N|c_j|^2 + N\sum_k U^{\mathrm{dd}}_{|j-k|}|c_k|^2 + \gamma^{1\mathrm{D}}_{\mathrm{QF}}N^{3/2}\gamma_{\mathrm{QF}}|c_j|^3\right)c_j\,, \tag{S4}$$

with the reduced effective one-dimensional parameters $\gamma^{1\mathrm{D}}_{\mathrm{QF}} = 2^{3/2}/(5\pi^{3/2}l^2 l_{\mathrm{latt}})^{3/2}\gamma_{\mathrm{QF}}$ and $g^{1\mathrm{D}} = g/((2\pi)^{3/2}l^2 l_{\mathrm{latt}})$. Here, J denotes the tunneling rate between two neighboring lattice sites. The dipolar interaction coefficients between lattice sites j and k depend both on the separation $|j-k|$, and non-trivially on the size l and anisotropy η of the transverse cloud. For the variational minimization, we generate an interpolating function for a sensible range of (l,η) and separations up

to $|j-k|=6$ via

$$U^{\rm dd}_{|j-k|}(l,\eta) = \int \mathrm{d}^3\vec{x}\Big\{|\Psi_0(\vec{x}-z_{|j-k|}\hat{e}_z,l,\eta)|^2 \int \mathrm{d}^3\vec{x}'\, U_{\rm dd}(\vec{x}-\vec{x}')|\Psi_0(\vec{x}',l,\eta)|^2\Big\}, \tag{S5}$$

where $\Psi_0(\vec{x}',l,\eta) = \Phi(x,y,l,\eta)w(z)$ [see Eqs. (S2) and (S3)]. This allows us to simply look up the values of $U^{\rm dd}_{|j-k|}$ without having to recalculate for every time step during the energy minimization. We note that the energy contribution rapidly declines for separations larger than 2 sites, and find that 6 is more than sufficient to quantitatively describe the physics.

To find the stationary state solution of Eq. (S4) (without gravity) we employ an imaginary time-evolution in combination with an optimization scheme, aiming to find the state which minimizes the total energy functional

$$\mathcal{E}[\mathbf{c};l,\eta] = \mathcal{E}_\perp[l,\eta] + \mathcal{E}_\parallel[\mathbf{c};l,\eta]\ , \tag{S6}$$

where $\mathbf{c}=(c_1,c_2,\ldots,c_n)$ for n total lattice sites. Here, $\mathcal{E}_\perp[l,\eta]$ gives the energy contribution from the transverse variational wave function, which reads

$$\mathcal{E}_\perp[l,\eta] = \frac{\hbar^2}{2ml^2}\left(\eta+\frac{1}{\eta}\right) + \frac{ml^2}{4}\left(\frac{\omega_x^2}{\eta}+\eta\omega_y^2\right)\ . \tag{S7}$$

The latter term of Eq. (S6) gives the discrete energy functional for the amplitudes c_j, which includes the tunneling and all interaction terms

$$\mathcal{E}_\parallel[\mathbf{c};l,\eta] = -\sum_j J(c_{j+1}+c_{j-1})c_j + \frac{1}{2}Ng^{\rm 1D}\sum_j|c_j|^4 + \frac{1}{2}N\sum_{j,k}U^{\rm dd}_{|j-k|}|c_k|^2|c_j|^2 + \frac{2}{5}N^{3/2}\gamma^{\rm 1D}_{\rm QF}\sum_j|c_j|^5\,. \tag{S8}$$

Starting from an initial distribution of the amplitudes c_j we first determine the variational parameters $(l,\,\eta)$, which is done via an optimization scheme minimizing Eq. (S8). Subsequently, we evolve the amplitudes in imaginary time using Eq. (S4) and repeat this process until we find the minimum of the total energy function Eq. (S6).

In Fig. S1 we assess the different interaction energy contributions to Eq. (S6) for a range of scattering lengths. For $a_{\rm s} > a_{\rm dd}$ the total interaction energy is positive, and it corresponds to a dilute BEC. Following $a_{\rm s}$ to smaller values all interaction contributions are almost constant, until at around $a_{\rm s} = 60\,a_0$ there is a phase transition from the BEC to droplet state, as identified in Fig. 4 of the main text. This sharp gradient ceases at around $a_{\rm s} = 55\,a_0$, where the atoms are localized to a single lattice plane. Note that although the DDI offsite energy is typically only 10% of the onsite counterpart, it constitutes a significant contribution to the total interaction energy in the system, shifting the BEC to droplet crossover and localization transitions by a few a_0.

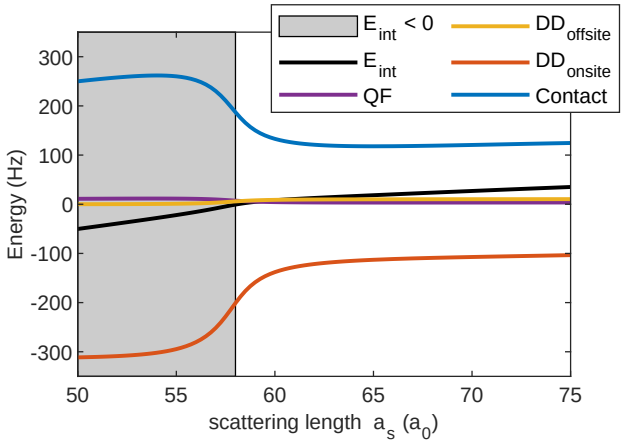

FIG. S1. **Interaction energy contributions.** Scattering length dependency of the individual interaction contributions of the ground state solutions from the 1D model, calculated for $N = 10^4$ atoms.

Once we have the ground state of the system, we employ the discrete effective one-dimensional eGPE in real-time to simulate the Bloch oscillations in the presence of gravity.

2D TO 3D CROSSOVER

The dimensionality of the system is known to highly influence the size and even the sign of the beyond-mean-field contribution, in both Bose-Bose [76–78] and dipolar [56, 79, 80] gases. Here, we assess the validity of employing the full 3D LHY correction to our system. Following Ref. [56], we define the dimensionless parameter $\xi = gn/\epsilon_0$–dependent on the contact interactions g, peak 3D density n, and the confinement energy scale $\epsilon_0 = \hbar^2\pi^2/2mz_{\rm ho}^2$–that indicates which dimensionality regime our system is in. If $\xi \gtrsim 1$ we are safe to use the 3D LHY term, whereas if $\xi \ll 1$ the 2D solution deviates from the 3D one. Deep in the localized droplet regime, where the peak density is on the order of $10^{22}\mathrm{m}^{-3}$, we find $\xi \approx 2$, and the 3D LHY as used throughout this work is valid. Even at large scattering lengths, where the peak density is closer to $5\times10^{20}\mathrm{m}^{-3}$, we find $\xi \approx 0.5$, which introduces an error of less than 5% between the 2D and 3D LHY terms [56]. In this limit, the 2D LHY term may be more appropriate, however in the dilute BEC phase the impact of the LHY is minimal.

ANALYTIC MODEL OF DEPHASING

Starting from the discrete 1D eGPE we decompose the coefficients c_j into amplitude and phase as $c_j =$

$|c_j|\exp(-i\phi_j)$, and then integrate Eq. (S4) in time to give

$$\phi_j(t) = \Bigg(-F_{\rm ext} z_j + g^{\rm 1D} N |c_j|^2 + N \sum_k U^{\rm dd}_{|j-k|} |c_k|^2 + \gamma^{\rm 1D}_{\rm QF} N^{3/2} \gamma_{\rm QF} |c_j|^3 \Bigg) \frac{t}{\hbar} \equiv (-F_{\rm ext} z_j + \mu_j) \frac{t}{\hbar}\,, \tag{S9}$$

with onsite chemical potentials μ_j, and where we have also assumed that $F_{\rm ext} d \gg J$ such that the amplitudes $|c_j|$ are frozen.

Following Ref. [81], we write the Fourier transform of the quasi-1D wavefunction as

$$\psi(k,t) = w(k) \sum_j |c_j| \exp[-i(k z_j + \phi_j(t))] = w(k) \tilde{C}(k,t)\,, \tag{S10}$$

where $w(k)$ is the momentum space Wannier function, and phases ϕ_j are given above. If all interactions are set to zero this function is initially a delta function situated at $k = 0$ and moves in k-space as $\tilde{k} = k - F_{\rm ext} t/\hbar$. Interactions broaden $\tilde{C}(k,t)$, leading to a dephasing of coefficients c_j. Fig. S2(a) depicts $|\tilde{C}(k,t)|^2$ as a function of k at different times t, normalized to $|\tilde{C}(0,0)|^2$.

We extract an analytic approximation to the dephasing time by considering the temporal behaviour of the point $|\tilde{C}(0,t)|^2$, i.e. at $\tilde{k} = 0$. During dephasing this point rapidly decreases through interference between neighboring sites. This quantity is plotted in Fig. S2(b) for a few example scattering lengths. It reaches the threshold $\alpha/\tilde{C}(0,0) = 0.5$ at the dephasing time $t = t_{\rm d}$, where many k-modes are now highly occupied. This time can be found through the smallest positive solution of

$$\alpha = \left| \left(\sum_j |c_j| \cos\left(\frac{\mu_j t_{\rm d}}{\hbar}\right) \right)^2 + \left(\sum_j |c_j| \sin\left(\frac{\mu_j t_{\rm d}}{\hbar}\right) \right)^2 \right|. \tag{S11}$$

Exact solutions to $|\tilde{C}(0,t_{\rm d})|^2 = \alpha$ can be only found in limiting cases. For the three lattice site case, with $j = -1, 0, 1$ and noting the symmetry of $|c_j| = |c_{-j}|$ we obtain

$$t_{\rm d} = \left| \arccos\left(\frac{4|c_0 c_1|}{\alpha + |c_0|^2 - 2} \right) \frac{\hbar}{(\mu_1 - \mu_0)} \right|, \tag{S12}$$

This relation is expected to give an accurate prediction of the dephasing time for all states where only 3 lattice sites are dominant. From this equation, one can see how the dephasing time tends to infinity in the limit of equally distributed chemical potentials, as observed in Fig. 2 of the main text. We can extend this to 5 sites, but it is not as trivial. One needs to numerically solve the transcendental equation

$$\alpha = \Big| 2 - |c_0|^2 + 4|c_0 c_1| \cos\left(\frac{(\mu_0 - \mu_1) t_{\rm d}}{\hbar}\right) + 4|c_0 c_2| \cos\left(\frac{(\mu_0 - \mu_2) t_{\rm d}}{\hbar}\right) + 8|c_1 c_2| \cos\left(\frac{(\mu_1 - \mu_2) t_{\rm d}}{\hbar}\right) \Big|, \tag{S13}$$

for the smallest non-zero root $t_{\rm d}$. We compare the results from Eqs. (S12) and (S13) to the numerically obtained dephasing rate, $\gamma = 1/t_{\rm d}$, in Fig. S2(c), as presented in Fig. 2 of the main text, and find excellent agreement.

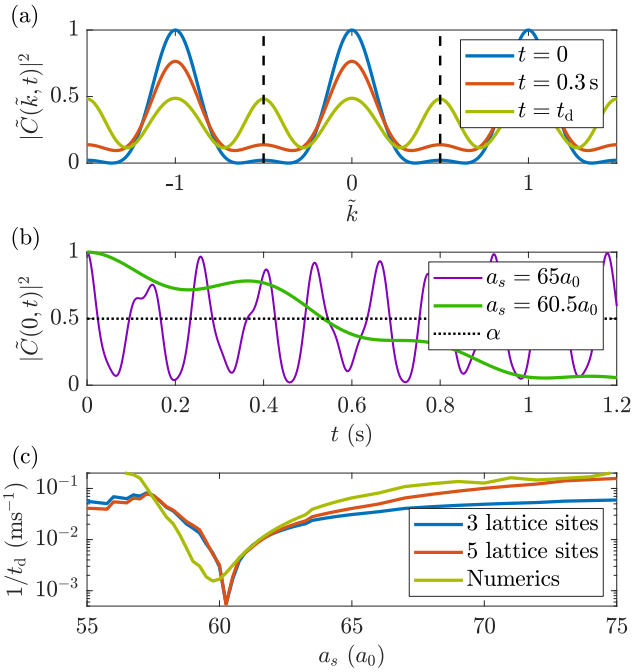

FIG. S2. **Analytic dephasing rate.** **(a)** Evolution of the function $\tilde{C}$, with $\tilde{k}$ normalized to the Brillouin zone in the moving frame, and $a_{\rm s} = 60.5\,a_0$. Here, the solution of Eq. (S12) is $t_{\rm d} = 0.59$s. **(b)** Time evolution of the central point of $\tilde{C}$, showing when $|\tilde{C}|^2$ crosses $\alpha = 0.5$. The function $\tilde{C}$ is scaled to the value at $\tilde{C}(0,0)$. **(c)** Analytic dephasing rate ($\gamma = 1/t_{\rm d}$) obtained for the 3 lattice site approximation Eq. (S12) and the 5 lattice site approximation Eq. (S13), compared to the numerically obtained value from a real-time simulation of the discrete model, Eq. (S4).

EXPERIMENTAL PROTOCOL

We prepare a ^{166}Er spin-polarized BEC similar to Ref. [4]. The magnetic field during the evaporation is along the z-axis with absolute value $|\mathbf{B}| = B_z = 1.9\,\mathrm{G}$ ($a_{\rm s} = 80(1)\,a_0$), see Fig. 1(a). The B-to-as conversion has been precisely mapped out in previous experiments [4, 20]. Before loading the lattice, we rotate the magnetic

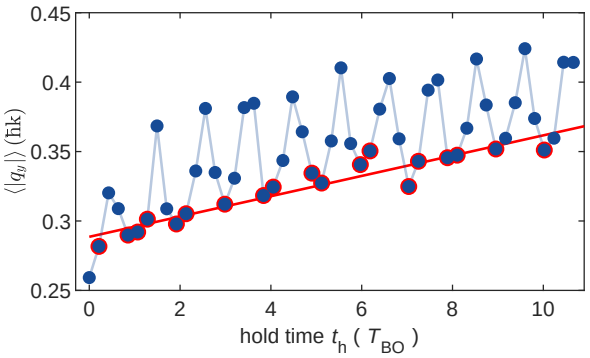

FIG. S3. **Evolution of the $\langle|q_z|\rangle$.** In the figure $\langle|q_z|\rangle$ as a function of time for a_s=58.8 a_0. The points with red edges are the one selected for the fit. The red line corresponds to the fit result $A(t-\tau)+0.5$

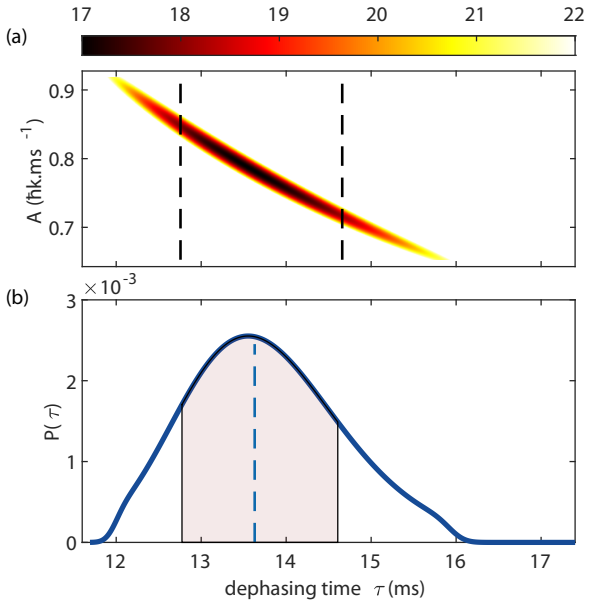

FIG. S4. **Uncertainties χ^2 analysis. (a)** χ^2 as a function of A and τ. The black dash lines correspond to the value $\chi^2_{min}+1$. Below, **(b)** probability distribution of τ, given by numerical integration of $\int_A dA e^{-\chi^2(A,\tau)/2}$ and normalization to 1. a_s=58.8 a_0. The dashed line indicates the fit result and the shaded area the 68% confidence interval.

field direction along the y-axis in 50 ms and change its absolute value to set the scattering length. At this step, we typically achieve 5×10^4 atoms with more than 60 % condensed fraction in a cigar shape dipole trap with trapping frequencies $\omega_{x,y,z} = 2\pi\,(240(3), 30(3), 217(1))$ Hz. For our experiments, the atoms are then loaded in a 1D lattice by a 20 ms exponential ramp of the lattice depth. This is the experimental protocol used in Fig 1, 2, and 3(a).

To study the reversibility of the interaction-induced transition to a single lattice site (3(b)), i.e. the evolution of the contrast due to a change of the scattering length, we employ a different protocol from the one above. In fact, in our experiment, the magnetic field along the y-direction can be changed on a timescale of $\simeq$ 20 ms, which is slower compared to the z-direction ($\simeq$ 1 ms). For this dataset, we prepare the BEC with $\mathbf{B} = (0, 0.25, 1)$ G and then we load the lattice as described above. We then linearly ramp the field in 20 ms to $\mathbf{B} = (0, 0.25, 0)$ G and record the time evolution. In Fig. 3(b), we study the contrast evolution after the ramp. For the black dataset, the magnetic field is quenched back to the initial value after 10 ms.

For Fig 4, we extract the atom number condensed in the lattice by releasing the cloud from the combined ODT-lattice trap and by performing an absorption imaging after 30 ms of TOF. We integrate the density along the lattice axis and use a double Gaussian fit on the integrated density profile. We repeat the sequence 4-8 times for every scattering length. At low scattering lengths, we find a decreased number of condensed atoms, see Fig.4. We attribute this to an increase of three-body loss in the vicinity of a Feshbach resonance [4] and the increased density of the groundstate.

ANALYSIS OF MOMENTUM DISTRIBUTION DURING BLOCH OSCILLATION

When the Bloch oscillation dephases, the width of the momentum distribution increases with time [82]. To evaluate the dephasing rate we analyze the 1D momentum distribution along z, $n(q_z)$, as a function of the holding time. Because of our limited vertical optical access, the 1D lattice is not perfectly aligned with the z (gravity) direction. We measure a tilt of 9(1)°. Such a tilt effectively weakens the radial trapping strength, limiting our observation time to 12 ms, which anyhow allows us to observe up to 25 BO period.

From $n(q_z)$, we can extract the maximum position ($q_z^{\max}$) and the quantity $\langle|q_z|\rangle$, given by

$$\langle|q_z|\rangle = \sum_{q_z} n(q_z)\,|q_z - q_z^{\max}|\,.$$

This quantity is proportional to the width of the distribution. In Fig. S3, we report $\langle|q_z|\rangle$ for a_s= 65.7(1.0) a_0. To quantify the dephasing rate γ, we apply a linear fit to $\langle|q_z|\rangle$. For the fit, we select only the points at the center of the Brillouin zone, up to the time when $\langle|q_z|\rangle$ is reaching the fully dephased configuration, $0.5\hbar k$. Indeed, when the cloud is at the edge of the Brillouin zone, $\langle|q_z|\rangle$ is artificially increased and it does not represent the dephasing, as shown in Fig. S3. We define the dephasing rate γ as the inverse of the time τ that the fitted function needs to

reach the value $0.5\,\hbar k$. Thus, using the fit parametrization $A(t-\tau)+0.5$, where A and τ are the fitting variables and t is the time, we can directly extract τ and its inverse γ.

To determine the uncertainties with our non-linear parametrization, we analyze the $\chi^2(A,\tau)$. We estimate the uncertainties on our data points by assuming equal statistical fluctuations around our fitting model and using the expected value $\langle\chi^2\rangle = N_{\rm data} - 2$. Figure S4 shows a clear asymmetric shape for χ^2, indicating asymmetric uncertainties on our fit parameters. As we are only interested in the uncertainties on τ, we consider $P_{\chi^2}(\tau) = \frac{1}{N}\int_A dA e^{-\chi^2(A,\tau)/2}$, with N a normalization constant. $P_{\chi^2}(\tau)$ corresponds to the probability distribution of τ for our fitting model. Finally, from $P_{\chi^2}(\tau)$, we define the 68% confident interval of our dephasing rate γ shown in Fig. S4.

In order to compare our experimental data with the theoretical predictions, we repeat the same analysis with the data from the 1D discrete model. Since in the experiment the condensed atom number changes with the scattering length, see Fig. 4, the atom number considered in the theoretical simulations varies accordingly. In Fig. 2, we account for the experimental fluctuations by taking an interval of ±20% of the BEC atoms number. For each scattering length, we determine the extreme values of γ in the ±20% range, which we use to create the shaded area.

CONTRAST OF THE INTERFERENCE PATTERN

The density modulation that usually characterizes a BEC loaded into a 1D lattice can be experimentally extracted from the matter-wave interferometry after a TOF expansion [59]. To study the transition to one single occupied lattice site, we record the density distribution as a function of $a_{\rm s}$. In more details, for each picture we perform a Fourier transform (FT) of the integrated momentum distribution, $n(q_z)$. In the contact dominated regime, the lattice induces two sidepeaks at $\pm q_z^*$ in $n(q_z)$. Consequently, in the FT analysis the peaks are at $z^* \simeq \lambda_{\rm lattice}$. The visibility of the interference pattern is then estimated as $n_{\rm FT}(|z^*|)/n_{\rm FT}(0)$.

Chapter 5

New imaging setup for the Erbium experiment

5.1. Motivation and challenges

In 2019, a new state of matter has been observed featuring the density modulation of solid and the phase coherence of a superfluid, called *supersolid* [Cho19] [Tan19] [B̈19]. The density modulations have typically a spacial period of $\lambda^* = 2.5\,\mu m$. To distinguish the modulation maxima and minima it is thus needed to have an imaging with a resolution smaller than λ^*, but typical absorption imaging does not fulfil such a requirement. This is the reason why, in our lab (the ERBIUM experiment), we have rather probed the momentum distribution showing peaks at $k = \frac{2\pi}{\lambda^*}$. In the last two years, supersolid has been subject to intense interest and the importance of in-situ imaging became increasingly large. More recently, theorists predicted the presence of a *domain supersolid* (DSS) in a spin mixture of ^{166}Er with a $m_j = 0$ and $m_j = -6$ [Bla22]. As the domain supersolid is long-lived and the spacial extension is predicted to be of more than $40\,\mu m$ for 3×10^4 atoms, observing it experimentally would allow gaining further understanding of supersolid states in general. Moreover, The ERBIUM experiment has also the ability to use the narrow transition at 1299 nm [Pat21] for state preparation of DSS.

Part of my master project was to build a new imaging setup allowing to reach the target high-resolution of 532 nm. The core of such setup is an objective, customized by the company *Special Optics*, it allows to use all the numerical aperture (NA) given by the current vacuum chamber. Thanks to the 5 beams MOT [Ilz18], the objective can be implemented without tremendous effort.

An objective brings also new optical engineering solutions. The rich spectrum of erbium gives many tools to control the atoms. It is in principle possible to focus a 1299 nm laser beam to locally address atoms confined in a 1064 nm optical lattice.

Combined with a digital micro-mirror device (DMD) this will allow the creation of local perturbations in the spatial plane or the realization of box potentials.

Implementing a new high-resolution imaging system in the erbium experiment presents many opportunities and challenges that will be discussed in this chapter. The first part is devoted to the design and the testing of a high-resolution objective designed to work with a 401 nm imaging light. In the second part, we describe the challenges regarding the implementation in the experiment and the future projects to use the objective.

5.2. Objective design

Let us first briefly review the key formulas and useful notions to understand the basis of the imaging theory. We place ourselves in the framework of diffraction theory and study the optical field after an aperture. This permits to set the definitions of the numerical aperture (NA), the resolution and the point-spread function (PSF). We will discuss briefly aberrations in optical systems and how to characterize them via the Intensity Strehl ratio. Finally, we present the objective designed and produced by the company *Special optics*.

5.2.1. Basics of optical design

Numerical aperture

In general, an object emit light in every direction. Nevertheless, any practical optical system features a finite size can only collect a limited amount of light. The angle over which a system can collect light is quantified by the numerical aperture (NA), defined as,

$$\mathrm{NA} = n \sin(\theta), \tag{5.44}$$

with n the refractive index of the medium and θ the angle of the last incoming beam with the optical axis. The notations are presented in Fig. 5.1. The presence of n assures that the NA is conserved when the light is propagating through different materials. This is an important property since most ultracold experiments present high vacuum setups and the light is travelling through a viewport before being collected by the imaging system. Equivalently, one can introduce the numerical aperture on the image plane and define the magnification M as,

$$\mathrm{NA_o} = |M| \mathrm{NA_i}. \tag{5.45}$$

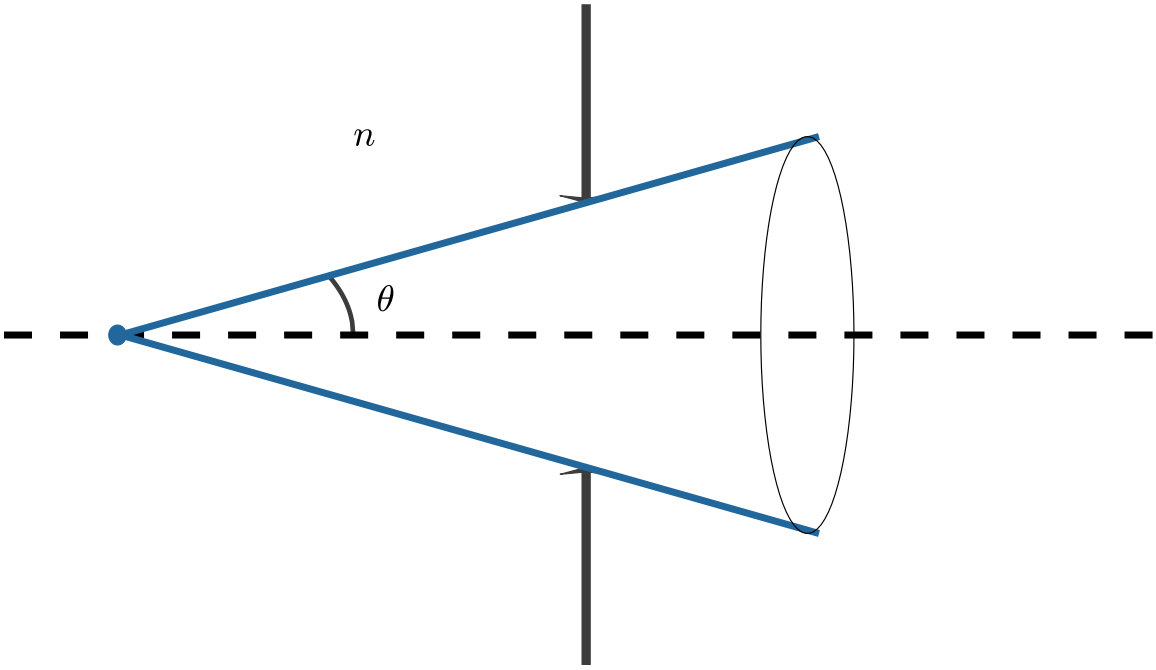

Figure 5.1.: . Light emited by a point source through an aperture. θ is the angle of the last ray with the optical axis and n the refractive index.

In rays optics, the magnification is often considered as the scaling factor between the object and the image.

Diffraction theory

We are now interested in what happens when light travels through an aperture. If one considers light as rays and records the image on a screen, only a shadow with the same shape as the aperture will be observed. However, in practice, depending on the wavelength of the incident light or the size of the aperture, more exotic patterns appear. In the *scalar approximation*, the light field at a position $\mathbf{r}$ is described by a complex field $u(\mathbf{r}) = \sqrt{I(\mathbf{r})}e^{i\phi(\mathbf{r})}$. A plane formed by $\phi(\mathbf{r})$ =const. is called wavefront. The field distribution obeys the scalar wave equation or Helmholtz equation,

$$(\nabla^2 + k^2)u = 0, \tag{5.46}$$

with the wave vector $k = \frac{n2\pi}{\lambda}$, λ the wavelength of the light and n the refractive index of the medium. Equation (5.46) is linear and if u_1 and u_2 are solutions, then u_1+u_2 is also a solution. We will use this property later to calculate the field distribution after an aperture with any shape. In the following, we give a brief review of diffraction theory, based on Ref. [Goo05] and Ref. [Tei07]. The simplest theory of diffraction is based on the assumption that an aperture lets a wave travel through without modification through and reduces it completely outside. An aperture is therefore described by the

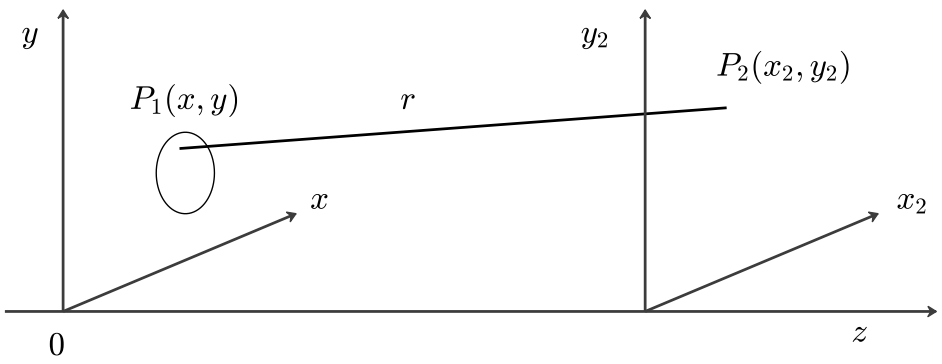

Figure 5.2.: Sketch of the coordinate system. x, y (resp. x_2, y_2) correspond to the diffraction or object plane (resp. the observation or image plane). z is the distance between the two planes and r is the relative distance between P_1 and P_2, the field distributions at (x, y) and (x_2, y_2)

function $A(x, y)$, where,

$$A(x,y) \begin{cases} 1 & \text{inside the aperture} \\ 0 & \text{outside the aperture} \end{cases} \tag{5.47}$$

We consider in the following, $P_1(x, y)$ the incoming complex wave in the aperture and $P_2(x, y)$ the outgoing complex wave at a distance z from the aperture plane. P_1 and P_2 are also called *light field distribution*. The notations are resumed in Fig. 5.2.

According to the Huyghens-Fresnel principle and the linearity of Eq. (5.46), the field $P_2(x, y)$ at a distance z can be calculated by summing over all diverging spherical waves coming from the aperture,

$$P_2(x_2, y_2) = \frac{i}{\lambda} \int\int dxdy P_1(x, y) \frac{\exp(-ikr(x, y))}{r(x, y)}, \tag{5.48}$$

where r is the distance between P_1 and P_2. In the Fraunhofer approximation ($x^2/\lambda, y^2/\lambda << z$), Eq. (5.48) becomes,

$$P_2(x_2, y_2) = \frac{ie^{-ikz}}{z\lambda} \exp(-i\frac{k}{z}\left[x_2^2 + y_2^2\right]) \int\int dxdy P_1(x, y) e^{-i\frac{2k}{z}[x_2 x + y_2 y]} \quad 5.49$$

It is now very easy to calculate the outcoming field as the Fourier transform of the aperture distribution evaluated at the frequencies $f_x = \frac{x}{\lambda z}$ and $f_x = \frac{y}{\lambda z}$.

Lets now consider a particular example of the diffraction intensity pattern from a circular aperture, described by $A(x, y) = circ(x_0, y_0, R)$, the circle of centre (x_0, y_0) with a half diameter R. If we insert P_1 in Eq. (5.49) we obtain,

$$P_2(r) = \frac{i \exp(-ikz)}{z\lambda} \exp(\frac{ikzr^2}{2z}) B[P_1]|_r, \quad 5.50$$

where we used the $r = \sqrt{x_2^2 + y_2^2}$ and the circular symmetry to replace the two-dimensional integral by the Fourier-Bessel transform $B[...]$. The Fourier-Bessel transform of a circular function is given by,

$$B[circ(R)] = A\frac{J_1(2\pi R\rho)}{\pi R\rho}, \quad 5.51$$

where we introduced the reduce variable $\rho = \sqrt{f_x^2 + f_y^2}$ and J_1 represents the first-order Bessel function.

Experimentaly, only the intensity of the diffracted light can be observed. The intensity is defined as the modulus squared of the field and we thus obtain,

$$I(r) = (\frac{1}{\lambda z})^2 A(2\frac{J_1(kRr/z)}{kRr/z})^2. \quad 5.52$$

This intensity pattern is known as the Airy pattern or Airy disk and is schown in Fig. 5.3. The first minimum occurs at,

$$r_0 = 0.61\frac{\lambda z}{R}. \quad 5.53$$

This points out a major difference between ray optics and wave optics. Indeed, an image of an infinitely small point by an aberration-free system is of finite size. As consequence, two points at a distance smaller than r_0 will not be differentiable by common means. This gives the diffraction limit of resolution for an optical system. By approximating $R/z \approx NA$ we can write,

$$r_0 = 0.61\frac{\lambda}{NA}. \quad 5.54$$

We define the diffraction-limited resolution of an optical system as the distance r_0.

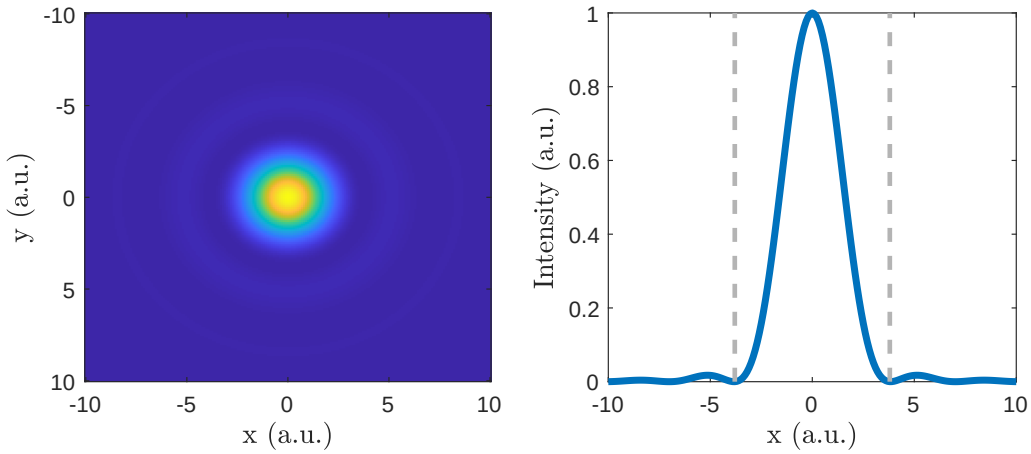

Figure 5.3.: Airy distribution. Left, 2D Airy distribution. Right, cut at $y = 0$ of the Airy distribution. the dashed line correspond to the first minimum

Image formation and point-spread function

Thanks to the linearity of the wave equation, one can use the image of a point source to calculate the light field distribution of a more complex object. Using the supperposition principle we find,

$$P_2(x_2, y_2) = \int\int dxdy\ h(x, y, x_2, y_2) P_1(x, y), \tag{5.55}$$

where $h(x, y, x_2, y_2)$ represents the image at (x_2, y_1) of a point source at (x, y) in the object plane. Using the *isoplanatism* property in the object plane we can write,

$$h(x, y, x_2, y_2) = h(x_2 - x, y_2 - y) \tag{5.56}$$

and reduce Eq. (5.55) to,

$$P_2(x_2, y_2) = \int\int dxdy\ h(x_2 - x, y_2 - y) P_1^g(x, y) = h(x, y) * P_1^g(x, y), \tag{5.57}$$

with $P_1^g(x, y) = P_1(x, y)/\|M\|$ the geometric image of the $P_1(x, y)$ and $*$ stands for the convolution product. One can apply the same procedure to calculate the intensity distribution,

$$I_2(x_2, y_2) = \|h(x, y)\|^2 * I_1^g(x, y). \tag{5.58}$$

The function $\|h(x, y)\|^2$ is referred to as the *point spread function*(PSF) and represents the *impulse response* of an optical system. For an ideal system $\|h(x, y)\|^2$ is an Airy function (Fig. 5.3).

Aberrations and Strehl ratio

In practice no imaging system is perfect and aberrations occur. Aberrations can have many origins, misalignments of optics or surface imperfection of the optical components. They are characterized by the deformation of the wavefront from the reference spherical wave [Mah98]. The most common ones are the five Seidel aberrations [Smi07]: The tilt, the defocus, the coma, the astigmatism and spherical aberrations.

To quantify the aberrations, one method consists in reconstructing the wavefront as a superposition of the Zernike polynomials [Mah13]. This method is very efficient to get an expression of the aberrations as each polynomial can be associated with one type of aberration. Nevertheless, accessing experimentally the wavefront is difficult. It is either asking for many images of PSF at different distances to scan through the focal point of the optical system [Öt19] [Mar17], or using a Shack-Hartmann wavefront sensor like the WFS20-5C/M from *thorlabs* [Kle17]. In the work of this thesis, the size of the beam going out of the objective has a diameter of 60 mm and a standart wavefront sensor could not be used, as it would only probe a very small area of the beam. With the setup employed in the thesis, collecting many PSF at different distance is also imposible.

Another method to quantify aberrations is to calculate the so-called *intensity Strehl ratio* S. In presence of aberrations, the intensity maximum of the Airy peak is reduced since the spot is bigger than the diffraction-limited one. S is then defined as the ratio between the peak intensity between the PSF measured and the peak intensity of the corresponding perfect PSF. This gives a value to S between 0 and 1, where $S = 1$ corresponds to an ideal system. According to the Marechal criterion [Goo05], we considere that an optical system is diffraction-limited if $S > 0.8$.

5.2.2. Design considerations

As seen previously, the resolution of an imaging system depends on the NA and the wavelength λ used. In our experiment, the imaging wavelength λ is 401 nm [Fri14a], which corresponds to a strong transition and allow enough scattering events with atoms. No transition at lower wavelength is available in the optical range for erbium and therefore λ can't be reduced to gain further resolution. One other solution to improve the resolution is to increase the NA. Here we are ultimately limited by the opening angle given by the size of the viewport, which is fixed for the existing vacuum chamber. Due to the relatively large distance of the first possible position of the objective to the object (the atoms themselve), the diameter of the objective has to be large enough to capture the full angle available. Nevertheless, the bigger the objective is, the bigger the aberrations and this necessitates a complex optical design.

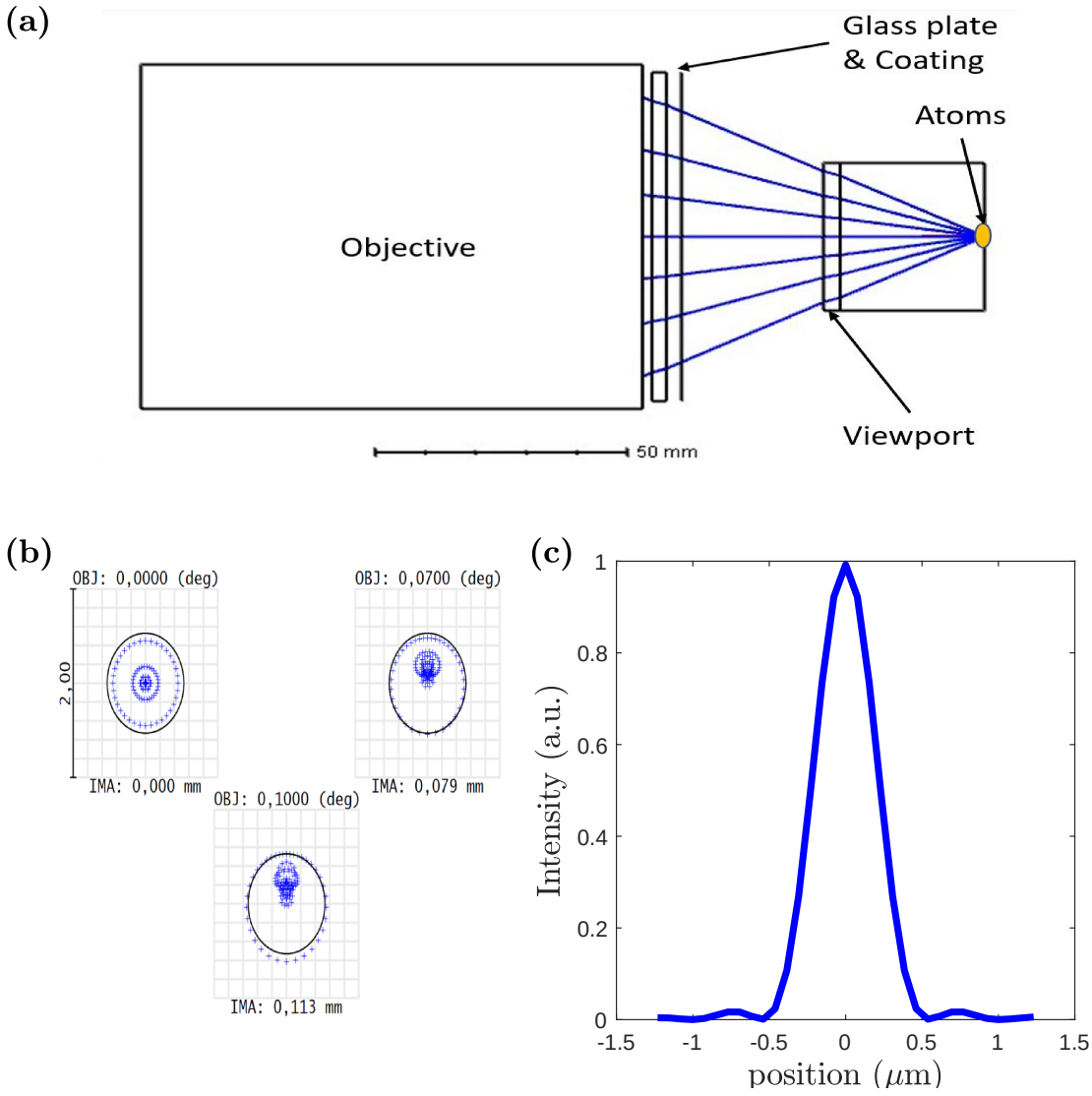

Figure 5.4.: Design of the objective with the software *OpticsStudio*. **(a)** Schematic of the design from the company *Special Optics*.**(b)** Ray spot diagram for a wavelength of 401 nm for different incidence angles. **(c)** Theoretical PSF, featuring a resolution of 532 nm

We finally chose the design proposed by the compagny *Special Optics*, which offers an objective with NA= 0.46, with an effective focal length (EFL) of 60.1 nm and an aperture of 60 mm. This corresponds to a resolution of $Res = 532$ nm. The characteristics of the objective are shown in Fig. 5.4. The design produced includes a compensation for the spherical aberrations introduced by the viewport. The spots diagram in Fig. 5.4(b) shows the sensibility of the objective to angle of the incomming beam.

Additionally, the design from *Special Optics* features an interchangeable front glass plate, allowing to change the reflection coating of the objective according to the purpose of the current project. Extra documents on the objective are presented in Appendix. B.

5.3. Testing the performances of the objective

5.3.1. Test target and Magnification

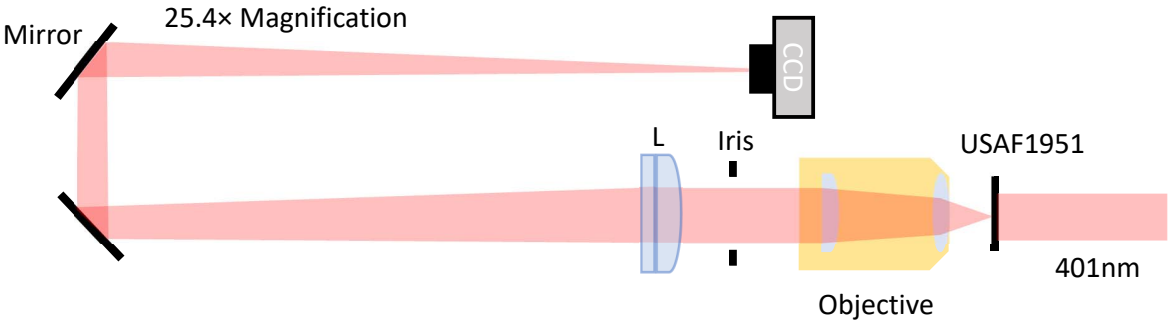

Figure 5.5.: Test target imaging setup. A test target USAG 1952 is illuminated by a collimated beam. The collimated light after the objective is focused by 1524 mm FL Achromatic lens to CCD camera.

Before setting up a new objective in an experiment, we have carried tests of the performance. We experimentally determined the characteristics of the objective and compared them to the specifications sold by the company *Special Optics*.

To get a first measurement on the resolution we try to image the smallest object possible. For that, we use the standard test target USAF 1951 and try to resolve the smallest feature possible. Images of groups 7,8 and 9 are given in Fig. 5.6(a,b). We can resolve easily the bars up to group 8, separated by a distance of 1.1 µm. The group 9 presents a maximum distance of 0.98 µm between the bars. At this scale, aberrations arise and it is not possible to clearly differentiate the bars. This first test indicates that the resolution of the objective is inferior to 1 µm but an exact value cannot be extracted.

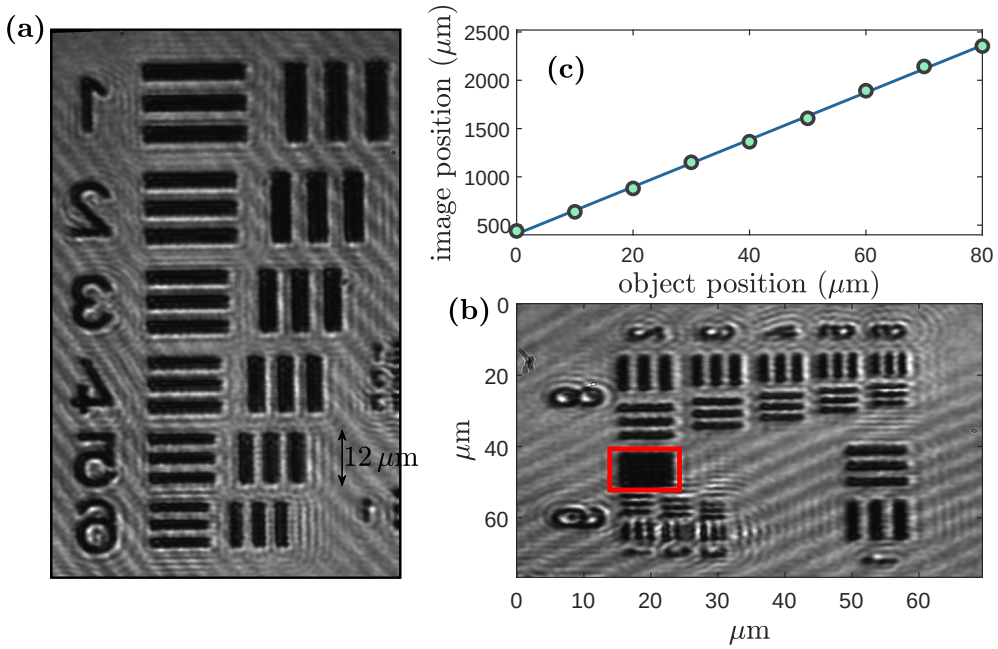

Figure 5.6.: Image of a test target UASF1951. **(a)(b)** group 7-8-9. the red square indicates the object used to determine the magnification **(b)** in green, the position of the square in the image plane versus position in the object plane. In blue, linear fit.

Measure on the test target also permits to determine the magnification of an optical setup. Indeed, we know the size of the camera pixel and the one of a bar and we find $M = \frac{Object}{Image}$. This gives a good approximation of M, but to have a more precise value, one method consists in moving an object of a known distance and recording how much the image has moved. We can directly extract M with the slope of a linear fit. We applied this method with the square in Fig. 5.6(c) and obtained the result in Fig. 5.6(b). We found a magnification of,

$$M = 24.4(3). \tag{5.59}$$

A single pixel of our CCD used has a size of 2.2 µm × 2.2 µm, which corresponds to a region of ≈ 0.09 µm × 0.09 µm on the object.

5.3.2. Determination of the point spread function

Once we know the magnification of the experimental setup, we can try to image the point spread function of the objective. This is not an easy task since we need to create a point source smaller than 532 nm, the resolution of the objective.

The easiest method consists of shining light through a small pinhole [Kle17]. However, for our objective we would need a pinhole with a diameter smaller than 500 nm and

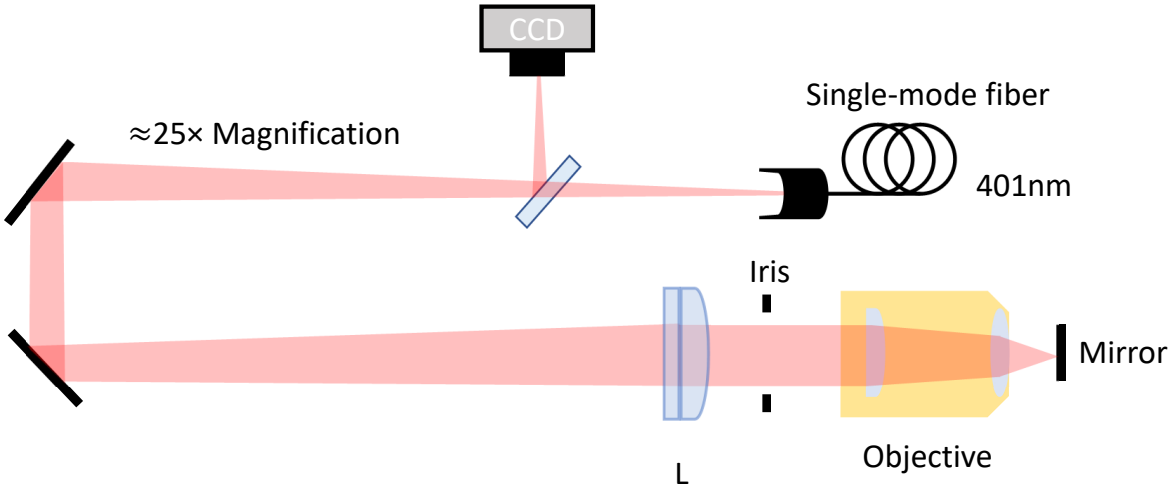

Figure 5.7.: Sketch of the testing setup. A 401 nm light beam is emitted from a single mode fiber with a mode-field diameter of 3.6 µm and expands freely up to a collimation lens (L). The collimated beam is focussed through the objective and reflected back by a mirror. The light is focused by L and sent to a CCD camera recording the PSF

very advanced engineering technics not present at the University of Innsbruck are needed. Other methods can be used like, imaging gold nanoparticles or light emitted from a SNOM fiber [Kle17].

We modified the setup of Fig. 5.5 to the one presented Fig. 5.7. Here, the point source is self-created by the objective, retro-reflected by a mirror and imaged by the objective. More in detail, a 401 nm beam goes out a single-mode fiber with a mode-field-diameter of 3.6 µm and expands for 1524 mm. A 4-inch achromatic lens is used to create a 60 mm collimated beam. The beam diameter can be controlled by an iris. The beam is then, focused by the objective onto a mirror and retro-reflected until a 50:50 plate beam splitter, sending one part of the light to a CCD, where the PSF is imaged.

In this configuration, the objective is probed twice and every aberrations is multiplied by two. Therefore, it is a good way to get an upper bound for the resolution but it is very hard to reach the specifications delivered by *Special Optics*. The point spread function obtained is presented in Fig. 5.8.

5.3.3. Analysis of the point spread function

Once we obtained the PSF, we developed a *Matlab* routine to extract the resolution and the Strehl ratio. We start by recentering with a 2D gaussian the PSF obtained on the CCD (Fig.5.8(a)). As seen with Eq. (5.52), the image of a point source presents a circular symmetry and to reduce the local disturbance we integrate radially the 2D PSF. This is done by summing over all the pixels of (Fig.5.8(a)) and, calculating the

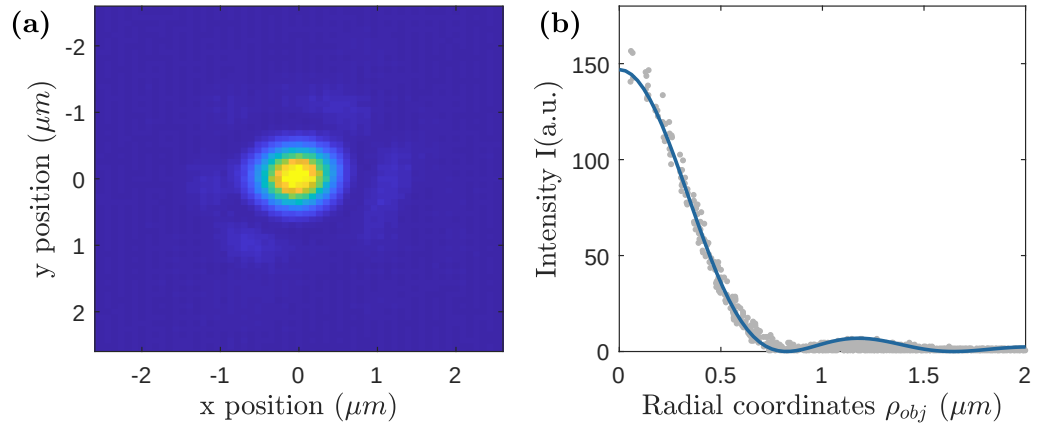

Figure 5.8.: Experimental point spread function of the objective. **(a)** 2D centred PSF. **(b)** In grey, experimental integrated PSF. A fit $\propto sinc^2$ is represented in blue.

distance between the centre of the pixel and the centre of image, ρ_{obj}. We convert the distance from the image plane to the object plane with the magnification M and obtain the radial PSF presented in Fig. 5.8(b).

To determine the resolution of the objective, we extract the first zero crossing by fitting a sinc^2 function to the data in Fig. 5.8(b). The exact mathematical expression of the fit is given by,

$$I_0(\frac{\sin(A\rho)}{A\rho})^2, \tag{5.60}$$

where I_0 and A are the fitting parameters. The result of the fit is represented by the blue line in Fig.5.8(b). The resolution is simply given by Res=$1/A$ and we find,

$$\text{Res} = 0.85(2)\,\mu\text{m}$$

The error corresponds to the uncertainties on the fit parameter A. The resolution is satisfying for future projects and will allow resolving density modulations of a domain supersolid.

Before calculating the Strehl ratio, the data are transferred to bins with a width of 0.05 µm and shown in Fig. 5.9 in blue. This reduces the local fluctuations and the statistical uncertainties on the maximum. To determine the Strehl ratio, one needs to normalize the PSF by the area of the Airy disk (Eq. (5.52)). Mathematically, this is equivalent to write,

$$I_{norm} = C \times I_{PSF}, \tag{5.61}$$

with,

$$C = \frac{\int\int A(x,y)dxdy}{\int\int I_{PSF}dxdy}. \tag{5.62}$$

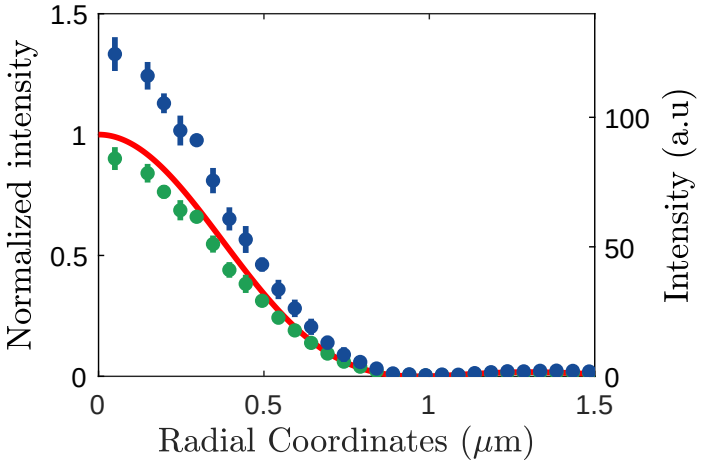

Figure 5.9.: Binarized and normalized PSF. In blue, binarized point spread function with right axis. In green, normalized PSF, left axis and in red perfect PSF. The error bars correspond to the standart deviation over the bins.

$A(x, y)$ is the airy function with a radius set to the experimental resolution. The denominator corresponds to the sum over all the pixels of the local intensity multiplied by the pixel area. We find $C = 5.9(3) \times 10^{-3}$ and dispaly the normalized signal PSF in green in Fig. 5.9.
It is now possible to directly read the Strehl ratio as the peak intensity of I_{norm} and we find,

$$S = 0.88(4). \tag{5.63}$$

The error is evaluated by the propagation of uncertainties with the peak intensity, the calculated resolution and the magnification. S is over 0.8, indicating that in principle the imagining is diffraction limited. Nevertheless, we don't reach the expected resolution, meaning that the full aperture is not used. This can come from a slight defocus of the reflecting mirror and therefore creating a point source bigger than 532 nm. Furthermore, if the aberations are coming from the tilt of the objective, the spherical asymetry of the PSF is reduced during the spherical integration and by consequence will have smaller weight in the calculation of S.

5.3.4. Aperture

As we saw, the resolution of an optical system is directly proportional to the NA, which is proportionnal to the aperture size of the objective. To experimentaly study how the PSF changes with the aperture size, we vary the aperture size with the iris in Fig. 5.7 and analyse the PSF. The results obtained are presented in Fig. 5.10. The theoretical resolution as the function of the iris diameter D can be expressed by

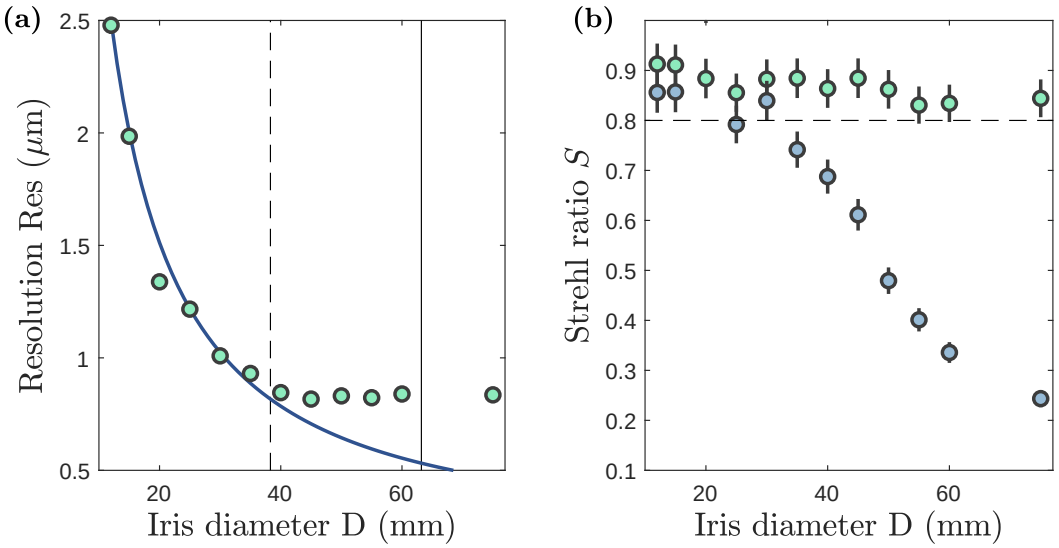

Figure 5.10.: (a) Resolution with the aperture diameter. In green, the data points. The blue line represents the theory calculation based on Eq. (5.54). The dark line represents the aperture limitation due to the mirror size. The dashed line indicates the point where we expect the theory to differe from the experiment due to aberrations. The errorbars are smaller than the symbole size. **(b)** Strehl ratio S versus the aperture. In green, S calculated with the resolution measured and in blue with the theoretical resolution. The dashed line indicates the diffraction limit at $S = 0.8$.

inversing Eq. (5.54) and yields,

$$\mathrm{Res(R)} = \frac{0.61\lambda}{\sin(\mathrm{atan}(\frac{R}{\mathrm{EFL}}))}. \tag{5.64}$$

For small apertures, the experimental data are in good agreement with the theory but from, $D \approx 40\,\mathrm{mm}$ start to deviate. As the maximum resolution obtained is $0.85\,\mu\mathrm{m}$, we expect the resolution to saturate from $D = 38\,\mathrm{mm}$, corresponding to a resolution of $0.85\,\mu\mathrm{m}$ in Eq. (5.64). This is represented by the dashed line in Fig. 5.10(a). The black line corresponds to the limitation of D due to the plastic mount and the size of the objective. We also see that the Strehl ratio S decreases with the size of the aperture. This is caused by an increased sensitivity to aberrations. We calculate S for the measured resolution and theoretical resolution. From $D = 38\,\mathrm{mm}$ the two calculations diverge drastically, indicating that the actual aperture is somehow limited to 38 mm. This can come from the testing setup where the alignment is crucial, and a defocus of less than a μm will cause this deviation.

Another characteristic essential to know is the depth of focus (DOF) as a function of the aperture. Indeed, during TOF, the atomic cloud expands in 3 dimensions and one part will then be out of focus. To the price of losing resolution, by reducing the aperture, it is possible to increase the DOF and image the cloud. The theoretical calculations are presented in Fig. 5.11. Unfortunately, it is impossible with the current

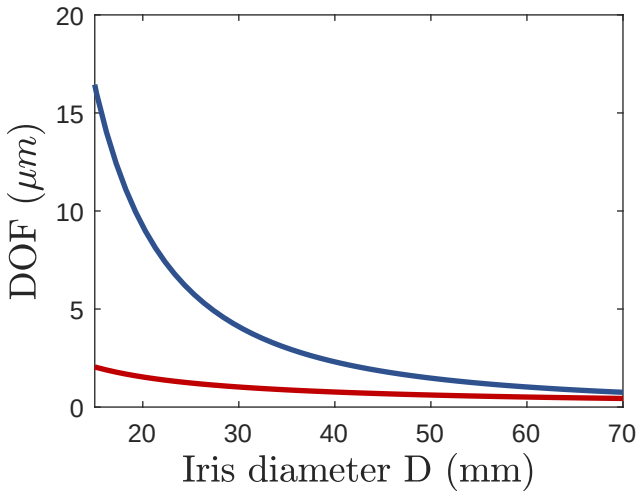

Figure 5.11.: Depth of focus (blue line) and resolution (red) as a function of the iris diameter D.

testing setup to see the influence of a defocus in the resolution and the Strehl ratio.

5.4. Experimental implementation

The last challenge of this thesis was to implement the new objective in the ERBIUM experiment. In the current setup, additionaly to the imaging beam, two laser beams are travelling in the vertical directions, a 401 nm beam for Bragg spectroscopy and 1064 nm for the vertical dipole trap. The new objective would allow to focus a 1299 nm laser beam and use a DMD directly in the image plane. In this section, we present the new design to implement the objective and the plan for the distribution of the laser beams.

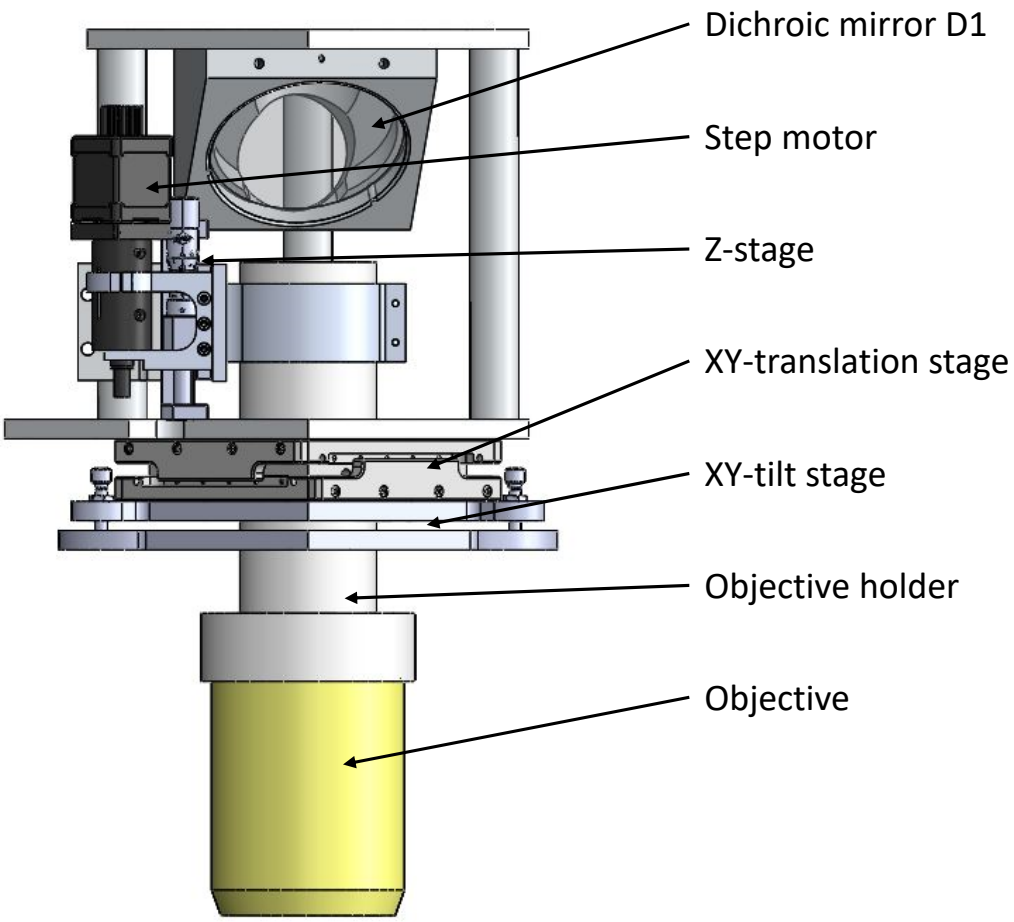

Figure 5.12.: Drawing of the holding tower of the objective realized with *Solidworks 2020*. Design adapted from Maximilian Sohmen thesis [Soh21].

5.4.1. Implementing the imaging setup

High-resolution imaging setups are very sensitive to misalignment on the micrometer scale. The imaging beam pointing on the atoms must be perfectly centred and aligned with the objective and the viewports if one wants to reach the 532 nm resolution specified by the company *Special Optics*.

Our Er-Dy experiment developed a support for the objective which we modify to obtain the one presented in Fig. 5.12. It features all the degrees of freedom needed to align the objective with the atoms. The angle alignment of the imaging beam with the objective is tuned via a self-made XY-tilt stage. An XY-translation stage KT150 from *Owis* is used to centre the beam with the objective. In the current configuration, it offers a travel range of 20 mm. Finally, the height of the objective is controlled by a Z-translation stage MT60 also from *Owis*, featuring a travel range of 50 mm. To be able to change the height of the objective in a controllable way, we have mounted on the Z-translation stage a high-resolution linear actuator M-228 from *Physical Instrument* with a 25 mm range. We found that the M-228 presents a resolution of 1 µm with a speed of $0.1\,\mathrm{mm\,s^{-1}}$ over a 10 mm range (corresponding to the range between in-situ to TOF) but features a bigger error when going back to its inital in-situ position. We, therefore suggest, when going from TOF to in-situ, to go further and come back to the in-situ position. In that way, the error for both, TOF to in-situ and in-situ to TOF is of 1 µm, which is low enough to be used in a reliable way. The objective is screwed on a self-made holder out of fiber-enforced plastics PAS-PEEK-GF30 from *Faigle Gmbh* with a thermal expansion coefficient of 22 µm/(Km). The support also presents a holder for a 100 mm diameter dichroic mirror which can be rotated by $\pm 20°$. A picture of the objective and the holder mounted in the experiment is presented in Fig. 5.15. The breadboards are standard 3/4 of inch breadboards from *thorlabs* that were cut by the University workshop.

5.4.2. Laser distribution for further implementations

This last section is devoted to the future plans for the ERBIUM experiment. As we mentioned in Sec. 5.1, we want to use the objective for different purposes other than imaging. Using lasers with different wavelengths is always a challenge as most of the optical elements are made to work with a small range of wavelengths. Furthermore, one needs elements to split the laser in different paths also called laser distribution.

The two applications we would like to use the objective for are, the creation of light patterns with a DMD setup [Pet15] working with 401 nm and the use of a focused 1299 nm. For further projects, we also want to keep the possibility to use 631 nm and 532 nm in transmission through the objective.

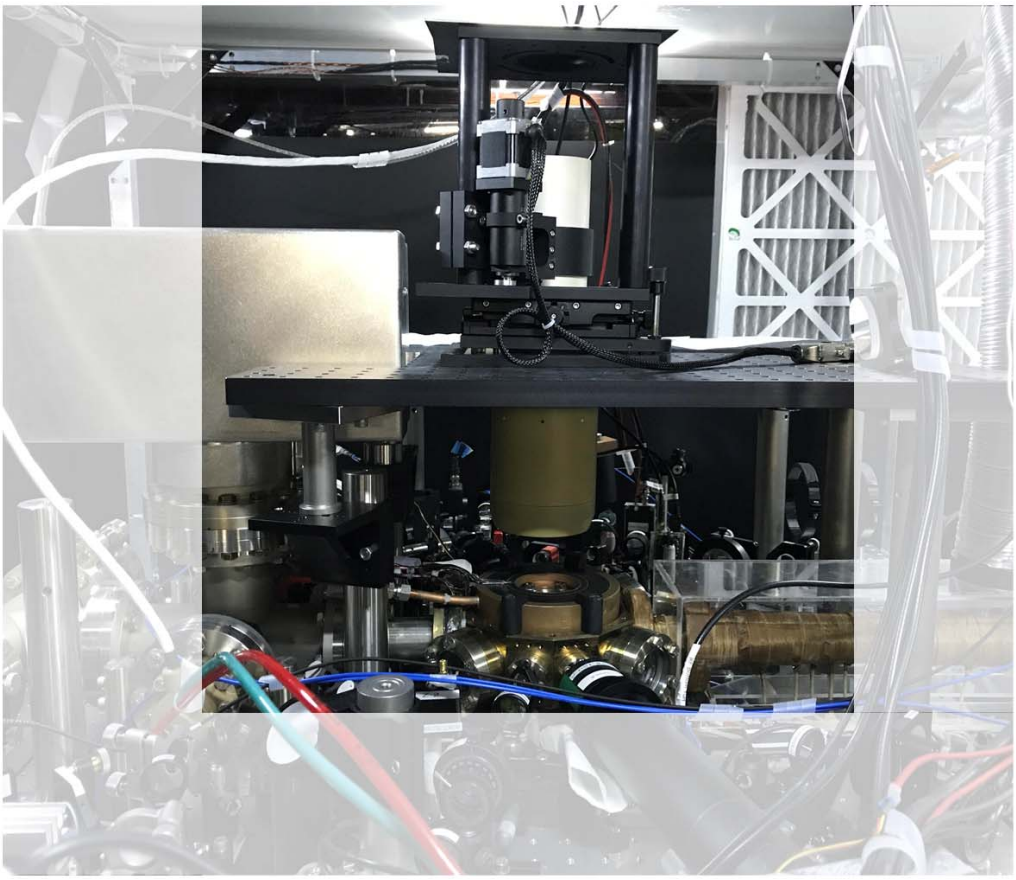

Figure 5.13.: Implementation of the objective in the ERBIUM experiment

To keep as much possible of flexibility, we designed optical paths allowing to use simultaneously light at 401 nm, 1299 nm, 532 nm and eventually 631 nm. The distribution is presented in Fig. 5.14. We decided, to first split the wavelengths 532 nm and 631 nm thanks to a 100 mm dichroic mirror (D1 in Fig. 5.14); see Appendix. B. The light from the imaging is planned to travel through a 50:50 75 mm cube or plate BS and then, be focused by L1 to a CCD camera *Andor Luca*. The 50:50 BS splits the light coming from the DMD to the light of the imaging. Finally, a second dichroic mirror (D2) overlaps the light at 1299 nm with the one at 401 nm.

A first draft of the spatial organisation was made and is presented in Fig. 5.15.

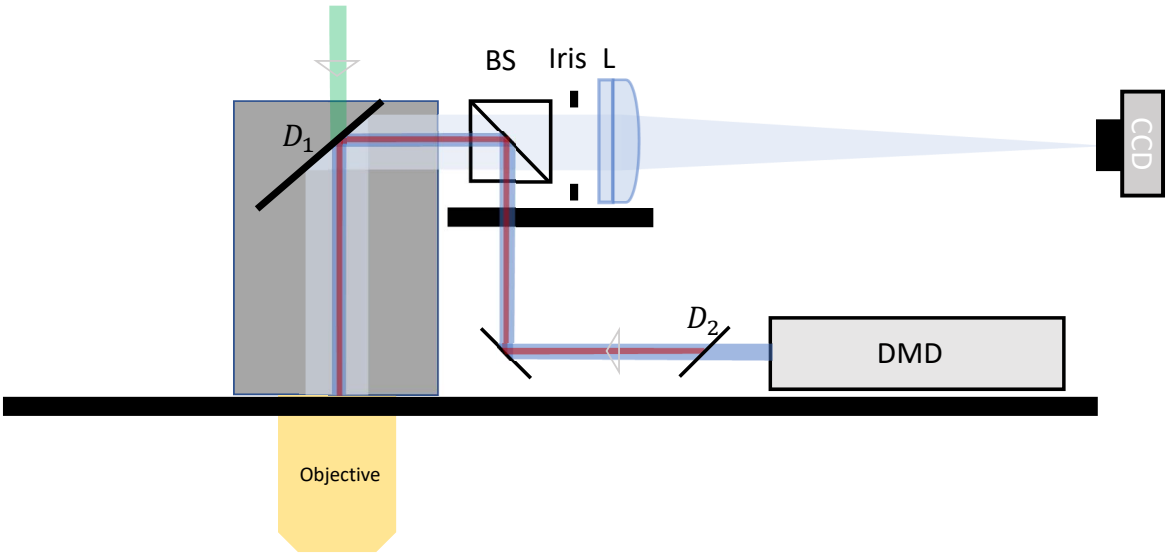

Figure 5.14.: Schematic side view of the implementation of the objective in the experiment. The grey arrows indicate the sens of propagation.

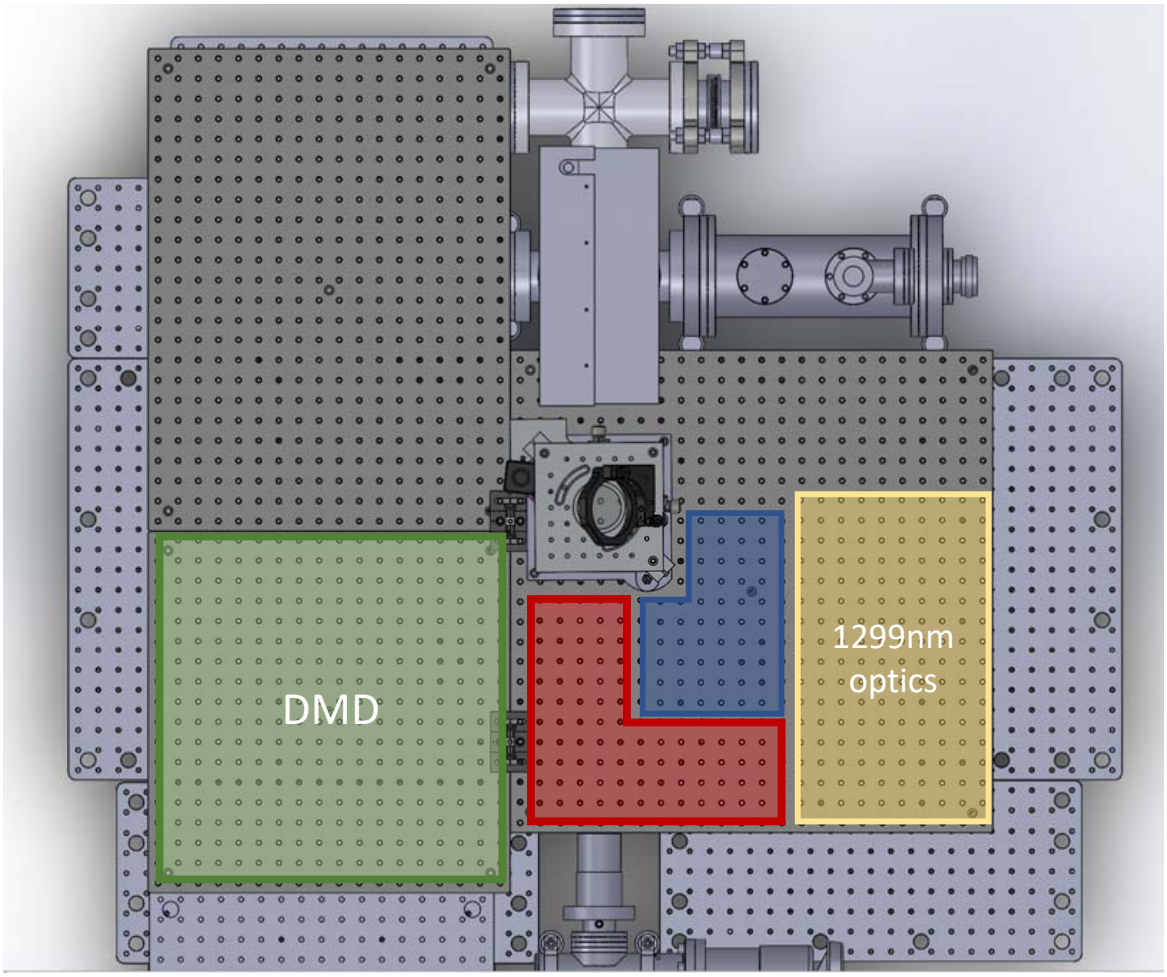

Figure 5.15.: breadboard configuration of the second floor of the ERBIUM experiment. In blue, the space used for the two 401 nm light splitting. In red, the overlapping with the 1299 nm light. In yellow and green are additional spaces for optical implementations.

Chapter 6

Conclusion

6.1. Summary

The first purpose of this thesis was to participate in the experimental study of dipolar gas confined in a 1D optical lattice, creating an array of quasi-2D dipolar gases. We employed Bloch oscillations to understand the role quantum fluctuations play in an array of quasi-two-dimensional BEC. We developed a method to quantify the dephasing rate. We observed long-live oscillations when the repulsive short range interaction and quantum fluctuations balance the attractive long-range dipole-dipole interactions. A minimum of dephasing occurs at $60\,a_0$, corresponding to the minimization of the variance of chemical potential over the lattice sites. By further decreasing the scattering length, we observed the disappearance of the interference pattern in momentum space, a sign of transition to a localized state in a single lattice plane. To quantify the transition region, we performed a Fourier transform to the atomic cloud and defined the contrast as the ratio between the main and second order components. The observations were compared with a discrete quasi-one-dimensional theoretical model developed in our group. Based on the extended Gross-Pitaevskii theory, it shows a great quantitative agreement.

The second purpose of this thesis was to design, characterize and implement an high-resolution imaging setup, allowing to reach in-situ density distribution of dipolar BEC of erbium directly in the trap. We imaged the point-spread function of an objective designed and produced by *Special Optics*. We found a resolution of $0.85(2)\,\mu m$, with an intensity Strehl ratio of $S = 0.88(4)$. This is sufficient for the purpose of the experiment and would allow us to observe in-situ supersolid density modulation. To align the objective with the atoms, we designed a support for the objective including 5 precision adjustable degrees of freedom, the XY-tilt, the XY-translation and Z-translation. The Z-translation can be controlled by a stepper motor to change from TOF to in-situ imaging reliably. Finally, we draw a first planing for the future laser implementations of the ERBIUM experiment. This new imaging setup represents a

major step for the actual experiment toward quantum simulation and offers many new opportunities to observe exotic states of matter with dipolar erbium.

6.2. Further understanding of dipolar BEC in optical lattices

Our study on Bloch oscillations opened the door to a deeper questioning. As already emphasized in Ref. [Kum19], dipolar gases in optical lattices represent a unique opportunity to control and experimentally access the effects of quantum fluctuation. In our experiment we probed BO for a lattice depth of 8 E_{rec}. In order to understand better the role played by LHY in distributing the chemical potential over the lattice sites without suffering from atom loss, it would be interesting to find a way to shift the minimum of dephasing to higher a_{s}.

We investigated only dipoles aligned along the elongated axes, with principaly mean-field attractive interactions. Early results for B aligned along the gravity axis indicated that the behaviour is different. In this configuration DDI, is repulsive and only few Bloch cycles were observed and further studies are needed.

6.3. Next step for the implementation of the objective

The objective has been set up recently in the experiment, but to reach a sub-micron resolution, alignment between the atoms, the viewport and the objective must be perfect. So far, we aligned the imaging beam perpendicular to the viewport, giving us a reference to align the objective. The next step will include the setting of the imaging optical path and the camera *Andor Luka*. Once done, we will perform the last fine adjustment of the objective by trying to resolve the density modulation of a supersolid.

Appendix A

Code analyse PSF

A.1. main.m

```
1
2  %% parameters
3  ROI_cut=50;
4  pixel_camera=2.2; %in microns
5  magnification=24.4;
6  error_magnification=0.4;
7  res_coeff=pixel_camera/magnification; %rescaling coefficient
8  err_res_coeff= pixel_camera*error_magnification/magnification
       ^2;
9  pix_area=res_coeff*res_coeff;
10 err_pix_area=res_coeff*2*err_res_coeff;
11
12 %% analysis
13 %load the pictures
14 filename=['%%filename%%','mm.bmp'];
15
16 psf=imread(filename);
17
18
19 ROI=create_ROI(psf, ROI_cut, 1);
20 %1D integration of the psf
21 [rho, psf_int]= PSF_1D(ROI, ROI_cut , 1);
22 %calculation of the resolution
23 [res, err_res, I0, err_I0]= resolution(rho, psf_int,res_coeff,
       err_res_coeff, 1);
24 %extraction of the normalisation coefficient
25 [C_res,err_C_res]=norma(ROI,res, err_res,pix_area,
       err_pix_area);
```

```
26
27 %calculation of strehl ratio
28 strehl= C_res*I0;
29 err_strehl=strehl(inda)*sqrt((err_C_res/C_res)^2+(err_I0/I0)
       ^2);
```

A.2. create_ROI.m

```
1  function [ROI]= create_ROI(data, ROI_cut, show_p)
2  %% create a ROI out of a 2D psf function
3  % showp =1 to show a plot
4
5
6  %find the center
7  [maxv,maxpx]=max(data);
8  [maxvv,maxpy]=max(maxv);
9  maxpx=maxpx(maxpy);
10
11 %Cut the ROI and center
12 ROI=double(data(maxpx-ROI_cut:maxpx+ROI_cut,maxpy-ROI_cut:
       maxpy+ROI_cut));
13 %remove the background
14 ROI=ROI-mean(mean(data(1:30,1:30)));
15
16 if show_p==1
17      figure(10)
18      imagesc(ROI)
19
20 end
```

A.3. PSF_1D.m

```
1  function [rho, c_fit] = PSF_1D(ROI,ROI_cut, show_p)
2
3  % return the circulary integrated PSF
4  % ROI -> 2D array
5  % Magn -> magnification coefficient
6  % px_size of the camera
7  % show_p -> show the plots
8
9  % the analysis is based on a circular integration of the PSF
       and fitting
```

```
10 % with a sinc^2
11
12
13 [s1,s2]=size(ROI);
14 x_fit=zeros(1,s1*s2);
15 y_fit=zeros(1,s1*s2);
16 c_fit=zeros(1,s1*s2);
17 for ind1=1:s1
18     for ind2=1:s2
19         x_fit((ind1-1)*s1+ind2)=-ROI_cut+ind1-1;
20         y_fit((ind1-1)*s1+ind2)=-ROI_cut+ind2-1;
21         c_fit((ind1-1)*s1+ind2)=ROI(ind1,ind2);
22     end
23 end
24
25
26 %fit a gaussian to get the center position
27 maxv=max(c_fit);
28 myfitgau=fittype('I*exp(-2*(x-A).^2/B^2)*exp(-2*(t-C).^2/D^2)'
       , 'indep',{'x','t'},'coef',{'A','B','C','D','I'});
29 [mdl1,gof1]=fit([x_fit',y_fit'],c_fit',myfitgau,'start'
       ,[0,3,0,3,maxv]);
30
31 %recenter the psf
32 center_x=mdl1.A;
33 center_y=mdl1.C;
34
35 %circular numerical integration
36 rho=zeros(1,length(c_fit));
37 for ind1=1:length(c_fit)
38    rho(ind1)=sqrt((x_fit(ind1)-center_x)^2+(y_fit(ind1)-
          center_y)^2);
39 end
40
41
42 if show_p==1
43     figure(1)
44     imagesc(ROI)
45
46     figure(2)
47     hold on;
48     plot(rho,c_fit,'o','Markersize',1)
49 end
```

A.4. resolution.m

```
function [res, err_res, I0, err_I0]= resolution(rho, psf_1D,
    res_coeff,err_res_coeff, show_p)
%calculate the resolution with a sinc^2 fit
% rho -> X_axis of the psf in pixel
% 1D_ROI= 1D_integrated psf, 1D array
% px_size -> size of the pixel of camera
% magn -> magnification of the optical system
% err_magn -> error on the magnefication
% show_p=1 to see plots


maxv=max(psf_1D);
%calculate the resolution with a sinc^2 fit

myfit=fittype('I*sinc(A*x)^2', 'indep',{'x'},'coef',{'A','I'})
    ;
fit_poly=fittype('A+(x-B)^3+C*x^2', 'indep',{'x'},'coef',{'A',
    'B','C'});
fitfunc=@(I,A,x) I*sinc(A*x).^2;
[mdl,gof]=fit(rho', psf_1D', myfit,'start',[0.1,maxv]);
[mdl_poly,gof]=fit(rho', psf_1D', fit_poly, 'start',[maxv
    ,0,1],'lower',[0,0,-1000]);
res=1/mdl.A*res_coeff; %resoltuion in um

%resolution=0.627;

%calcul error on the resolution calculation
alpha = 0.68;
ci = confint(mdl, alpha);
err_A=(ci(2)-ci(1))/2;
err_I=(ci(end)-ci(end-1))/2;

%give the error on the resolution
err_res=res*sqrt((err_A/mdl.A)^2+(err_res_coeff/res_coeff)^2);
I0=mdl.I;
err_I0=err_I;
if show_p==1
     x_plot=linspace(0,30,1000);
     figure(20);
     hold on;
     plot(rho*res_coeff,psf_1D,'o','Markersize',1);
     plot(x_plot*res_coeff,mdl(x_plot));
```

```
39      xlabel('distance to center (\mu m)');
40      ylabel('intensity (a.u)');
41      xlim([0,2]);
42  end
43  %plot(x_plot*0.1,mdl_poly(x_plot));
```

A.5. norma.m

```
1  function [C_2D, err_C_2D]= norma(psf_2D, res, err_res,
       pix_area, err_pix_area)
2  % renormalize the wave function
3  % return the renormalization coefficient and the error
       associated to it
4
5  %psf_2D -> 2D arrax of the psf
6  %res -> resolution of the objective
7  %err_res -> error of the resolution
8  %pix_area equivalent objet of the area of one pixel
9  %err_pix_area error of the pixel area
10
11 %% experimental determination of the integral
12 int_2d=sum(sum(psf_2D))*pix_area;
13 err_int_2d= sum(sum(psf_2D))*err_pix_area;
14
15
16 %% 2D perfect bessel function
17 X=[];Y=[];
18
19 x = -10:0.2:10;
20 y = -10:0.2:10;
21 %scaling of x,y
22 rescal=res/3.8317;  %rescaling factor
23 rescal_max=(res+err_res)/3.8317;  %rescaling factor
24 X=meshgrid(x);
25 Y=meshgrid(y)';
26 Rho=sqrt(X.^2+Y.^2);
27 I0 = 1;
28 I = I0*(2*besselj(1,Rho)./(Rho)).^2;
29 I(isnan(I))=1;
30 figure(1)
31 X=rescal*X;
32 Y=rescal*Y;
33 surface(X,Y,I,'Edgecolor','none')
```

```
34
35 theory_pix_area=(0.2*rescal)^2;
36 theory_pix_area_max=(0.2*rescal_max)^2;
37
38 %integral of I
39 int_2D_theory=sum(sum(I))*theory_pix_area;
40 int_2D_theory_max=sum(sum(I))*theory_pix_area_max; %upper
      bound for the integration of the airy pattern.
41 err_int_2D_theory=int_2D_theory_max-int_2D_theory;
42
43
44 C_2D=int_2D_theory/int_2d;
45 err_C_2D=C_2D*sqrt((err_int_2D_theory/int_2D_theory)^2+(
      err_int_2d/int_2d)^2);
46 %ylabel('Normalized PSF Amplitude')
47 %xlabel('Radial Coordinates')
```

Appendix

B

Technical documents of imaging setup

This chapter presents additionnal documents related to the new imaging setup.

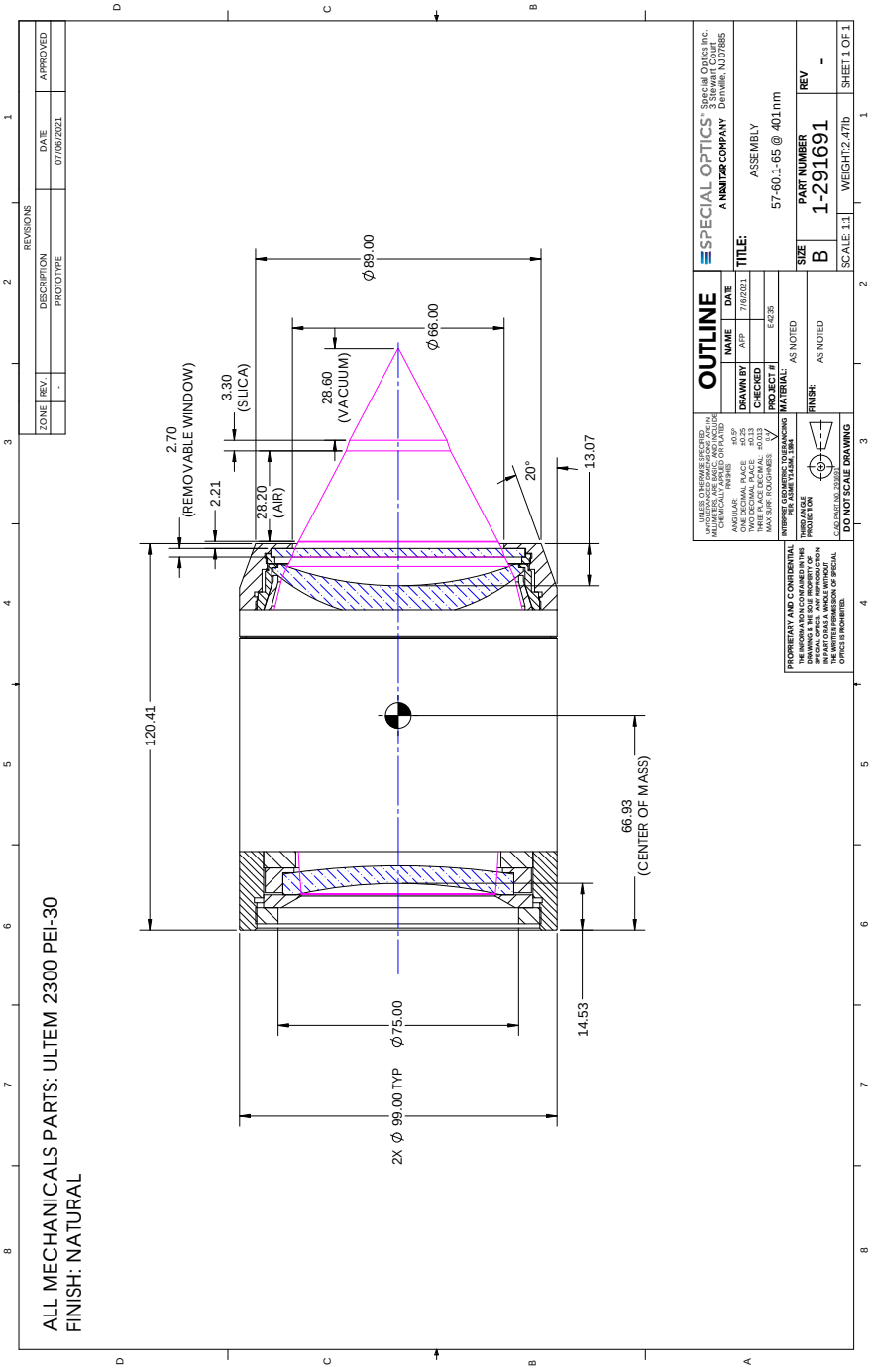

Figure B.1.: Technical drawing of the objective produced by *SpecialOptics*

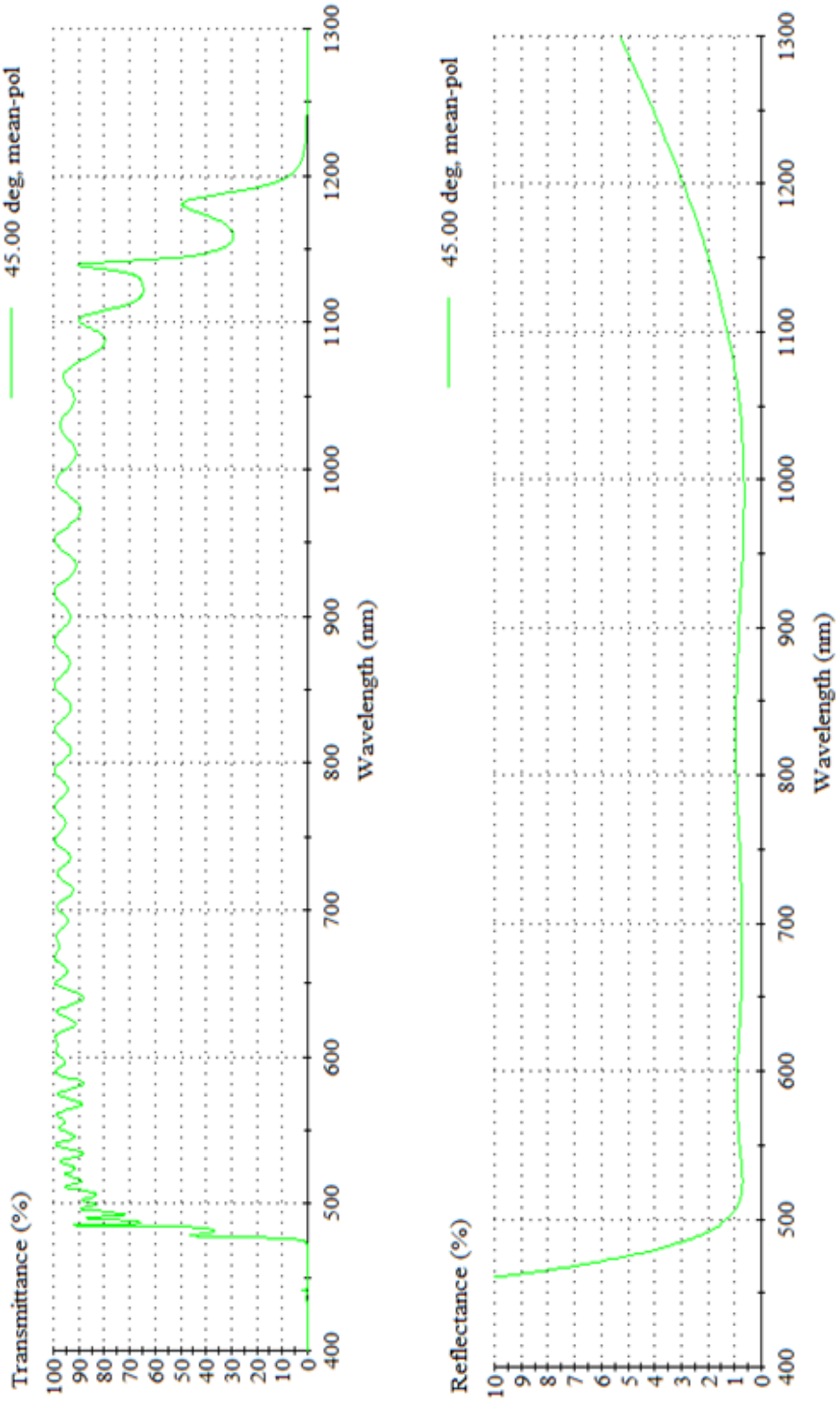

Figure B.2.: , Coating of the dichroic mirror D1 produced by *OptoSigma*

Bibliography

[Aik12] K. Aikawa, A. Frisch, M. Mark, S. Baier, A. Rietzler, et al., *Bose-Einstein Condensation of Erbium*, Phys. Rev. Lett. **108**, 210401 (2012).

[Aik14] K. Aikawa, A. Frisch, M. Mark, S. Baier, R. Grimm, et al., *Reaching Fermi Degeneracy via Universal Dipolar Scattering*, Phys. Rev. Lett. **112**, 010404 (2014).

[And95] M. H. Anderson, J. R. Ensher, M. R. Matthews, C. E. Wieman, and E. A. Cornell, *Observation of Bose-Einstein Condensation in a Dilute Atomic Vapor*, Science **269**, 198–201 (1995).

[And97] M. R. Andrews, C. Townsend, H. J. Miesner, D. Durfee, D. M. Kurn, et al., *Observation of Interference Between Two Bose Condensates*, Science **275**, 637 – 641 (1997).

[Asc76] N. W. Aschroft and N. D. Mermin, *Solid State Physics*, Saunders College Publishing, New York, 1976.

[BÏ9] F. Böttcher, J.-N. Schmidt, M. Wenzel, J. Hertkorn, M. Guo, et al., *Transient Supersolid Properties in an Array of Dipolar Quantum Droplets*, Phys. Rev. X **9**, 011051 (2019).

[Bai16] S. Baier, M. J. Mark, D. Petter, K. Aikawa, L. Chomaz, et al., *Extended Bose-Hubbard models with ultracold magnetic atoms*, Science **352**, 201–205 (2016).

[Bak09] W. S. Bakr, J. I. Gillen, A. Peng, S. Fölling, and M. Greiner, *A quantum gas microscope for detecting single atoms in a Hubbard-regime optical lattice*, Nature **462**, 74–77 (2009).

[Bar08] M. Baranov, *Theoretical progress in many-body physics with ultracold dipolar gases*, Physics Reports **464**, 71–111 (2008).

[Bar12] M. A. Baranov, M. Dalmonte, G. Pupillo, and P. Zoller, *Condensed Matter Theory of Dipolar Quantum Gases*, Chemical Reviews **112**, 5012–5061 (2012).

[BD96] M. Ben Dahan, E. Peik, J. Reichel, Y. Castin, and C. Salomon, *Bloch Oscillations of Atoms in an Optical Potential*, Phys. Rev. Lett. **76**, 4508–4511 (1996).

[Bec99] P. Becker, N. Olsson, and J. Simpson, *Chapter 5 - Erbium-Doped Fiber Amplifiers—Amplifier Basics*, Erbium-Doped Fiber Amplifiers (P. Becker, N. Olsson, and J. Simpson, eds.), Optics and Photonics, Academic Press, San Diego, 1999, pp. 131–152.

[Bec18] J. H. Becher, S. Baier, K. Aikawa, M. Lepers, J.-F. Wyart, et al., *Anisotropic polarizability of erbium atoms*, Phys. Rev. A **97**, 012509 (2018).

[Bla20] P. B. Blakie, D. Baillie, and S. Pal, *Variational theory for the ground state and collective excitations of an elongated dipolar condensate*, Communications in Theoretical Physics **72**, 085501 (2020).

[Bla22] T. Bland, E. Poli, L. A. P. na Ardila, L. Santos, F. Ferlaino, et al., *Domain supersolids in binary dipolar condensates*, arXiv:2203.11119 2203.11119 (2022).

[Blo29] F. Bloch, *Über die Quantenmechanik der Elektronen in Kristallgittern*, Zeitschrift für Physik **52**, 555–600 (1929).

[Blo05] I. Bloch, *Ultracold quantum gases in optical lattices*, Nature Physics **1**, 23–30 (2005).

[Blo12] I. Bloch, J. Dalibard, and S. Nascimbène, *Quantum simulations with ultracold quantum gases*, Nature Physics **8**, 267–276 (2012).

[Bra95] C. C. Bradley, C. A. Sackett, J. J. Tollett, and R. G. Hulet, *Evidence of Bose-Einstein Condensation in an Atomic Gas with Attractive Interactions*, Phys. Rev. Lett. **75**, 1687–1690 (1995).

[Car05] I. Carusotto, L. Pitaevskii, S. Stringari, G. Modugno, and M. Inguscio, *Sensitive Measurement of Forces at the Micron Scale Using Bloch Oscillations of Ultracold Atoms*, Phys. Rev. Lett. **95**, 093202 (2005).

[Chi10] C. Chin, R. Grimm, P. Julienne, and E. Tiesinga, *Feshbach resonances in ultracold gases*, Rev. Mod. Phys. **82**, 1225–1286 (2010).

[Cho16] L. Chomaz, S. Baier, D. Petter, M. J. Mark, F. Wächtler, et al., *Quantum-Fluctuation-Driven Crossover from a Dilute Bose-Einstein Condensate to a Macrodroplet in a Dipolar Quantum Fluid*, Phys. Rev. X **6**, 041039 (2016).

[Cho19] L. Chomaz, D. Petter, P. Ilzhöfer, G. Natale, A. Trautmann, et al., *Long-Lived and Transient Supersolid Behaviors in Dipolar Quantum Gases*, Phys. Rev. X **9**, 021012 (2019).

[Cho22] L. Chomaz, I. Ferrier-Barbut, F. Ferlaino, B. Laburthe-Tolra, B. L. Lev, et al., *Dipolar physics: A review of experiments with magnetic quantum gases* (2022).

[Con63] J. G. Conway and B. G. Wybourne, *Low-Lying Energy Levels of Lanthanide Atoms and Intermediate Coupling*, Phys. Rev. **130**, 2325–2332 (1963).

[Dav95] K. B. Davis, M. O. Mewes, M. R. Andrews, N. J. van Druten, D. S. Durfee, et al., *Bose-Einstein Condensation in a Gas of Sodium Atoms*, Phys. Rev. Lett. **75**, 3969–3973 (1995).

[dB25] L. de Broglie, *Recherches sur la théorie des Quanta*, Annales de la fondation Louis de Broglie (1925).

[Fat08] M. Fattori, G. Roati, B. Deissler, C. D'Errico, M. Zaccanti, et al., *Magnetic Dipolar Interaction in a Bose-Einstein Condensate Atomic Interferometer*, Phys. Rev. Lett. **101**, 190405 (2008).

[Fer06] G. Ferrari, N. Poli, F. Sorrentino, and G. M. Tino, *Long-Lived Bloch Oscillations with Bosonic Sr Atoms and Application to Gravity Measurement at the Micrometer Scale*, Phys. Rev. Lett. **97**, 060402 (2006).

[Fey82] R. P. Feynman, *Simulating physics with computers*, International Journal of Theoretical Physics **21**, 467–488 (1982).

[Fri12] A. Frisch, K. Aikawa, M. Mark, A. Rietzler, J. Schindler, et al., *Narrow-line magneto-optical trap for erbium*, Phys. Rev. A **85**, 051401(R) (2012).

[Fri14a] A. Frisch, *Dipolar Quantum Gases of Erbium*, PhD Thesis (2014).

[Fri14b] A. Frisch, M. Mark, K. Aikawa, F. Ferlaino, J. L. Bohn, et al., *Quantum chaos in ultracold collisions of gas-phase erbium atoms*, Nature **507**, 475–479 (2014).

[Gad09] B. Gadway, D. Pertot, R. Reimann, M. G. Cohen, and D. Schneble, *Analysis of Kapitza-Dirac diffraction patterns beyond the Raman-Nath regime*, Opt. Express **17**, 19173–19180 (2009).

[Goo05] J. Goodman, *Introduction to Fourier Optics*, McGraw-Hill physical and quantum electronics series, W. H. Freeman, 2005.

[Gre02] M. Greiner, O. Mandel, T. Esslinger, T. W. Hänsch, and I. Bloch, *Quantum phase transition from a superfluid to a Mott insulator in a gas of ultracold atoms*, Nature **415**, 39–44 (2002).

[Gri00] R. Grimm, M. Weidemüller, and Y. B. Ovchinnikov, *Optical Dipole Traps for Neutral Atoms*, 95–170 (2000).

[Gup05] C. Gupta and N. Krishnamurthy, *Extractive metallurgy of rare earths*, CRC Press, 2005.

[Gus08] M. Gustavsson, E. Haller, M. J. Mark, J. G. Danzl, G. Rojas-Kopeinig, et al., *Control of Interaction-Induced Dephasing of Bloch Oscillations*, Phys. Rev. Lett. **100**, 080404 (2008).

[Hem93] A. Hemmerich and T. Hänsch, *Two and three-dimensional optical crystals*, Fundamentals of Quantum Optics III (Berlin, Heidelberg) (F. Ehlotzky, ed.), Springer Berlin Heidelberg, 1993, pp. 90–104.

[Hub63] J. Hubbard, *Electron correlations in narrow energy bands*, Proceedings of the Royal Society of London A: Mathematical, Physical and Engineering Sciences **276**, 238–257 (1963).

[Ifa10] G. H. Ifan and P. H. Thomas, *Measurement and their Uncertainties*, OUP, 2010.

[Ilz18] P. Ilzhöfer, G. Durastante, A. Patscheider, A. Trautmann, M. J. Mark, et al., *Two-species five-beam magneto-optical trap for erbium and dysprosium*, Phys. Rev. A **97**, 023633 (2018).

[Jak98] D. Jaksch, C. Bruder, J. I. Cirac, C. W. Gardiner, and P. Zoller, *Cold Bosonic Atoms in Optical Lattices*, Phys. Rev. Lett. **81**, 3108–3111 (1998).

[Ket96] W. Ketterle and N. V. Druten, *Evaporative Cooling of Trapped Atoms*, Advances In Atomic, Molecular, and Optical Physics, vol. 37, Academic Press, 1996, pp. 181–236.

[Kit05] C. Kittel, *Introduction to Solid State Physics*, Wiley, New York, 2005.

[Kle17] F. Kleissler, *Assembly and Characterization of a High Numerical Aperture Microscope for Single Atoms*, Master's thesis, Rheinischen Friedrich-Wikhelms-Universität Bonn, Bonn (2017).

[Kra18] A. Kramida, Y. Ralchenko, and J. Reader, *Nist atomic spectra database*.

[Kru01] E. Krutmeijer, *The nobel prize in physics 2001*.

[Kum19] J. Kumlin, K. Jachymski, and H. P. Büchler, *Beyond-mean-field corrections for dipolar bosons in an optical lattice*, Phys. Rev. A **99**, 033622 (2019).

[Lah09] T. Lahaye, C. Menotti, L. Santos, M. Lewenstein, and T. Pfau, *The physics of dipolar bosonic quantum gases*, Reports on Progress in Physics **72**, 126401 (2009).

[Li17] H. Li, J.-F. m. c. Wyart, O. Dulieu, and M. Lepers, *Anisotropic optical trapping as a manifestation of the complex electronic structure of ultracold lanthanide atoms: The example of holmium*, Phys. Rev. A **95**, 062508 (2017).

[Lim11] A. R. P. Lima and A. Pelster, *Quantum fluctuations in dipolar Bose gases*, Phys. Rev. A **84**, 041604 (2011).

[Lim12] A. R. P. Lima and A. Pelster, *Beyond mean-field low-lying excitations of dipolar Bose gases*, Phys. Rev. A **86**, 063609 (2012).

[Lu11] M. Lu, N. Q. Burdick, S. H. Youn, and B. L. Lev, *Strongly Dipolar Bose-Einstein Condensate of Dysprosium*, Phys. Rev. Lett. **107**, 190401 (2011).

[M11a] B. M and W. M, *Isotopic Compositions of the Elements 2009 (IUPAC Technical Report)*, PURE AND APPLIED CHEMISTRY **83**, 397–410 (2011).

[MÏ1b] S. Müller, J. Billy, E. A. L. Henn, H. Kadau, A. Griesmaier, et al., *Stability of a dipolar Bose-Einstein condensate in a one-dimensional lattice*, Phys. Rev. A **84**, 053601 (2011).

[Mah98] V. Mahajan, *Optical Imaging and Aberrations: Ray geometrical optics*, Online access with subscription: SPIE Digital Library, no. Teile 1-2, SPIE Optical Engineering Press, 1998.

[Mah13] V. Mahajan, *Optical Imaging and Aberrations: Wavefront analysis*, Optical Imaging and Aberrations, SPIE Optical Engineering Press, 2013.

[Mar17] M. Marszalek, *Assembly and testing of an objective lens designed for imaging ultracold quantum gases*, Master's thesis, Unversity of Innsbruck, Institut für Experimentalphysik (2017).

[Mat99] M. R. Matthews, B. P. Anderson, P. C. Haljan, D. S. Hall, C. E. Wieman, et al., *Vortices in a Bose-Einstein Condensate*, Phys. Rev. Lett. **83**, 2498–2501 (1999).

[Mor06] O. Morsch and M. Oberthaler, *Dynamics of Bose-Einstein condensates in optical lattices*, Rev. Mod. Phys. **78**, 179–215 (2006).

[Niu96] Q. Niu, X.-G. Zhao, G. A. Georgakis, and M. G. Raizen, *Atomic Landau-Zener Tunneling and Wannier-Stark Ladders in Optical Potentials*, Phys. Rev. Lett. **76**, 4504–4507 (1996).

[Pat21] A. Patscheider, B. Yang, G. Natale, D. Petter, L. Chomaz, et al., *Observation of a narrow inner-shell orbital transition in atomic erbium at 1299 nm*, Phys. Rev. Research **3**, 033256 (2021).

[Pet15] D. Petter, *Spatial modulation of light for ultracold gas experiments with erbium atoms*, Master's Thesis (2015).

[Roa04] G. Roati, E. de Mirandes, F. Ferlaino, H. Ott, G. Modugno, et al., *Atom Interferometry with Trapped Fermi Gases*, Phys. Rev. Lett. **92**, 230402 (2004).

[Sch16] M. Schmitt, M. Wenzel, F. Böttcher, I. Ferrier-Barbut, and T. Pfau, *Self-bound droplets of a dilute magnetic quantum liquid*, Nature **539**, 259–262 (2016).

[Smi07] W. J. Smith, *Modern optical engineering*, Optical Imaging and Aberrations, McGraw-Hills, 2007.

[Smi11] D. A. Smith, S. Aigner, S. Hofferberth, M. Gring, M. Andersson, et al., *Absorption imaging of ultracold atoms on atom chips*, Opt. Express **19**, 8471–8485 (2011).

[Soh21] M. Sohmen, *Supersolidity in Dipolar Quantum Gases in and out of Equilibrium*, PhD Thesis (2021).

[Tan19] L. Tanzi, E. Lucioni, F. Famà, J. Catani, A. Fioretti, et al., *Observation of a Dipolar Quantum Gas with Metastable Supersolid Properties*, Phys. Rev. Lett. **122**, 130405 (2019).

[Tei07] M. Teich and B. E. Saleh, *Fundamentals of photonics*, Wiley-Interscience;, 2007.

[Tra12] A. Trabesinger, *Quantum simulation*, Nature Physics **8**, 263–263 (2012).

[Wan37] G. H. Wannier, *The Structure of Electronic Excitation Levels in Insulating Crystals*, Phys. Rev. **52**, 191–197 (1937).

[Wil96] S. R. Wilkinson, C. F. Bharucha, K. W. Madison, Q. Niu, and M. G. Raizen, *Observation of Atomic Wannier-Stark Ladders in an Accelerating Optical Potential*, Phys. Rev. Lett. **76**, 4512–4515 (1996).

[Öt19] T. Öttl, *Designing and testing an objective for imaging ultracold quantum gases*, Master's thesis, Unversity of Innsbruck, Institut für Experimentalphysik (2019).

Acknowledgements

First, I would like to thank my supervisor Francesca Ferlaino for giving me the opportunity to work in the ERBIUM experiment. I'm thankful for the support she gave me all along this journey, up to the very last minute before handing in this thesis.

I'm very grateful to Manfred for all the time he accorded me during this project and for his joy to share technical knowledge. Thank you also for the last-minute corrections to the thesis.

Je remercie également l'école des Mines de Saint-Etienne qui m'a permis de réaliser ce double master avec l'université d'Innsbruck, en particulier Patrick Ganster pour avoir été mon tuteur durant cet échange. Un remerciement va aussi à mes professeurs de classe préparatoire qui m'ont donné le goût pour les sciences fondamentales et m'ont orienté dans la voie de la recherche.

Thanks to all the members of the ERBIUM, the ER-DY and T-REQS experiments as well as the members of the theory group, including Russel, and Wyatt with whom I share my office for the last months. Special thanks go to, Gabriele for introducing me to the very rich and exact science of coffee, Alexander for sharing with me all its technical expertise and Arfor for the time spent in the lab with a very good mood and nice music. Thanks also to Daniel, Simon, Sarah and Théo to have shared time with me in the lab.

A deep thank goes to our administrative assistant Silvia, who dealt with all my orders and was always providing me with administrative helps in the fastest delay. This thesis would not have been possible without the help of the mechanical workshop from both the university and IQOQI, thank you.

I also want to thank the people outside the university, starting with my incredible WG, who always gave me the chance to talk about all and nothing after long days in the lab. Ready at any time to go skiing, climbing or simply watching a movie. I should also not forget to thank our group *climbing and diner* with who I spent many hours whether outside or inside climbing.

Finalement, et non le moins important, je voudrais remercier ma famille. Merci à mon Papa et ma pitite moman de m'avoir donné l'opportunité d'aller étudier à Innsbruck et toujours encouragé dans mes choix d'étude. Merci à mes frères, Emilien et Anatole, pour me faire rire et rêver avec vos idées extravagantes. Enfin, un grand merci à Nadine pour me donner un socle si solide dans ma vie, je t'aime vvvvraiment.

universität
innsbruck

Eidesstattliche Erklärung

Ich erkläre hiermit an Eides statt durch meine eigenhändige Unterschrift, dass ich die vorliegende Arbeit selbständig verfasst und keine anderen als die angegebenen Quellen und Hilfsmittel verwendet habe. Alle Stellen, die wörtlich oder inhaltlich den angegebenen Quellen entnommen wurden, sind als solche kenntlich gemacht.

Die vorliegende Arbeit wurde bisher in gleicher oder ähnlicher Form noch nicht als Magister-/Master-/Diplomarbeit/Dissertation eingereicht.

Datum	Unterschrift